THIN-FILM ALN-ON-SILICON RESONANT GYROSCOPES: DESIGN, FABRICATION, AND EIGENMODE OPERATION

A Dissertation
Presented to
The Academic Faculty

by

Mojtaba Hodjat-Shamami

In Partial Fulfillment
of the Requirements for the Degree
Doctor of Philosophy in the
School of Electrical and Computer Engineering

Georgia Institute of Technology
December 2020

COPYRIGHT © 2020 BY MOJTABA HODJAT-SHAMAMI

THIN-FILM ALN-ON-SILICON RESONANT GYROSCOPES: DESIGN, FABRICATION, AND EIGENMODE OPERATION

Approved by:

Dr. Farrokh Ayazi, Advisor
School of Electrical and Computer Engineering
Georgia Institute of Technology

Dr. Oliver Brand
School of Electrical and Computer Engineering
Georgia Institute of Technology

Dr. F. Levent Degertekin
School of Mechanical Engineering
Georgia Institute of Technology

Dr. Peter J. Hesketh
School of Mechanical Engineering
Georgia Institute of Technology

Dr. David R. Myers
Department of Biomedical Engineering
Georgia Institute of Technology

Date Approved: December 3rd, 2020

To my parents

ACKNOWLEDGMENTS

First and foremost, I would like to thank my advisor, Professor Farrokh Ayazi, for his support and guidance throughout the past several years and giving me the opportunity to work on a rewarding project.

I would also like to thank my dissertation committee members, Professor Oliver Brand, Professor Levent Degertekin, Professor Peter Hesketh, and Professor David Myers for providing their feedback and insights.

This work was supported in part by the DARPA Microsystems Technology Office. I also wish to thank the Georgia Tech Institute for Electronics and Nanotechnology for fabrication support.

I am grateful for the support I have received from all my friends and colleagues at the IMEMS research group. I wish to thank Dr. Giorgio Casinovi, Dr. Jenna Fu, Dr. Logan Sorenson, Dr. Peng Shao, Dr. Diego Serrano, Dr. Yaesuk Jeong, Dr. Chang-Shun Liu, Dr. Vahid Tavassoli, and Dr. Chong Li. My special thanks go to Dr. Haoran Wen, Dr. Benoit Hamelin, Dr. Anosh Daruwalla, Dr. Jeremy Yang, Mr. Samuel Wisher, Mr. Jun-Yang Lei, Mr. Seung-Yong Shin, Mr. Jaehoo Choi, and Mr. Pranav Gupta. I would also like to particularly thank Dr. Arashk Norouzpour-Shirazi and Dr. Roozbeh Tabrizian with whom I have had the privilege of closely collaborating.

Finally, I would like to express my deepest gratitude to my family.

TABLE OF CONTENTS

ACKNOWLEDGMENTS **iv**

LIST OF TABLES **vii**

LIST OF FIGURES **viii**

LIST OF SYMBOLS AND ABBREVIATIONS **xiv**

SUMMARY **xvi**

Chapter 1. Introduction **1**

1.1 Brief Review of Vibratory Gyroscopes **2**

- 1.1.1. The Birth of a Modern Instrument 2
- 1.1.2. Tuning Fork Gyroscopes 4
- 1.1.3. Gyroscopes with Degenerate Modes of Vibration 6

1.2. Operation Principles of Coriolis Vibratory Gyroscopes **8**

1.3. Gyroscope Performance Specifications **12**

- 1.3.1. Definitions of the Performance Metrics 12

1.4. Motivation for the Development of Thin-Film Piezoelectric Gyroscopes **16**

Chapter 2. Design of Thin-film Piezoelectric Resonant Gyroscope **18**

2.1. Piezoelectric Transduction **19**

2.2. High-Frequency Piezoelectrically Transduced Gyroscopes **22**

- 2.2.1. In-Plane Flexural Vibration Mode Shapes 24
- *2.2.2. Effective Mass of the In-Plane Flexural Resonator* 28

2.2.3. Electromechanical Coupling Coefficient 30

2.2.4. Gyroscopic Coupling Coefficient 33

2.3. AlN-on-Silicon Fabrication Process 34

Chapter 3. Mode Matching of Resonant Piezoelectric Gyroscopes 38

3.1. Eigenmode Operation of Piezoelectric Devices 39

3.1.1. Theory of Eigenmode Operation 41

3.1.2. Principles of Eigenmode Operation 46

3.1.3. The Effect of Damping on Eigenmode Operation 49

3.1.4. Eigenmode Operation of an AlN-on-Si Resonant Gyroscope 50

3.2. Resonance Frequency and Quality Factor Tuning of Piezoelectric Devices 53

Chapter 4. A Mode-Matched AlN-on-Silicon Resonant Annulus Gyroscope 61

4.1. Design of the AlN-on-Si Annular Gyroscope 61

4.2. Fabrication and Characterization of the AlN-on-Si Annular Gyroscope 66

4.3. Improvement of the Bias Instability 76

Chapter 5. Conclusions and Future Directions 81

5.1. Center-Supported Design for the Piezoelectric Gyroscope 82

5.2. Pitch and Roll and Triaxial Piezoelectric Gyroscopes 83

REFERENCES 87

LIST OF TABLES

Table 1.1 Performance requirements for different classes of gyroscopes 15

Table 4.1 COMSOL simulation results for the AlN-on-Si resonant annulus gyroscope 65

LIST OF FIGURES

Figure 1.1 Bryan's depiction of the revolution of the vibration mode of a cylindrical shell subject to physical rotation of the body showing the direction of revolution for nodal meridians (1890). 2

Figure 1.2 First vibratory gyroscope by J. Lyman and N. Elwood (1943) 3

Figure 1.3 First silicon integrated vibratory gyroscope by J. O'Connor and D. Shupe (1983) 3

Figure 1.4 Micromachined tuning fork gyroscope developed at the Draper Laboratory 4

Figure 1.5 Quartz rate gyroscope developed at BEI-Systron Donner 5

Figure 1.6 Commercialized micromachined gyroscopes developed by Analog Devices (a), STMicroelectronics (b), and Invensense (c). 5

Figure 1.7 Mode-matched tuning fork gyro (a) and quadruple mass gyro (b) developed at Georgia Tech and UC Irvine respectively. 6

Figure 1.8 Degenerate-mode vibratory gyroscopes. (a) m-HRG developed by Northrop Grumman, (b) Birdbath resonator gyroscope, University of Michigan, (c) μ-HRG, Georgia Tech, (d) polysilicon vibrating shell gyroscope, University of Michigan, (e) disk resonator gyro, University of California, Davis, (f) BAW disk gyroscope, Georgia Tech 7

Figure 1.9 Different types of Coriolis vibratory gyroscopes (CVGs) 8

Figure 1.10 Simplified model of a vibratory gyroscope along with the free-body diagram 9

Figure 1.11 Allan deviation plot showing regions of different slopes and underlying associated noise sources 14

Figure 2.1 Displacement field (top) and stress field (bottom) for the in-plane flexural vibration mode shape of a square structure 24

Figure 2.2 AlN-on-Si resonant square gyroscope with triangular electrode placements for efficient drive mode excitation and sense mode decoupling (left) and the piezoelectric stack on the thick silicon substrate (right) 25

Figure 2.3 Displacement field (top) and stress field (bottom) for the in-plane flexural vibration mode shape of a disk structure 26

Figure 2.4 Displacement field (top) and stress field (bottom) for the in-plane flexural vibration mode shape of an annulus structure 26

Figure 2.5 AlN-on-Si resonant disk gyroscope with eight identical top electrodes and double-T supports around its periphery along with close up views of the support structure and routing 27

Figure 2.6 First three in-plane flexural vibration modes of the disk and annulus structures 28

Figure 2.7 Effective mass coefficient of the in-plane flexural annulus resonator as a function of the inner to outer radius of the annulus 29

Figure 2.8 Normalized effective mass of the in-plane flexural annulus gyroscope as a function of the inner to outer radius of the annulus 30

Figure 2.9 In-plane components of the stress field for the flexural (top) and elliptical (bottom) vibration modes showing the favored stress pattern of the flexural mode for top-surface piezoelectric transduction. 31

Figure 2.10 Gyroscopic coupling coefficient of the in-plane flexural annular gyroscope as a function of the inner to outer radius of the annulus 34

Figure 2.11 AlN-on-Si fabrication process flow. (a) deposit the piezoelectric stack on the SOI wafer, (b) pattern the top Mo layer, (c) deposit and pattern backside oxide layer, (d) etch AlN for access to bottom Mo layer, (e) etch AlN, bottom Mo, and Si device layers to define the device structure, (f) etch Si handle layer for backside release, (g) release the device in HF. 36

Figure 3.1 Frequency response of annular piezoelectric gyroscope with 16 identical top electrodes measured making it possible to measure the response around the annulus at every 22.5°. The level of the indirect response, which is a measure of modal coupling, changes as the angle of measurement changes. 40

Figure 3.2 Simulated magnitude of the drive and sense modes of a gyroscope for different cases of modal coupling and frequency mismatch. The eigenmode direction is where the drive response is maximum, and the sense response approaches zero. 44

Figure 3.3 Schematic representation of modal alignment techniques. (a) The electrostatic alignment technique corrects the misalignment in the stiffness direction to remove quadrature coupling. (b) Eigenmode 47 operation adjusts the excitation and readout directions to the as-fabricated natural vibration direction.

Figure 3.4 SEM image of the AlN-on-Si annular resonant gyroscope with 16 identical top electrodes. Pairs of adjacent electrodes are connected together, reducing the number of independently controlled electrodes to 8, suitable for eigenmode operation of the first in-plane flexural modes. 50

Figure 3.5 Drive and sense mode response of the gyroscope for different levels of the weighting factor α. For $\alpha = 0.8$, the resultant transduction direction is closest to the eigenmode direction; the sense-mode peak disappears from the drive response and the sense-mode amplitude is significantly reduced. 52

Figure 3.6 Schematic diagram of the second-order resonator with (top) and without (bottom) displacement feedback along with the corresponding force to displacement transfer functions 54

Figure 3.7 Schematic diagram of the second-order resonator with (top) and without (bottom) velocity feedback along with the corresponding force to velocity transfer functions 55

Figure 3.8 SEM images of the AlN-on-Si square resonator connected to the substrate using a network of T-supports 57

Figure 3.9 Schematic view of the piezoelectric square resonator and the isometric and top views of the second-order in-plane flexural vibration mode shape. 57

Figure 3.10 Interface system architecture for active feedback tuning of resonance parameters. 58

Figure 3.11 Frequency response of the piezoelectric resonator with active displacement feedback. The resonance frequency is tuned by ~400 p.p.m. in both directions. 58

Figure 3.12 Frequency response of the piezoelectric resonator with active velocity feedback. Quality factor is tuned from 1800 to 6300 with the reference *Q* value of 2900. 59

Figure 4.1 Drive and sense vibration mode shapes of the annulus piezoelectric gyroscope showing the displacement field (top) and the stress pattern (bottom) of the in-plane flexural resonant mode. The stress field pattern is suitable for top-side piezoelectric transduction. 62

Figure 4.2 Simulated output Coriolis current of the AlN-on-Si annulus resonant gyroscope, showing a scale factor of 1.62 nA/°/s for an assumed *Q* of 6,300 and a driving voltage of 90 mV peak. 64

Figure 4.3 SEM images of annulus piezoelectric resonant gyroscopes fabricated using a simple 4-mask AlN-on-Si process. (a) 8 top electrodes used for eigenmode operation of the gyroscope. (b) The network of peripheral tethers is used to both support the structure and provide a routing path for the electrical connections. 67

Figure 4.4 Schematic illustration of the eigenmode operation. The natural vibration modes are misaligned with respect to the electrodes as fabricated (left) and by applying scaling coefficients to electrode pairs the location of effective excitation and readout electrodes is virtually controlled and aligned with the eigenmodes (right). 68

Figure 4.5 (a) Interface system architecture of the piezoelectric gyroscope. The drive loop, sense channel, and dynamic displacement feedback are implemented in the FPGA in the digital domain. The piezoelectric gyroscope is actuated and sensed in the analog domain based on eigenmode operation. (b) Measurement setup, including a FlexRIO system from National Instruments in communication with the analog frontend mounted on the rate table and controlled by the PC. (c) Printed circuit board showing the device actuated by applying the eigenmode input pair voltage and sensed by processing the output current according to eigenmode operation. Potentiometers at the input and output are used for realization of the eigenmode operation coefficients. 70

Figure 4.6 The normalized drive and sense frequency responses of the AlN-on-Si resonant gyroscope as fabricated (a), with eigenmode operation only (b) and with eigenmode operation and dynamic frequency tuning applied (c). The zero-rate error is reduced by ~35 dB with the application of eigenmode operation. The device shows a *Q* of ~6,300 while operating in air, corresponding to a mode-matched mechanical bandwidth of 500 Hz. 71

Figure 4.7 (a) The measured output current of the piezoelectric gyroscope vs. the applied external rotation rate. The experimental scale factor is 1.57 nA/°/s for an input 90 mV peak drive voltage. (b) The time-domain output waveform for different rotation rates at two frequencies of 1 Hz and 2 Hz and different rotation amplitudes. (c) Allan deviation plot of the piezoelectric gyroscope showing a measured angle random walk of 0.86 °/√h, which is close to the simulated MNEΩ of 24.7 °/h/√Hz considering the effect of interface noise. The bias instability of the gyroscopes is ~125 °/h, 73 which is limited by the precision and excess noise of the interface circuitry.

Figure 4.8 Temperature characterization plots for the AlN-on-Si resonator gyroscope. (a) Temperature dependence of drive and sense resonance frequency deviations from the drive resonance frequency at 20°C showing a maximum frequency split of 107 ppm between the two modes with a maximum frequency split variation of 6 ppm over the temperature range. The linear temperature coefficient of frequency is ~ -12 ppm/°C. (b) Drive and sense mode insertion loss vs. temperature. The insertion loss of both modes remains almost constant over the temperature range with a maximum difference of 0.9% between the two modes and maximum variation of 0.6%. (c) Drive and sense mode *Q* vs. temperature. Considering mechanical decoupling from the substrate, the quality factor remains almost constant over the temperature range with a maximum difference of 3.2% between the two modes and a maximum variation of 2.2%. 75

Figure 4.9 Wideband frequency response of the piezoelectric gyroscope drive mode showing the spurious modes suppressed by at least 40 dB around the resonance peak. 76

Figure 4.10 Allan deviation plots with and without eigenmode operation. The bias instability is reduced from 1700 deg/h to ~270 deg/h by adjusting the eigenmode coefficients and hence the transduction direction. The residual bias is due to slight misalignment from the natural vibration directions caused by the limited resolution of eigenmode coefficients adjustment. 77

Figure 4.11 Allan deviation plots at two different drive voltage levels. Increasing the excitation voltage from 20mV to 50mV results in the reduction of thermal noise in the output bias as expected. However, this reduction does not translate to lower bias instability as it is limited by the phase noise of the NCO and DACs (flicker noise after demodulation) which is proportional to the excitation signal. In other words, larger excitation results in larger scale factor and hence lower ARW as the thermal noise remains constant but it does not result in lower bias instability as the flicker noise is signal dependent. 79

Figure 5.1 A center-supported AlN-on-Si resonant gyroscope. The annular structure is supported using a network of double-T tethers which serve as signal routing paths as well and anchored in the center to the handle layer. The device is separated from the peripheral substrate for package stress isolation. 83

Figure 5.2 A preliminary design for a pitch and roll AlN-on-Si resonant gyroscope with a second-order elliptical drive vibration mode and third-order out-of-plane bending sense modes. 84

Figure 5.3 A representative design for a triaxial AlN-on-Si gyroscope with the annular pitch and roll device supported to the peripheral substrate and the yaw device placed in the middle and anchored to the handle layer in the center of the structure. 85

LIST OF SYMBOLS AND ABBREVIATIONS

ADC	Analog-to-Digital Converter
AlN	Aluminum Nitride
ASIC	Application-Specific Integrated Circuit
AVAR	Allan Variance
BAW	Bulk Acoustic Wave
BI	Bias Instability
Cl_2	Chlorine
CVG	Coriolis Vibratory Gyroscope
DAC	Digital-to-Analog Converter
η	Electromechanical Coupling Coefficient
FBAR	Film Bulk Acoustic Wave Resonator
FEA	Finite-Element Analysis
FPGA	Field Programmable Gate Array
HF	Hydrofluoric Acid
HRG	Hemispherical Resonator Gyroscope
ICP	Inductively Coupled Plasma
IFOG	Interferometric Fiber-Optic Gyroscope
IMU	Inertial Measurement Unit
k_B	Boltzmann Constant
λ	Gyroscopic Coupling Coefficient
MEMS	Microelectromechanical System
$MNE\Omega$	Mechanical Noise Equivalent Rotation Rate

Mo	Molybdenum
NCO	Numerically Controlled Oscillator
O_2	Oxygen
Ω	Rotation Rate
PCB	Printed Circuit Board
PECVD	Plasma-Enhanced Chemical Vapor Deposition
PPM	Parts per Million
ρ	Volumetric Mass Density
RIE	Reactive Ion Etching
RLG	Ring Laser Gyroscope
ScAlN	Scandium Aluminum Nitride
SEM	Scanning Electron Microscope
SF_6	Sulfur Hexafluoride
Si	Silicon
SNR	Signal-to-Noise Ratio
SOI	Silicon on Insulator
TFG	Tuning Fork Gyroscope
TMAH	Tetramethylammonium Hydroxide
ZRO	Zero-Rate Output

SUMMARY

Resonant MEMS gyroscopes have been rapidly adopted in various consumer, industrial, and automotive applications thanks to their small size, low cost of manufacturing, and high sensitivity. The current efforts in enhancing the performance of high-precision resonant gyroscopes are mainly focused on two seemingly contradictory metrics, larger bandwidth and lower noise level, to push the technology towards inertial navigation applications. Considering the advantages brought about by *Q*-amplification in micromechanical resonators, mode matching has been the primary means of achieving a very high signal-to-noise ratio in Coriolis vibratory gyroscopes. However, mode matching imposes a heavy constraint on the operational bandwidth of high-*Q* devices, creating a tradeoff between the bandwidth and noise level.

Capacitive bulk acoustic wave gyroscopes rectify this problem to some extent by employing stiff bulk vibration modes of the resonating structure and hence significantly increasing the resonance frequency of the device. Bulk-mode resonant gyroscopes operating in the megahertz frequency range have also been shown to offer superior shock and vibration immunity. Nevertheless, these advantages come at the cost of intricate fabrication processing to realize high-aspect-ratio capacitive gaps, stringent vacuum encapsulation requirements, and on-chip DC polarization charge pumping.

The key enabling factor for the realization of low-noise high-bandwidth resonant gyroscopes is the utilization of a strong electromechanical transducer at high frequencies. Thin-film piezoelectric-on-silicon technology provides a very efficient transduction mechanism suitable for implementation of bulk-mode resonant gyroscopes without the need for submicron capacitive gaps or large DC polarization voltages. More importantly, the in-air operation of piezoelectric devices at moderate *Q* values allows for the cointegration of mode-matched gyroscopes and accelerometers on a common substrate for inertial measurement units. To attain this goal, gyroscopic vibration modes compatible with thin-film piezoelectric transduction must be identified. Also, contrary to capacitive devices that exploit the electrostatic spring softening mechanism for mode matching, piezoelectric gyroscopes require alternative techniques for frequency matching and modal alignment that can be applied independently of electrostatic transduction.

This work presents the design, fabrication, characterization, and method of mode matching of piezoelectric-on-silicon resonant gyroscopes. The degenerate in-plane flexural vibration mode shapes of a disk or annulus are demonstrated to have gyroscopic coupling as well as a strong piezoelectric transduction coefficient. In particular, the annulus structure is adopted as the preferred geometry for the implementation of piezoelectric gyroscope design. Eigenmode operation of resonant gyroscopes, based on virtual alignment of the transduction direction to the natural direction of vibration modes, is introduced as the modal alignment technique for the piezoelectric devices independently of the transduction mechanism. This method can also be applied for mode matching of devices that require sophisticated electrode arrangements for modal alignment, such as electrostatic pitch and roll gyroscopes with slanted electrodes that are utilized for out-of-plane quadrature error cancellation. Controlled displacement feedback is also employed as the frequency matching technique to accomplish complete mode matching of the piezoelectric gyroscopes.

Gyroscopic operation of a 3.15 MHz AlN-on-Si annulus resonator that utilizes a pair of high-*Q* degenerate in-plane vibration modes is demonstrated. The piezoelectric gyroscope shows a mode-matched operation bandwidth of ~250 Hz, which is one of the largest open-loop bandwidth values reported for a mode-matched MEMS gyroscope, a small motional resistance of ~1300 Ω owing to efficient piezoelectric transduction, and a scale factor of 1.57 nA/°/s for operation at atmospheric pressure, which greatly relaxes packaging requirements. Eigenmode operation results in an ~35 dB reduction in the quadrature error at the resonance frequency. The measured angle random walk of the device is 0.86 °/√h with a bias instability of 125°/h limited by the excess noise of the discrete electronics.

CHAPTER 1. INTRODUCTION

"Gyroscope, an elegant philosophical instrument," – John Herschel

Gyroscopes are sensors that measure the rate or angle of mechanical rotation with respect to inertial space about a specified axis. Primarily, they were developed for navigation and stabilization applications. However, with the advent of microelectromechanical system (MEMS) technology and the dramatic reduction in the size, power, and cost of micromachined sensors, gyroscopes are now being used for various emerging applications in the consumer electronic market.

Based on the physical phenomenon used to detect rotational motion gyroscopes are categorized in different classes. Mechanical gyroscopes detect angular motion based on the conservation of angular momentum of a spinning mass. A fast spinning mass ideally connected to a frame through frictionless bearings resists any change in its angular momentum and therefore any rotation applied to the frame can be detected based on the relative position of the spinning mass and the frame. Optical gyroscopes make use of the Sagnac effect to detect rotational motion. The phase shift between two light waves traveling in a ring in opposite directions is proportional to the angular velocity of the ring. Ring laser gyroscope (RLG) and interferometric fiber-optic gyroscope (IFOG) are examples of devices that sense rotation based on the Sagnac effect. The most widely used method of sensing angular rotation, however, is based on the Coriolis effect, named after Gaspard-Gustave Coriolis who first described it in 1835, and is utilized in vibratory gyroscopes. In a rotating frame, an apparent force is exerted on any moving body. Detection of this force which is proportional to the angular rate of rotation and the velocity of the moving object and perpendicular to both constitutes the basis for all vibratory gyroscopes. Although there has been recent interest in miniaturizing optical gyroscopes, the dominant majority of microfabricated gyroscopes are vibratory gyroscopes operating based on the Coriolis effect.

1.1 Brief Review of Vibratory Gyroscopes

1.1.1. The Birth of a Modern Instrument

In a communication to the Cambridge Philosophical Society in 1890, George H. Bryan described the nature of the beats which can be heard when a vibrating shell is rotated about its axis [1]. He attributed this effect to the revolution of the nodal meridians, with an angular velocity less than but in the same direction of that of the rotating object, which depends on the mode of vibration (Figure 1.1). This very important observation laid the foundation for the development of vibratory gyroscopes many decades later.

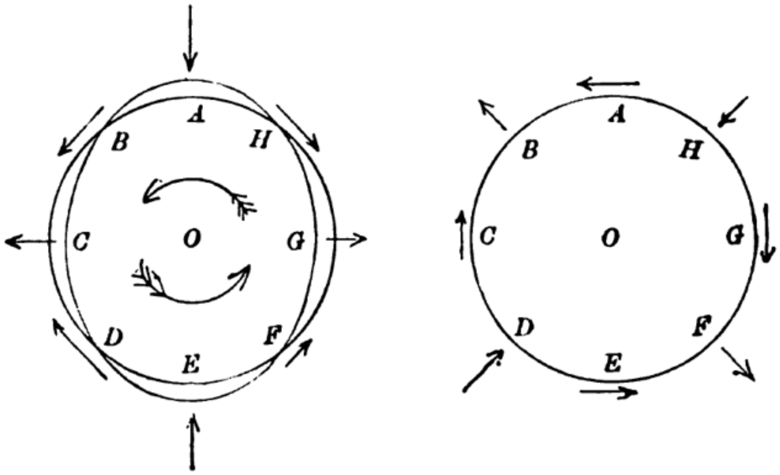

Figure 1.1: Bryan's depiction of the revolution of the vibration mode of a cylindrical shell subject to physical rotation of the body showing the direction of revolution for nodal meridians (1890).

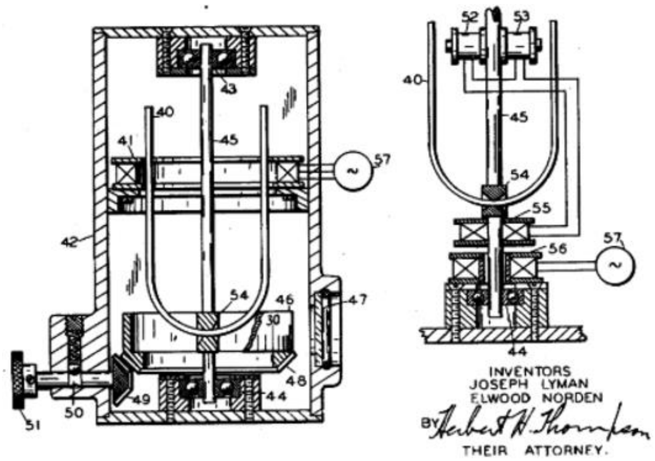
43
40
45
41
57
42
54
46
30
47
48
44
49
50
51
52
53
40
45
54
55
56
57
44
INVENTORS
JOSEPH LYMAN
ELWOOD NORDEN
BY
THEIR ATTORNEY.

Figure 1.2: First vibratory gyroscope by J. Lyman and N. Elwood (1943)

The very first vibratory gyroscope was invented by Joseph Lyman and Norden Elwood of Sperry Gyroscope Company in 1943 (Figure 1.2) [2] . They used a tuning fork structure in their apparatus to detect rotational motion and since then, the term tuning fork gyroscope (TFG) has remained with the two-body vibratory gyroscopes.

The first Silicon integrated gyroscope was invented by James O'Connor and David Shupe in 1983 [3]. Their device, as shown in Figure 1.3, consisted of a single cantilever resonator which was excited at resonance and piezoresistive elements that were used to detect rotation of the vibrating beam about an axis parallel to its length.

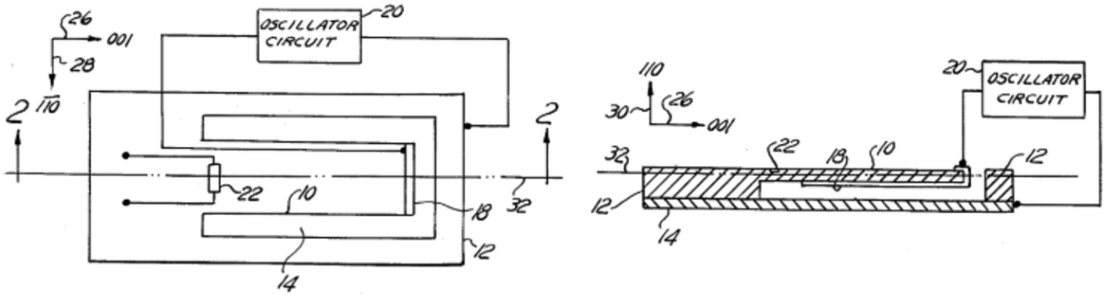
26
001
28
110
2
OSCILLATOR CIRCUIT
20
2
22
10
18
32
12
14
110
30
26
001
20
OSCILLATOR CIRCUIT
32
22
18
10
12
12
14

Figure 1.3: First silicon integrated vibratory gyroscope by J. O'Connor and D. Shupe (1983)

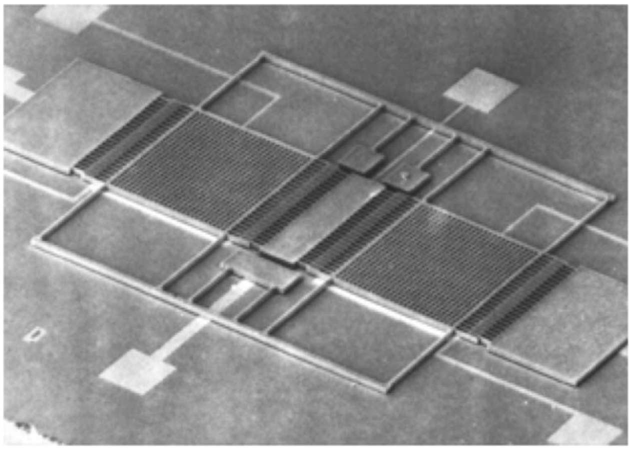

Figure 1.4: Micromachined tuning fork gyroscope developed at the Draper Laboratory

1.1.2. Tuning Fork Gyroscopes

Jonathan Bernstein and Marc Weinberg of the Draper Laboratory developed a brilliant design for a micromachined tuning fork gyroscope (TFG) in 1994 [4]. Although this gyroscope did not show very good performance at the beginning, it is fair to say that most other designs of MEMS TFGs that used capacitive transduction and were developed later have been close variants of the Draper gyroscope shown in Figure 1.4.

Michael Layton of BEI-Systron Donner devised a quartz tuning fork gyroscope in 1998 [5] and this type of gyroscope (Figure 1.5) dominated the automotive and industrial markets until the capacitive micromachined TFGs were successfully commercialized a few years later.

Analog Devices, STMicroelectronics, Invensense, and Bosch have been the major players in commercialization of the low-cost high-volume micromachined gyroscopes (Figure 1.6) which made inertial sensing accessible for a vast range of consumer electronic

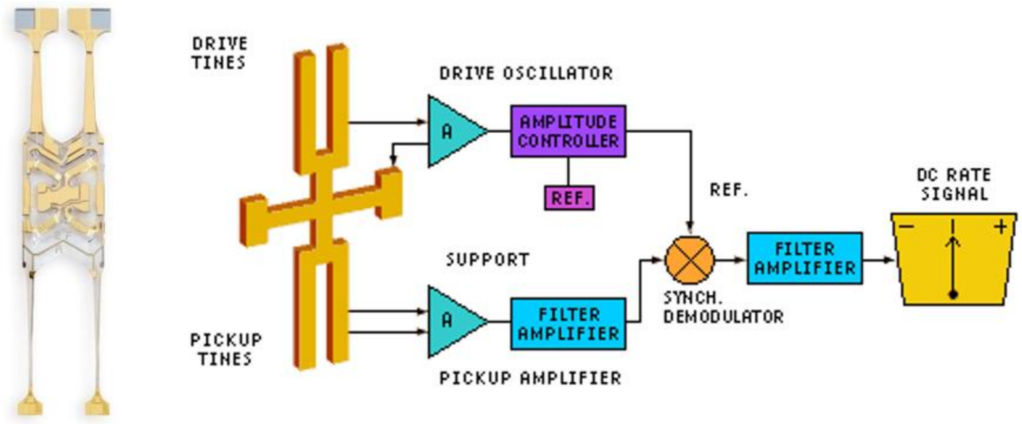
DRIVE TINES
DRIVE OSCILLATOR
A
AMPLITUDE CONTROLLER
REF.
REF.
DC RATE SIGNAL
−
+
SUPPORT
FILTER AMPLIFIER
SYNCH. DEMODULATOR
A
FILTER AMPLIFIER
PICKUP TINES
PICKUP AMPLIFIER

Figure 1.5: Quartz rate gyroscope developed at BEI-Systron Donner

devices such as smart phones, tablets, gaming controllers, cameras, drones, and virtual reality hardware [6-12].

Analog Devices opted for the integration of the MEMS and ASIC on the same die whereas the other companies took the different approach of fabricating the mechanical device and the electronics on separate substrates and providing the connections between the two chips using vias and bond wires. It appears now that the second approach has been more successful in addressing the needs of the consumer and industrial markets.

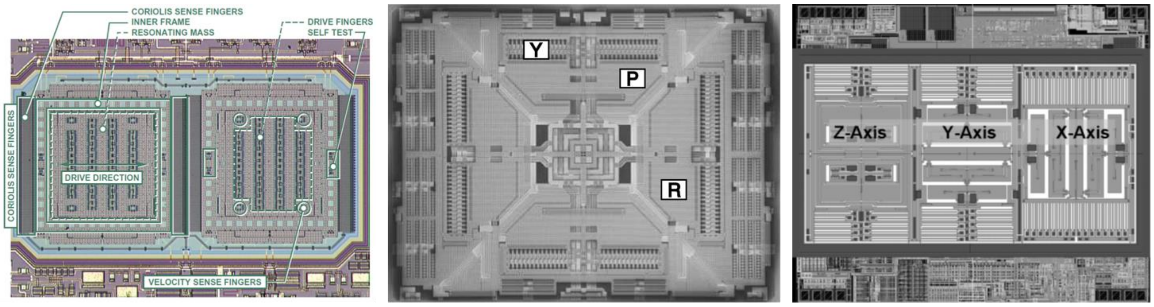
CORIOLIS SENSE FINGERS
INNER FRAME
RESONATING MASS
DRIVE FINGERS
SELF TEST
CORIOLIS SENSE FINGERS
DRIVE DIRECTION
VELOCITY SENSE FINGERS
Y
P
R
Z-Axis
Y-Axis
X-Axis

(a) (b) (c)

Figure 1.6: Commercialized micromachined gyroscopes developed by Analog Devices (a), STMicroelectronics (b), and Invensense (c).

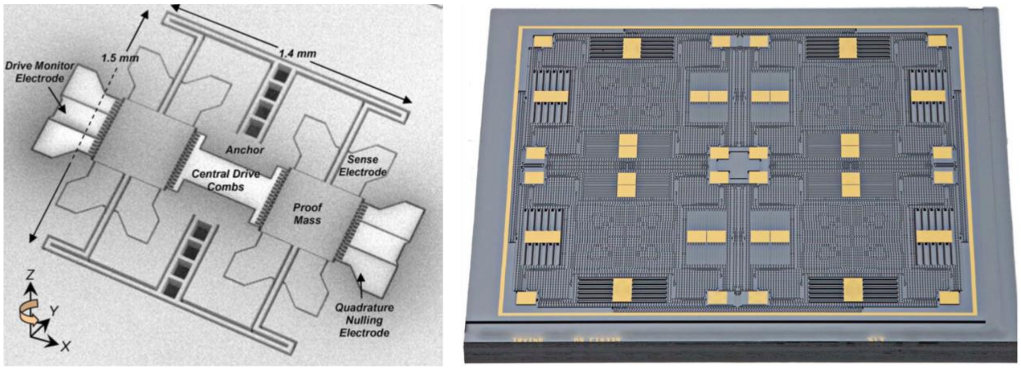

(a) (b)

Figure 1.7: Mode-matched tuning fork gyro (a) and quadruple mass gyro (b) developed at Georgia Tech and UC Irvine respectively.

Academic research on the tuning fork gyroscopes has been mainly focused on the development of mode-matched gyroscopes. The two vibration modes of the mode matched TFGs are designed to have the same resonant frequency to take advantage of mechanical quality factor amplification of the output signal to achieve better performance. The tuning fork gyroscope developed at Georgia Tech [13] and the quadruple mass gyroscope developed at UC Irvine [14] are good examples of such devices. Anti-phase actuation of the two and four resonating proof masses removes sensitivity to linear acceleration and angular acceleration respectively.

1.1.3. Gyroscopes with Degenerate Modes of Vibration

Structures with four-fold rotational symmetry can support two distinct vibration modes which occur at the exact same frequency. Gyroscopes that utilize these two degenerate modes have the advantage of mode-matched operation not just by design but by geometry, reducing the sources of mismatch between the two gyroscopic modes to fabrication nonidealities or material anisotropy.

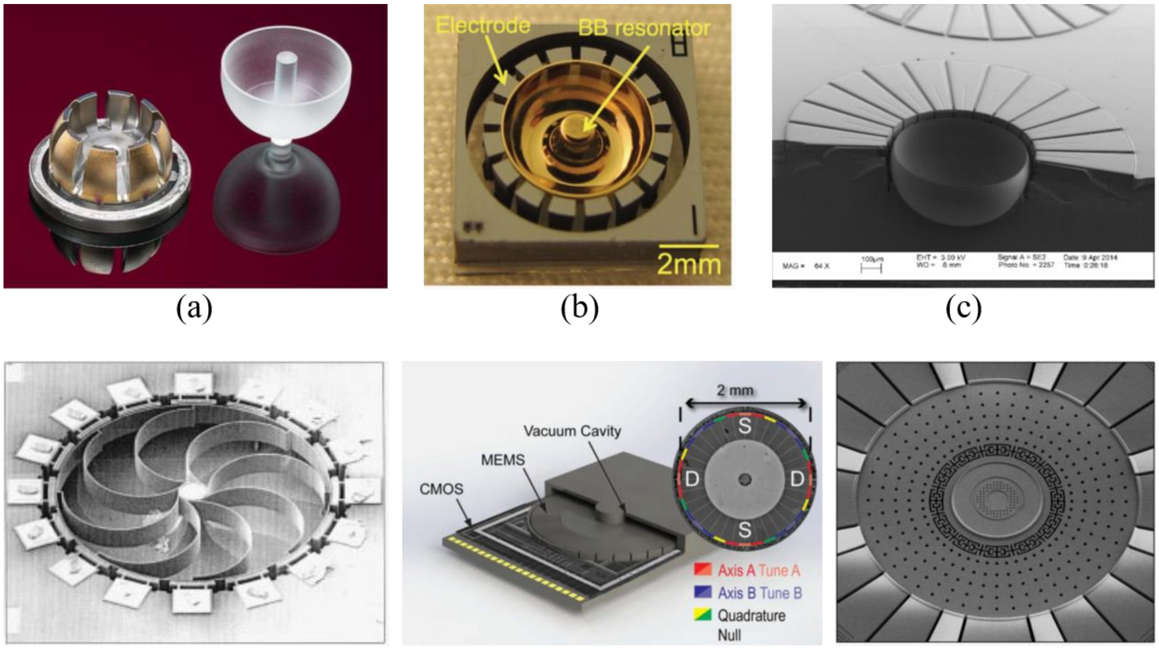

(a) (b) (c)

(d) (e) (f)

Figure 1.8: Degenerate-mode vibratory gyroscopes. (a) m-HRG developed by Northrop Grumman, (b) Birdbath resonator gyroscope, University of Michigan, (c) µ-HRG, Georgia Tech, (d) polysilicon vibrating shell gyroscope, University of Michigan, (e) disk resonator gyro, University of California, Davis, (f) BAW disk gyroscope, Georgia Tech

Many different structures have been used for implementation of degenerate mode gyroscopes among which the hemispherical resonator gyroscope (HRG) developed by Northrop Grumman is the most well-known design which has been successfully adopted for space applications. Figure 1.8a shows a milli-HRG [15] with small dimensions and lower part counts based on a simplified HRG design. The great success of the HRG has sparked much interest in miniaturization and batch fabrication of the hemispherical gyroscope. The challenge in the realization of micro-scale HRG is with maintaining the very large mechanical quality factor as the surface to volume ratio of the device decreases. Figure 1.8b shows a fused silica birdbath resonator gyroscope with high quality factor [16] and Figure 1.8c shows a fully integrated micro hemispherical resonator gyroscope [17, 18] as two examples of micromachined HRG devices.

Ring and disk structures have also been widely used for the implementation of degenerate-mode vibratory gyroscopes as shown in Figure 1.8d for a polysilicon vibrating shell gyroscope [19], Figure 1.8e for a disk resonating gyroscope [20] and Figure 1.8f for a substrate-decoupled bulk acoustic wave (BAW) gyroscope [21].

1.2. Operation Principles of Coriolis Vibratory Gyroscopes

The fundamental mechanism for detection of rotational motion in vibratory gyroscopes is based on the sensing of the Coriolis force in a rotating frame. Coriolis force appears to be applied to moving objects due to a coordinate transformation from a fixed to a rotating frame and can be sensed by the objects attached to the rotating frame. Therefore, vibratory gyroscopes utilize two distinct modes of vibration to excite the motion and sense Coriolis signal. The device is actuated along the first (drive) mode and a signal proportional to the rotation rate is picked off along the second (sense) mode. The motion of the second mode is induced due to the transfer of energy between the two modes by the Coriolis effect.

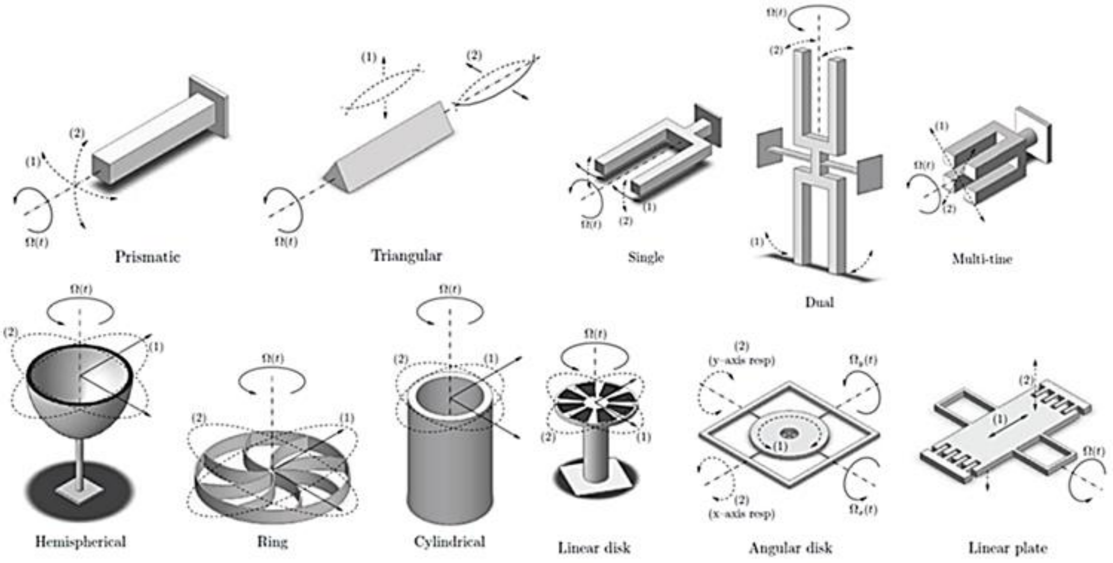
Prismatic
Triangular
Single
Dual
Multi-tine
Hemispherical
Ring
Cylindrical
Linear disk
Angular disk
Linear plate
(1)
(2)
Ω(t)
(y-axis resp)
(x-axis resp)
Ω_y(t)
Ω_x(t)

Figure 1.9: Different types of Coriolis vibratory gyroscopes (CVGs)

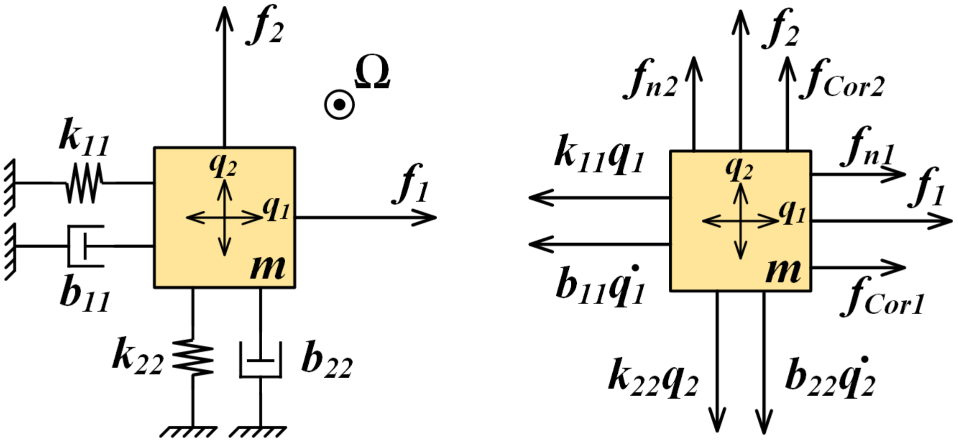

Figure 1.10: Simplified model of a vibratory gyroscope along with the free-body diagram

Coriolis vibratory gyroscopes mostly fall into one of the four categories of vibrating beams, tuning forks, vibrating plates, and vibrating shells [22] as shown in Figure 1.9. Considering two orthogonal vibration modes, we can use a simplified mass-spring-damper system to model these devices and derive their governing equations of motion as depicted in Figure 1.10. The generalized coordinates, q_1 and q_2 are defined in the orthogonal drive and sense directions. m, k, and b represent the point mass, stiffness and damping coefficients, Ω is the rotation rate perpendicular to the directions of vibration, f_1 is the externally applied drive force and let us assume $f_2 = 0$ so there is no external force applied to the sense mode, $f_{Cor} = 2m\Omega\dot{q}$ represents the Coriolis force which can be neglected at the drive mode, and f_n represents thermomechanical noise force with the power spectral density of $\sqrt{4k_BTb}$. We can write the equations of motion as follows.

$$\begin{cases} m\ddot{q}_1 + b_{11}\dot{q}_1 + k_{11}q_1 = f_1 + 2m\Omega\dot{q}_2 + f_{n1} \\ m\ddot{q}_2 + b_{22}\dot{q}_2 + k_{22}q_2 = f_2 - 2m\Omega\dot{q}_1 + f_{n2} \end{cases} \tag{1.1}$$

Depending on the values of the drive and sense resonance frequencies, we can define mode-split and mode-matched operation of the vibratory gyroscopes. Mode-split gyros are driven at the drive resonance frequency which is significantly lower than the sense resonance frequency. Under this condition we can find the Coriolis and noise displacements at the sense mode as given below assuming that the drive force dominates the Coriolis and noise forces and maintains a constant displacement of q_1 at the drive mode.

$$q_{2,\Omega} = \frac{-2\dfrac{j\omega_1 q_1}{\omega_2^2}}{1-\left(\dfrac{\omega_1}{\omega_2}\right)^2 + j\dfrac{1}{Q_2}\left(\dfrac{\omega_1}{\omega_2}\right)}\Omega \cong -j2\frac{\omega_1 q_1}{\omega_2^2}\Omega \tag{1.2}$$

$$q_{2,n} = \frac{\dfrac{f_{n2}}{m\omega_2^2}}{1-\left(\dfrac{\omega_1}{\omega_2}\right)^2 + j\dfrac{1}{Q_2}\left(\dfrac{\omega_1}{\omega_2}\right)} \cong \frac{f_{n2}}{m\omega_2^2} \tag{1.3}$$

In these equations, ω_1, ω_2, Q_1, and Q_2 are the resonance frequencies and quality factors of the drive and sense modes respectively. Using equations (1.2) and (1.3), we can find the scale factor and the mechanical noise equivalent rotation rate for the mode-split gyroscopes as

$$SF_{m-s} = -j2\frac{\omega_1 q_1}{\omega_2^2} \tag{1.4}$$

$$MNE\Omega_{m-s} = \sqrt{\frac{k_B T\omega_2}{2E_{k,1}Q_2}}\ \frac{rad/s}{\sqrt{Hz}} \tag{1.5}$$

where $E_{k,1}$ is the kinetic energy of the drive mode and k_B is the Boltzmann constant.

Mode-matched gyroscopes as opposed to mode-split gyros are driven at a drive resonance frequency which is equal to the sense resonance frequency. This condition could be met either by careful design of an asymmetric structure or by employing degenerate vibration modes of a mechanical structure with four-fold rotational symmetry. Setting the drive and sense resonance frequencies equal $\left(\omega_1 = \omega_2 = \omega_o\right)$ we can find the scale factor and mechanical noise equivalent rotation rate for the mode-matched case as given below.

$$q_{2,\Omega} = -2Q_2 \frac{q_1}{\omega_o} \Omega \tag{1.6}$$

$$q_{2,n} = -jQ_2 \frac{f_{n2}}{m\omega_o^2} \tag{1.7}$$

$$SF_{m-m} = -2Q_2 \frac{q_1}{\omega_o} \tag{1.8}$$

$$MNE\Omega_{m-m} = \sqrt{\frac{k_B T \omega_o}{2E_{k,1} Q_2}} \frac{rad/s}{\sqrt{Hz}} \tag{1.9}$$

Matching the drive and sense modes enables Q amplification of the output signal as we can see in equation (1.8) which greatly reduces the burden on electronics noise requirements. In other words, although the mechanical noise equivalent rotation rate is the same for the mode-matched and mode-split cases, the total signal-to-noise ratio (SNR) is higher for mode-matched devices as the electrical noise level can be more easily designed to be below the mechanical noise limit.

1.3. Gyroscope Performance Specifications

1.3.1. Definitions of the Performance Metrics

The performance specifications of rate gyroscopes are defined in the IEEE Standards for Inertial Sensor Terminology [23]. The most widely used specification parameters are given in this section with the definitions taken from the above-mentioned standard.

Scale factor: The ratio of a change in output to a change in the input intended to be measured. Scale factor is generally evaluated as the slope of the straight line that can be fitted by the method of least squares to the input-output data.

Bias: The average over a specified time of gyro output measured at specified operating conditions that has no correlation with input rotation or acceleration. Bias is typically expressed in °/h.

Resolution: The largest value of the minimum change in input, for inputs greater than the noise level, which produces a change in output equal to some specified percentage (at least 50%) of the change in output expected using the nominal scale factor.

Dynamic range: The ratio of the input range to the resolution.

Sensitivity: The ratio of a change in output to a change in an undesirable or secondary input. For example: a scale factor temperature sensitivity of a gyro is the ratio of change in scale factor to a change in temperature.

Cross-coupling errors: The errors in the gyro output resulting from gyro sensitivity to inputs about axes normal to an input reference axis.

Characterization of the gyroscope bias, among all the other metrics, is of utmost importance especially for navigation applications. Gyro bias drift is a major source of error in inertial measurement units (IMU) as the integration of the drifting bias results in the accumulation of error in the heading angle information. Bias drift can be caused by deterministic effects, however, the presence of random sources of noise in the gyroscope bias necessitates the use of stochastic methods for characterization of bias. Allan variance (AVAR) is a widely used tool for characterization of oscillator phase and frequency stability [24] and due to similarities has been adopted for the characterization of inertial sensors bias data as well. Assuming the rate bias data series Ω_k for $k = 1, 2, .., N$ and sampling time of τ_o, AVAR is defined as

$$\sigma^2(\tau) = \frac{1}{2}\left\langle \left(\bar{\Omega}_{k+m} - \bar{\Omega}_k\right)^2 \right\rangle \tag{1.10}$$

where $\tau = m\tau_o$, $\overline{\Omega}_k$ is the cluster average of m rate samples, and $\langle \ \rangle$ represents ensemble average. Allan deviation is defined as the square root of Allan variance.

The contribution of the error processes can be distinguished using this method, as different noise sources appear in different regions of the Allan deviation plot. Figure 1.11 shows the characteristics of the logarithmic Allan deviation plot for rate gyroscope bias indicating different regions and the underlying associated noise sources [25].

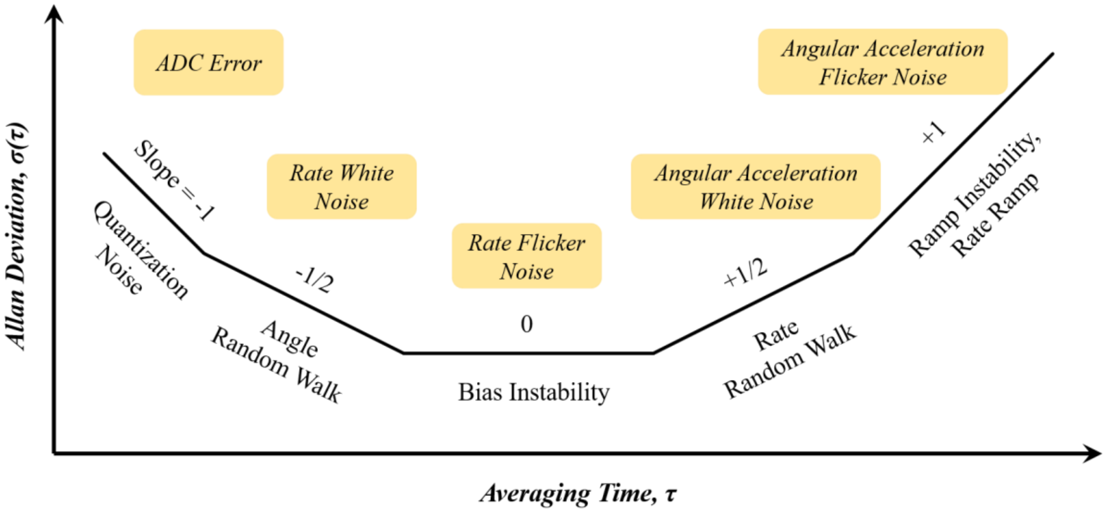
ADC Error
Angular Acceleration Flicker Noise
Slope = -1
Rate White Noise
Angular Acceleration White Noise
+1
Quantization Noise
Rate Flicker Noise
Ramp Instability, Rate Ramp
-1/2
+1/2
0
Angle Random Walk
Bias Instability
Rate Random Walk
Allan Deviation, σ(τ)
Averaging Time, τ

Figure 1.11: Allan deviation plot showing regions of different slopes and underlying associated noise sources

Quantization noise: this is the noise associated with the analog-to-digital conversion of the rate data. It appears with a slope of -1 in the log-log plot of Allan deviation versus averaging time.

Angle random walk: The angular error buildup with time that is due to white noise in angular rate. This error is typically expressed in degrees per square root of hour (°/√h). The effect of white rate noise appears with a slope of -1/2 in the Allan deviation plot.

Bias instability: The random variation in bias as computed over specified finite sample time and averaging time intervals. This nonstationary (evolutionary) process is characterized by a 1/f power spectral density. Bias instability is typically expressed in degrees per hour (°/h). The origin of this noise is either electronics or other components demonstrating flicker noise and it shows as a flat region in the Allan deviation plot.

Rate random walk: The drift rate error buildup with time that is due to white noise in angular acceleration. This error is typically expressed in degrees per hour per square root of hour ((°/h)/√h) and shows up with a slope of +1/2 in the Allan deviation plot.

Rate ramp: A gyro behavior characterized by quadratic growth with averaging time of the rate Allan variance. This error could have a deterministic origin related to the test conditions and appears with a slope of +1 in the log-log Allan deviation plot versus averaging time. It is worth noting that an angular acceleration flicker noise component also appears with a slope of +1 in the Allan deviation plot.

According to their performance requirements, vibratory rate gyros can be categorized in three different classes of rate grade, tactical grade, and inertial-grade gyros as given in Table 1.1 [26].

Table 1.1: Performance requirements for different classes of gyroscopes

Parameter	Rate Grade	Tactical Grade	Inertial Grade
Angle random walk (°/√h)	> 0.5	0.5 – 0.05	< 0.001
Bias drift (°/h)	10 – 1000	0.1 – 10	< 0.01
Scale factor accuracy (%)	0.1 – 1	0.01 – 0.1	< 0.001
Full-scale range (°/s)	50 – 1000	> 500	> 400
Bandwidth (Hz)	> 70	~ 100	~ 100

1.4. Motivation for the Development of Thin-Film Piezoelectric Gyroscopes

Recent advances in reliable deposition of thin-film piezoelectric materials has instigated the development of several successful piezoelectric resonant devices such as filters, duplexers, and timing devices. Similarly, Coriolis vibratory gyroscopes being resonant sensors must benefit from the advantages of piezoelectric transduction. Thin-film piezoelectric transduction is especially suitable for devices operating at high frequencies. It can replace submicron capacitive gaps which are difficult to fabricate, eliminate the charge pump in the interface circuitry as there is no need for polarization voltages with piezoelectric devices, and offer greater linearity and power handling capability. In addition, relaxed vacuum encapsulation and hence quality factor requirements along with highly efficient piezoelectric transduction facilitates the design of large-bandwidth piezoelectric gyroscopes with low motional resistance.

Overall, piezoelectric transduction poses great opportunities for the implementation of low noise, low power, wide band gyroscopes. However, the great challenges that come with the design and mode matching of these devices have precluded the realization of thin-film piezoelectric gyroscopes to date. The aspiration behind this research is to introduce methods for the design and operation of mode matched AlN-on-Si gyroscopes and to develop a new technology platform for implementation of high-frequency resonant gyroscopes to first compete with the current capacitive technology and then exceed in terms of power, noise and bandwidth performance.

CHAPTER 2. DESIGN OF THIN-FILM PIEZOELECTRIC RESONANT GYROSCOPE

"If you want to find the secrets of the universe, think in terms of energy, frequency, and vibration." – Nikola Tesla

Over the past few decades, different transduction mechanisms including electrostatic, piezoelectric, and electromagnetic have been used for implementation of Coriolis vibratory gyroscopes. However, the consumer and industrial gyroscope market is currently dominated by capacitive devices mainly due to their robust and reliable fabrication process. The recent advances in the deposition process of thin-film piezoelectric materials, on the other hand, has drawn a lot of attention towards the adoption of piezoelectric transduction in resonant devices. Bulk acoustic wave (BAW) filters and duplexers are perhaps the most successful electromechanical devices on the market today and utilize thin films of aluminum nitride (AlN) or scandium-doped aluminum nitride (ScAlN) for energy conversion between the electrical and mechanical domains [27, 28].

There come many advantages with adopting piezoelectric transduction as the only electromechanical coupling mechanism for vibratory gyroscopes. Piezoelectric devices do not require vacuum encapsulation which is favorable considering conflicting package pressure requirements for cointegration of gyroscopes and accelerometers. They also do not require DC polarization voltages resulting in the elimination of charge pumps in the interface circuitry and further, they can provide more efficient transduction compared with capacitive devices making them the better candidates for low-power sensing applications.

There are challenges also associated with the design of piezoelectric gyroscopes compared with capacitive devices. Contrary to capacitive transduction which is directly related to the displacement field of the vibration mode shape, the underlying parameter that affects the efficiency of piezoelectric transduction is the strain or stress field. Therefore, identifying gyroscopic modes that are compatible with piezoelectric transduction is a crucial step in the design process of piezoelectric gyroscopes. Frequency matching and modal alignment of the mode-matched devices is another important aspect that needs to be considered in the absence of electrostatic tuning capability. This chapter presents the design of the gyroscope device suited for piezoelectric transduction. Methods of mode matching compatible with all-piezoelectric devices will be presented in chapter 3.

2.1. Piezoelectric Transduction

A piezoelectric medium can be described using the linear constitutive equations to interrelate the mechanical stress (T_{ij}), mechanical strain (S_{ij}), electric intensity (E_k), and electric displacement (D_k) fields in the solid mechanic and electrostatic domains [29]. Depending on the choice of the dependent variables, the constitutive equations can be given in four different forms. However, the strain-charge and stress-charge equations are the two more common forms used in engineering usage as given below.

$$\begin{cases} S_{ij} = s_{ijkl}^{E} T_{kl} + d_{kij} E_k \\ D_i = d_{ijk} T_{jk} + \varepsilon_{ij}^{T} E_j \end{cases} \tag{2.1}$$

$$\begin{cases} T_{ij} = c_{ijkl}^{E} S_{kl} - e_{kij} E_k \\ D_i = e_{ijk} S_{jk} + \varepsilon_{ij}^{S} E_j \end{cases} \tag{2.2}$$

In the above equations s_{ijkl} and c_{ijkl} are the compliance and stiffness tensors, d_{ijk} and e_{ijk} are the piezoelectric strain coefficient and piezoelectric stress coefficient tensors, ε_{ij} is the permittivity tensor, the superscript parameters indicate measurement of the coefficients under the corresponding field being held constant, and summation over repeated indices is assumed.

The linear piezoelectric constitutive equations are commonly presented in a matrix form where symmetry conditions are considered to reduce the number of independent matrix elements. Symmetry of the stress and strain fields $\left(T_{ij} = T_{ji} \text{ and } S_{ij} = S_{ji}\right)$ results in the reduction of independent elements of the stiffness tensor from 81 to 36 $\left(c_{ijkl} = c_{jikl} \text{ and } c_{ijkl} = c_{ijlk}\right)$, which makes their representation possible using a 6×6 matrix. The relationship between the elasticity constants and strain energy density imposes additional symmetry requirements on the stiffness tensor, further reducing the number of the independent constants from 36 to 21 $\left(c_{ijkl} = c_{klij}\right)$. The same conditions apply to the compliance tensor elements as well. Similarly, the symmetry of stress and strain fields result in the reduction of the number of independent piezoelectric strain and stress coefficient tensors from 27 to 18 $\left(d_{ijk} = d_{ikj} \text{ and } e_{ijk} = e_{ikj}\right)$, making their representation possible using 3×6 matrices. The permittivity tensor in general has 6 independent elements $\left(\varepsilon_{ij} = \varepsilon_{ji}\right)$ and is represented using a 3×3 matrix.

Using the engineering notation described above, the strain-charge equation in matrix form is given in equation (2.3) [30].

$$\begin{bmatrix} S \\ D \end{bmatrix} = \begin{bmatrix} s^E & d^t \\ d & \varepsilon^T \end{bmatrix} \begin{bmatrix} T \\ E \end{bmatrix} \tag{2.3}$$

In this equation, S, T, D, and E are the strain, stress, electric displacement, and electric field vectors respectively, s^E is the compliance matrix under constant electric field, d is the piezoelectric strain coefficient matrix, ε^T is the permittivity matrix under constant stress, superscript t denotes matrix transpose and contracted notation is used as given below.

$$S = \begin{bmatrix} S_1 \\ S_2 \\ S_3 \\ S_4 \\ S_5 \\ S_6 \end{bmatrix} = \begin{bmatrix} S_{11} \\ S_{22} \\ S_{33} \\ 2S_{23} \\ 2S_{13} \\ 2S_{12} \end{bmatrix}, T = \begin{bmatrix} T_1 \\ T_2 \\ T_3 \\ T_4 \\ T_5 \\ T_6 \end{bmatrix} = \begin{bmatrix} T_{11} \\ T_{22} \\ T_{33} \\ T_{23} \\ T_{13} \\ T_{12} \end{bmatrix}, D = \begin{bmatrix} D_1 \\ D_2 \\ D_3 \end{bmatrix}, \text{and } E = \begin{bmatrix} E_1 \\ E_2 \\ E_3 \end{bmatrix}. \tag{2.4}$$

The compliance, permittivity, and piezoelectric strain constant matrices for materials with the wurtzite crystal structure, e.g. AlN, are given below.

$$s = \begin{bmatrix} s_{11} & s_{12} & s_{13} & 0 & 0 & 0 \\ s_{12} & s_{11} & s_{13} & 0 & 0 & 0 \\ s_{13} & s_{13} & s_{33} & 0 & 0 & 0 \\ 0 & 0 & 0 & s_{44} & 0 & 0 \\ 0 & 0 & 0 & 0 & s_{44} & 0 \\ 0 & 0 & 0 & 0 & 0 & 2\left(s_{11} - s_{12}\right) \end{bmatrix} \tag{2.5}$$

$$\varepsilon = \begin{bmatrix} \varepsilon_{11} & 0 & 0 \\ 0 & \varepsilon_{11} & 0 \\ 0 & 0 & \varepsilon_{33} \end{bmatrix} \tag{2.6}$$

$$d = \begin{bmatrix} 0 & 0 & 0 & 0 & d_{15} & 0 \\ 0 & 0 & 0 & d_{15} & 0 & 0 \\ d_{31} & d_{31} & d_{33} & 0 & 0 & 0 \end{bmatrix} \tag{2.7}$$

Under plane stress assumptions we can neglect the normal stress $\left(T_3 = 0\right)$ and the corresponding shear stress components $\left(T_4 = 0 \text{ and } T_5 = 0\right)$ in the thin plate resulting in the reduced equations as follows.

$$\begin{bmatrix} S_1 \\ S_2 \\ S_6 \\ D_3 \end{bmatrix} = \begin{bmatrix} s_{11}^E & s_{12}^E & 0 & d_{31} \\ s_{12}^E & s_{11}^E & 0 & d_{31} \\ 0 & 0 & s_{66}^E & 0 \\ d_{31} & d_{31} & 0 & \varepsilon_{33}^T \end{bmatrix} \begin{bmatrix} T_1 \\ T_2 \\ T_6 \\ E_3 \end{bmatrix} \tag{2.8}$$

It is worth noting that, in this case, the electric displacement field in the normal direction to the plate $\left(D_3\right)$ is proportional to the sum of the in-plane stress fields $\left(T_1 + T_2\right)$ assuming zero electric field. We will see in the next section that this is an important consideration in selecting the vibration modes with large transduction efficiency for sensing applications.

2.2. High-Frequency Piezoelectrically Transduced Gyroscopes

Conventional vibratory rate gyroscopes use a pair of low-frequency rigid-body resonance modes in a microstructure for rotation rate detection by actuating the primary resonance mode of the device and detecting the rate-proportional Coriolis displacement signal along the secondary resonance mode. Although these vibratory gyroscopes provide the degree of functionality required by some consumer applications, they fail to offer the performance level demanded by many high-end applications, such as short-range inertial navigation, while maintaining a micro-scale physical size. By taking advantage of the stiff bulk resonance modes of the device structure, high-frequency resonant bulk acoustic wave (BAW) gyroscopes [31, 32] have overcome many limitations of low-frequency gyroscopes, such as vibration sensitivity, susceptibility to mechanical shock, and inadequate bandwidth and dynamic range under mode-matched conditions. However, the rotation rate scale factor of these devices decreases at higher resonance frequencies due to the smaller vibration amplitude. Capacitive BAW gyroscopes utilize submicron air gaps and large DC voltages to provide efficient transduction and at high frequencies. They also require vacuum encapsulation to avoid squeeze-film damping, which in turn necessitates special design considerations for co-integration of capacitive gyroscopes with static accelerometers, where low-pressure requirements for gyroscope packaging conflicts with the desired over-damped performance of the accelerometer needed for fast settling time and small overshoot [33]. Implementation of BAW gyroscopes that can provide efficient in-air transduction to minimize packaging complexity of multi-degree-of-freedom sensors, without the need for narrow gaps and large DC polarization voltages to further reduce fabrication cost and high voltage requirements of the sensor, is the main goal of this research. Inherent linearity and high efficiency of the piezoelectric transduction combined with superior power handling of thick single-crystal silicon acoustic platform facilitate actuation of the piezo-on-silicon gyroscopes with adequate vibration amplitudes, paving the way towards significant enhancement of rotation rate scale factor and total signal-to-noise ratio.

2.2.1. In-Plane Flexural Vibration Mode Shapes

High-frequency capacitive gyroscopes typically use the in-plane elliptical bulk resonance modes of a disk microstructure to enable Coriolis energy transfer between the two degenerate modes. However, the stress-field pattern of such mode shapes prevents their efficient transduction by top-surface piezoelectric thin films. Identifying distinct resonance modes that not only allow for piezoelectric transduction but also demonstrate gyroscopic coupling is key to the implementation of high-frequency piezoelectric gyroscopes. We have identified that the degenerate in-plane flexural mode pair of a plate structure with four-fold rotational symmetry exhibits both properties and utilized it to realize a piezoelectrically transduced Coriolis BAW gyroscope.

The basic structure with four-fold symmetry which supports degenerate in-plane flexural mode shapes is a square plate with the vibration mode shapes shown in Figure 2.1.

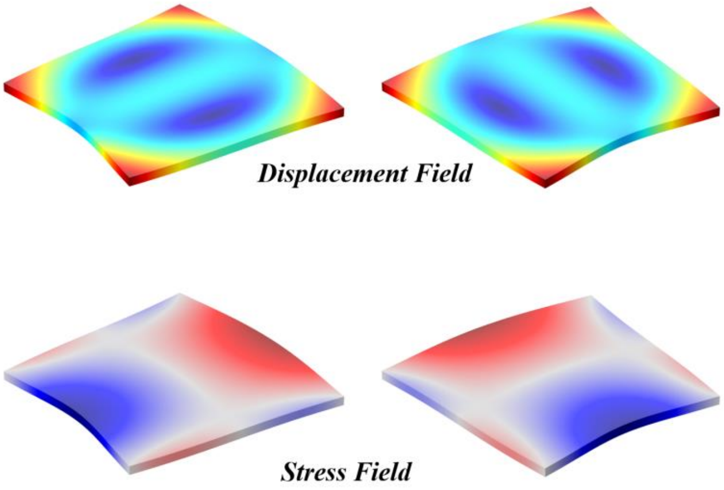

Figure 2.1: Displacement field (top) and stress field (bottom) for the in-plane flexural vibration mode shape of a square structure

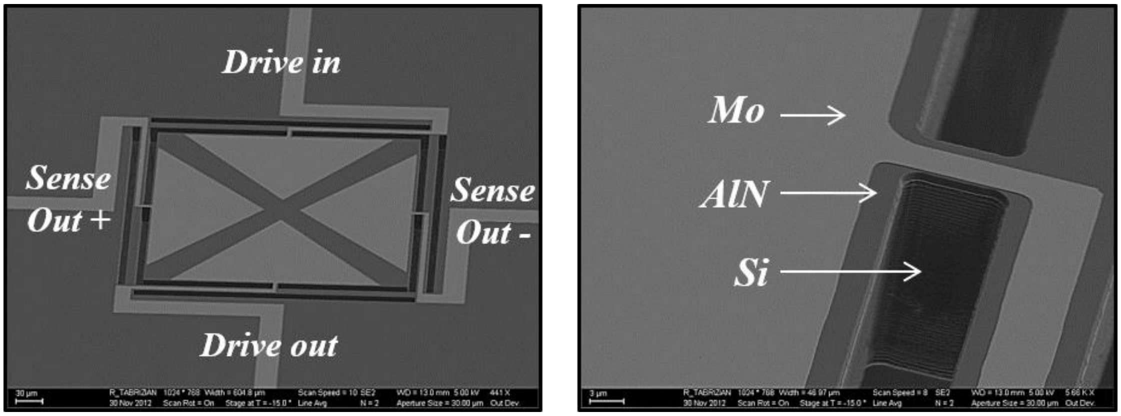

Figure 2.2: AlN-on-Si resonant square gyroscope with triangular electrode placements for efficient drive mode excitation and sense mode decoupling (left) and the piezoelectric stack on the thick silicon substrate (right)

To better visualize this mode shape, we can think of it as the bending vibration mode of a free-free slender rectangular beam with a length to width ratio that is reduced to one to form the square plate.

The stress-field pattern of this vibration mode allows for efficient transduction of the drive mode and placing the sense mode electrodes 90 degrees apart from drive mode electrodes ensures decoupling between the two modes by charge cancellation as shown in Figure 2.2 [34].

Among many possible geometric structures with four-fold rotational symmetry which support the in-plane flexural vibration modes, disk and annular structures are very suitable for laying out top-surface electrodes and designing the supporting anchors around their periphery [35]. The degenerate in-plane flexural mode shapes of the disk and annulus resonator are shown in Figure 2.3 and Figure 2.4. Their stress field is very similar to that of the square resonators which again allows for efficient transduction.

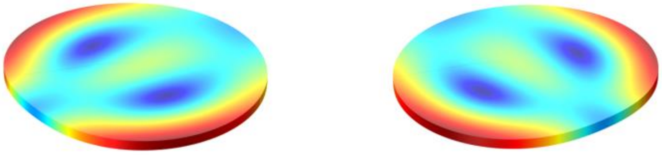

Displacement Field

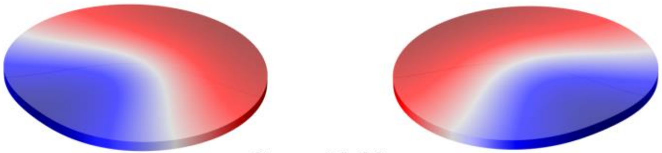

Stress Field

Figure 2.3: Displacement field (top) and stress field (bottom) for the in-plane flexural vibration mode shape of a disk structure

We will see in the next chapter that the minimum number of four electrodes needed for the operation of these devices are not enough for the implementation of the mode matching algorithm for piezoelectric gyroscopes and so the disk or annulus structures are

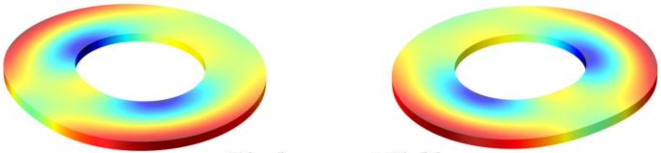

Displacement Field

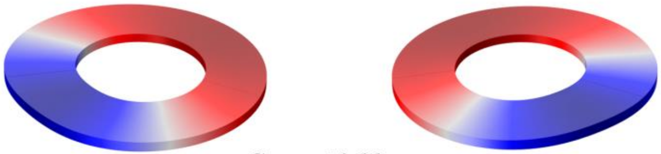

Stress Field

Figure 2.4: Displacement field (top) and stress field (bottom) for the in-plane flexural vibration mode shape of an annulus structure

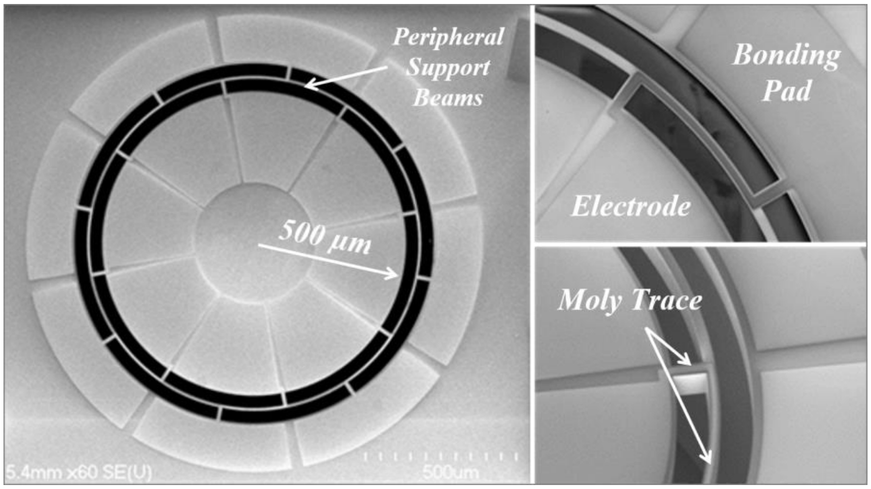

Figure 2.5: AlN-on-Si resonant disk gyroscope with eight identical top electrodes and double-T supports around its periphery along with close up views of the support structure and routing

favored in terms of electrode and anchor design. Figure 2.5 shows an AlN-on-Si disk gyroscope with eight identical top electrodes for orthogonal actuation and sensing, and sixteen circularly symmetric peripheral T-supports to ensure no structural asymmetry and provide a path for electrodes routing [36].

It is worth noting here that the higher-order in-plane flexural vibration modes are also degenerate gyroscopic modes which can likewise be transduced efficiently using a top-surface piezoelectric layer. It is needless to say that the higher order modes occur at much higher frequencies which can provide benefits in terms of providing larger mode matched operation bandwidth. The physical angular distance between the two degenerate gyroscopic modes ($^{90^\circ}\!/_{m}$, *m*: mode order) decreases as the order of the vibration mode increases. Figure 2.6 shows the first three mode shapes for the disk and annulus structures. Notice that the higher-order flexural modes of the disk have a nodal point at the center which could be favorable in terms of anchoring the device.

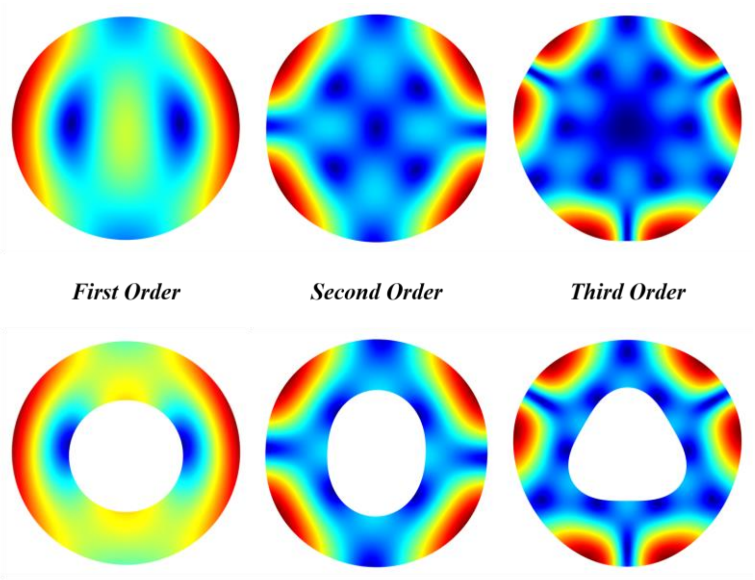

Figure 2.6: First three in-plane flexural vibration modes of the disk and annulus structures

2.2.2. Effective Mass of the In-Plane Flexural Resonator

Apart from the rigid-body translational mode resonators where the entire body of the resonator undergoes the same displacement, the effective mass of a resonator, which is the equivalent mass used in lump-element modelling of the resonator is a fraction of the total physical mass of the resonator structure and a function of the mode shape. The effective mass of a mechanical resonator is defined as the equivalent point mass usually in the direction of maximum displacement given in equation (2.9) as the volumetric integration of the resonator density weighted by the displacement field. It is assumed here that the magnitude of the displacement field vector is normalized.

$$m_{eff} = \iiint_V \rho \left|\vec{u}\right|^2 dV \tag{2.9}$$

The effective mass coefficient is defined as the effective mass divided by the physical mass of the resonator. The effective mass coefficients of the in-plane flexural

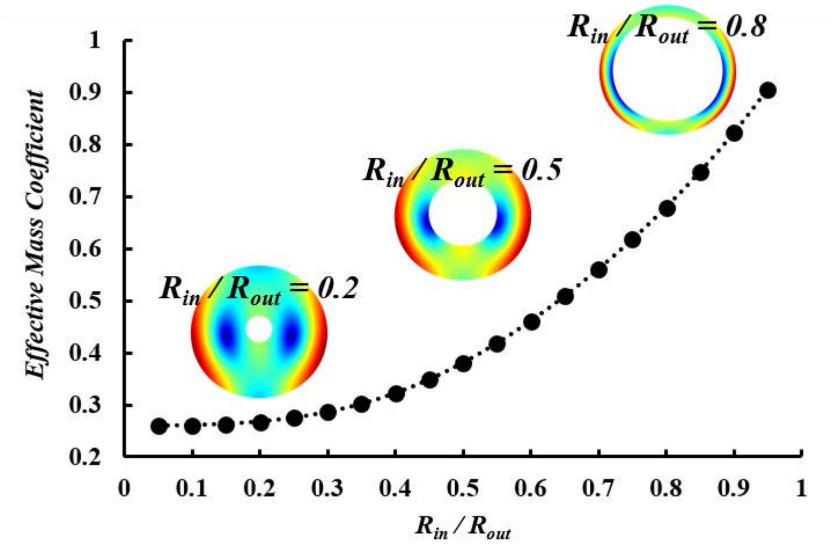

Figure 2.7: Effective mass coefficient of the in-plane flexural annulus resonator as a function of the inner to outer radius of the annulus

square and disk resonators are ~0.11 and ~0.26 respectively as simulated using COMSOL Multiphysics finite-element analysis (FEA) software.

Figure 2.7 shows the simulated effective mass coefficient for the annular in-plane flexural resonator as a function of the inner to outer radius of the annulus. As we can see, the coefficient improves as the annular structure becomes narrower and approaches unity as the width of the annulus tends to zero.

At a fixed resonant frequency, it is desired to design resonant gyroscopes with the largest mass possible to reduce the thermomechanical noise of the device. Considering that the resonant frequency of the annular in-plane flexural resonator is not a strong function of the inner radius and taking into account the size limitation in the design process, it is helpful to compare the effective mass of the annular resonators for different widths. Figure 2.8 shows the effective mass normalized to the maximum value as a function of the inner to

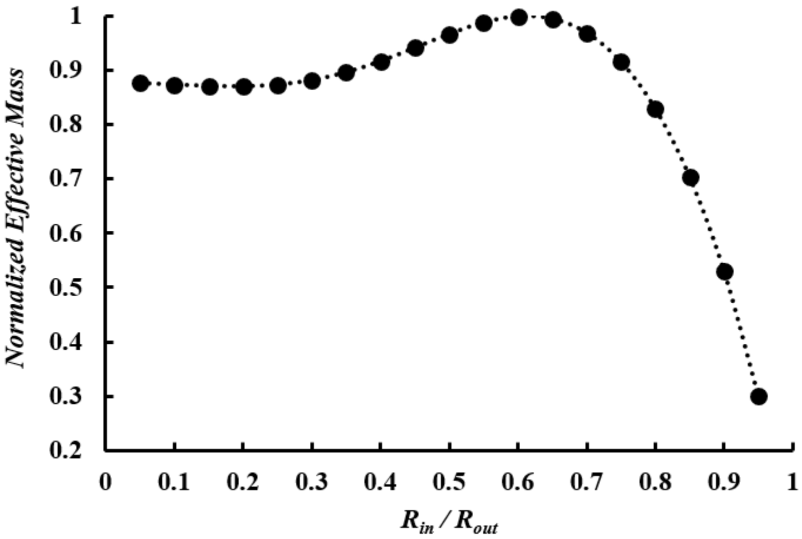

Figure 2.8: Normalized effective mass of the in-plane flexural annulus gyroscope as a function of the inner to outer radius of the annulus

outer radius of the annulus. The maximum effective mass occurs at a ratio of ~ 0.62 or if we consider the ratio of the outer to inner radius of the annulus the maximum effective mass occurs at a ratio of ~1.62. This number might be aesthetically discernible to possibly be related to the Golden Ratio.

2.2.3. Electromechanical Coupling Coefficient

Adoption of the in-plane flexural vibration mode pair for implementation of piezoelectric-on-silicon gyroscopes is critical in the sense that the elliptical modes commonly used in electrostatic gyroscopes do not provide strong electromechanical coupling through top-surface piezoelectric transduction. The weak coupling of the elliptical modes can be explained by their in-plane stress field distribution. Figure 2.9 compares the in-plane stress field components and their summation for the flexural and elliptical modes. We know from equation (2.8) that the sum of the in-plane stress

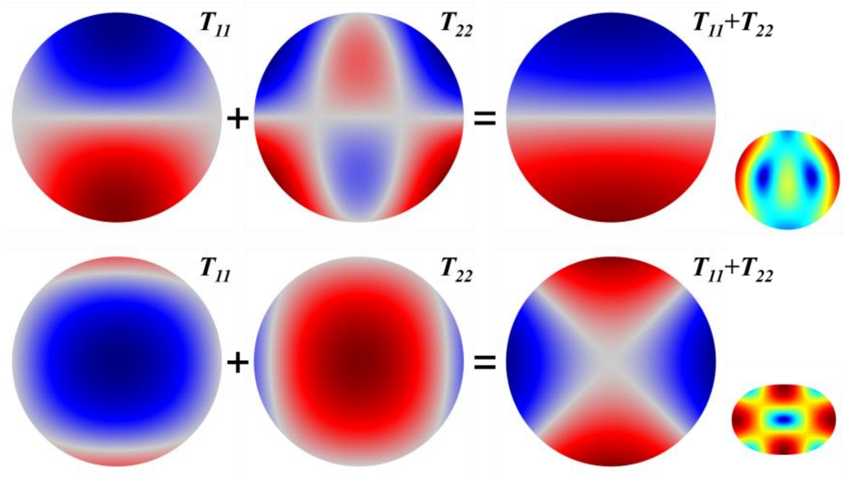

Figure 2.9: In-plane components of the stress field for the flexural (top) and elliptical (bottom) vibration modes showing the favored stress pattern of the flexural mode for top-surface piezoelectric transduction.

components determines the surface charge density. The in-plane stress components of the elliptical mode mostly cancel one another out as opposed to the stress components of the flexural mode and therefore provide much less efficient transduction.

Electromechanical coupling coefficient is a measure of the strength or efficiency of the transduction between the electrical and mechanical domains and is defined as the ratio of the mechanical force to the electrical voltage or the ratio of the electrical current to mechanical velocity as given in equation (2.10).

$$\eta = \frac{f}{V} = \frac{I}{\dot{q}} \tag{2.10}$$

This coupling coefficient is a function of the material properties, vibration mode shape, and geometric size of the resonator. Since there is no closed-form solution for the in-plane flexural vibration mode shapes we cannot derive an analytical expression for the electromechanical coupling coefficients of these resonators. However, it is possible to make a comparison between the coupling coefficients of the piezoelectrically transduced flexural and elliptical resonator using electrical and mechanical model parameters obtained from FEA simulations.

The effective stiffness, mass, and damping parameters and the motional capacitance, inductance, and resistance of electromechanical resonators are related by the electromechanical coupling coefficient as given in equations (2.11) below.

$$\begin{aligned} k_{eff} &= \eta^2 / C \\ m_{eff} &= \eta^2 L \\ b_{eff} &= \eta^2 R \end{aligned} \tag{2.11}$$

Considering that we can easily compute the effective mass and motional resistance using finite-element analysis, equation (2.12) can be used to calculate and compare the electromechanical coupling coefficients for different resonators. It is important to note that the coupling coefficient is independent of the resonator quality factor.

$$\eta^2 = \frac{m_{eff}\,\omega_o}{QR} \tag{2.12}$$

COMSOL simulation results show that η^2 is more than 20 times larger for an in-plane flexural disk resonator compared with an elliptical disk resonator of the same size and equal transduction area. This ratio increases much more for annular resonators such that η^2 can be more than 100 times larger for the flexural annular resonator compared with the elliptical annular resonator which translates to significant improvements in motional resistance, rate sensitivity, and thermomechanical noise performance of the gyroscope device.

2.2.4. *Gyroscopic Coupling Coefficient*

In section 1.2, we assumed perfect gyroscopic coupling between the two gyroscope vibration modes in presenting the Coriolis force equation and deriving subsequent relationships. However, for vibration modes with nonuniform displacement field over the body of the resonator, the effect of nonuniformity of the displacement field must be considered for lump-element modeling of the gyroscopic system and so the coupling coefficient λ is introduced to correct the Coriolis force equation as given below where $\overrightarrow{\Omega}$ is the rotation rate vector and $\vec{q}$ is the generalized displacement.

$$\overrightarrow{f}_{Cor} = 2m_{eff}\lambda\overrightarrow{\Omega}\times\dot{\vec{q}} \tag{2.13}$$

The gyroscopic coupling coefficient is defined as the volumetric integral of the cross product of the two displacement fields projected in the direction of the rotation rate vector as given in equation (2.14) where $\overrightarrow{u_1}$ and $\overrightarrow{u_2}$ denote the normalized displacement fields of the two gyroscopic vibration modes and a_Ω represents the unit vector in the direction of rotation.

$$\lambda = \iiint_V \left|(\overrightarrow{u_1}\times\overrightarrow{u_2})\cdot a_\Omega\right| dV \tag{2.14}$$

It is important to note that this definition assumes a uniform density function. If the density of the resonator is not uniform, a more general definition can be given by combining the effective mass and coupling coefficient definitions as follows.

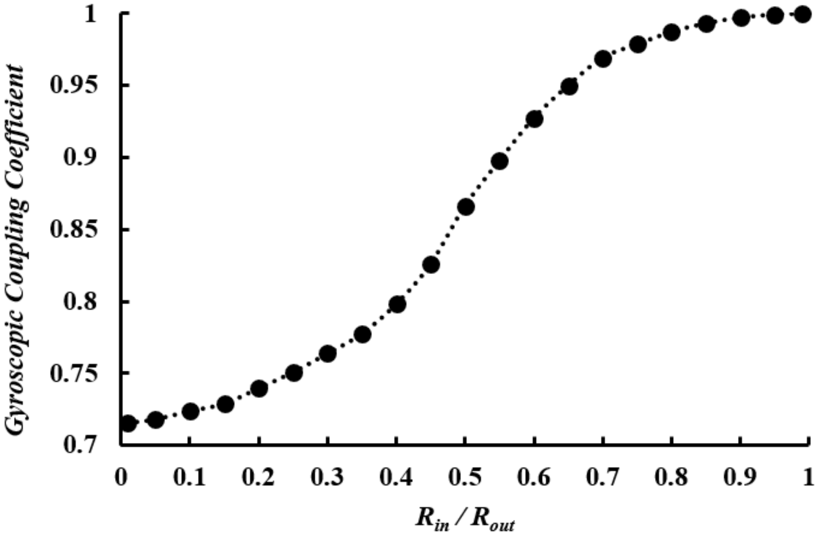

Figure 2.10: Gyroscopic coupling coefficient of the in-plane flexural annular gyroscope as a function of the inner to outer radius of the annulus

$$m_{eff}\lambda = \iiint\limits_V \rho \left| (\overrightarrow{u_1} \times \overrightarrow{u_2}) \cdot a_\Omega \right| dV \tag{2.15}$$

Figure 2.10 shows the gyroscopic coupling coefficient of the in-plane flexural annular gyroscope as a function of the inner to outer radius of the annulus as obtained from COMSOL simulations. The Coriolis coupling is higher than 90% if the inner radius is at least 60% of the outer radius which is larger than that for elliptical mode gyroscopes. The simulated gyroscopic coupling coefficient for the in-plane flexural square and disk gyroscopes are ~0.60 and ~0.72 respectively.

2.3. AlN-on-Silicon Fabrication Process

The cross-sectional view of the four-mask fabrication process for the piezoelectric resonant device is depicted in Figure 2.11. The process begins with the deposition of the piezoelectric stack, which consists of a thin film of sputtered AlN sandwiched between a top signal molybdenum (Mo) layer and a bottom ground Mo layer, on a silicon-on-insulator substrate. Next, the top Mo electrode layer is patterned to define the signal electrodes and connection pads on and around the device. Then, a PECVD oxide layer is deposited on the backside of the wafer and patterned for subsequent handle-layer etching. After that, the AlN layer is patterned to open access paths to the bottom Mo layer for ground connections. In the next step, the device structure is defined by etching trenches through the AlN, bottom Mo, and Si device layers. Subsequently, the silicon handle layer is etched for backside release of the structure using the previously patterned backside oxide layer. Finally, the device is released with a short step of HF oxide etch.

The Mo layer is etched in an RIE tool using SF_6 and O_2 gasses. AlN can be wet etched using TMAH or dry etched in an ICP-RIE tool using a Cl_2-based chemistry. It is more convenient to wet etch AlN to create openings to the bottom Mo layer as the etching stops at the Mo layer. However, to define the device structure, dry etching of the AlN layer is beneficial. Si device and handle layers are also etched using the standard Bosch process.

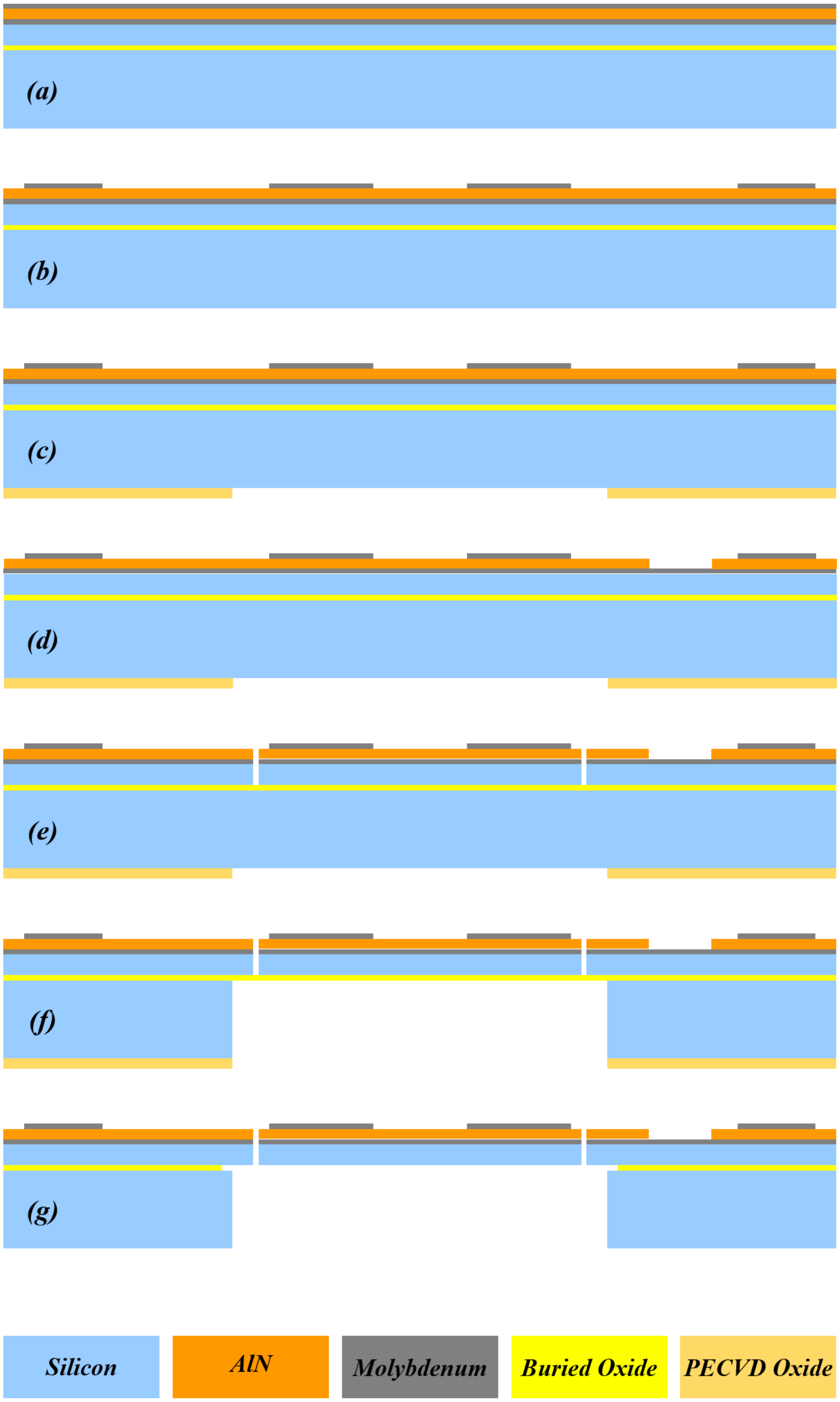
(a)
(b)
(c)
(d)
(e)
(f)
(g)
Silicon
AlN
Molybdenum
Buried Oxide
PECVD Oxide

Figure 2.11: AlN-on-Si fabrication process flow. (a) deposit the piezoelectric stack on the SOI wafer, (b) pattern the top Mo layer, (c) deposit and pattern backside oxide layer, (d) etch AlN for access to bottom Mo layer, (e) etch AlN, bottom Mo, and Si device layers to define the device structure, (f) etch Si handle layer for backside release, (g) release the device in HF.

CHAPTER 3. MODE MATCHING OF RESONANT PIEZOELECTRIC GYROSCOPES

"Over earth and ocean, with gentle motion, this pilot is guiding me." – Percy Bysshe Shelley

Resonant gyroscopes operate based on the transfer of energy between two gyroscopic modes due to the Coriolis effect. Ideally, the resonance frequency of the drive and sense modes of the gyroscope are identical resulting in Q-amplification of the sense signal and thus giving rise to improved signal-to-noise ratio and relaxed specification requirements for the interface circuitry. Moreover, the two mechanical modes of an ideal gyroscope are completely aligned with the direction of transduction resulting in the decoupling of the sense and drive signals and perfect bias stability of the sensor. In practice however, because of the nonidealities of the fabrication process and imperfect material properties, the resonance frequencies of the two modes of the gyroscope are mismatched and the gyroscopic modes are misaligned resulting in performance degradation. The process of frequency matching and modal alignment of the vibration modes of a resonant gyroscope is referred to as mode matching.

It is possible to correct the mismatches and misalignments of a device by permanent trimming of the modal parameters through mass and stiffness perturbation [37-39]. However, maintaining mode matching under different operation conditions of the gyroscope requires a real-time tuning technique. Capacitive resonant gyroscopes take advantage of the electrostatic spring softening mechanism to tune the device parameters and achieve mode matching by controlling DC tuning voltages across narrow capacitive gaps [40]. All-piezoelectric gyroscopes, however, require alternative techniques for frequency matching and modal alignment that can be applied independently of electrostatic transduction.

3.1. Eigenmode Operation of Piezoelectric Devices

Conventional modal alignment techniques are based on cancelling the vibration parameters that cause cross-coupling between the two modes of gyroscope. These cross-coupling terms are defined according to the direction of transduction electrodes. Therefore, cancelling them in effect corrects the direction of vibration of gyroscopic modes. Considering the difficulties of modal parameter adjustments with piezoelectric transduction, modal alignment of these devices necessitates rethinking the approaches to mode matching of resonant gyroscopes.

A resonant gyroscope is a four-port device consisting of input and output ports for the drive and sense vibration modes. Therefore, we can study its frequency response by exciting the input port of each mode and observing the response at the output port of the same mode (direct response) as well as the output port of the other mode (indirect response). In an ideal gyroscope, the direct response is similar to the response of a single resonator and the indirect response is zero. If we consider modal misalignment and frequency mismatch, we will see the appearance of both peaks in the direct response and a non-zero indirect response. Figure 3.1 shows the frequency response of an annular piezoelectric gyroscope with 16 excitation and readout electrodes making it possible to measure the response of the device at four different directions.

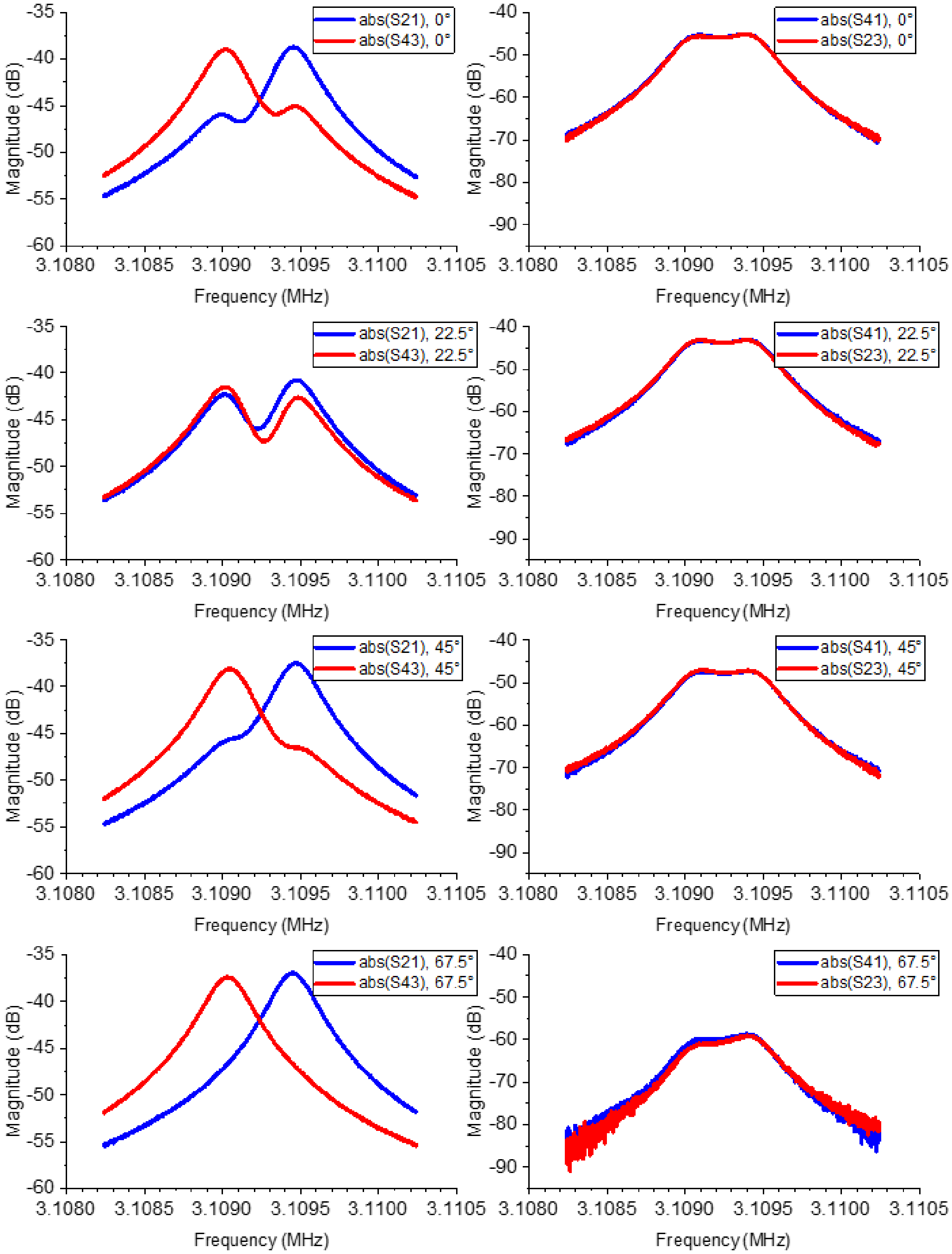

Figure 3.1: Frequency response of annular piezoelectric gyroscope with 16 identical top electrodes measured making it possible to measure the response around the annulus at every 22.5°. The level of the indirect response, which is a measure of modal coupling, changes as the angle of measurement changes.

These measurement results provide an important observation that transpires to be key in the development of the modal alignment technique for piezoelectric gyroscopes. As we can see, the level of the indirect response or modal coupling changes as the direction of excitation and readout changes. At some angel the coupling is reduced by ~15 dB and the second peak disappears from the direct response. As we will see in the next section, modal decoupling of the piezoelectric gyroscopes can be achieved by changing the transduction direction instead of correcting the direction of vibration modes. We herein refer to this method of modal alignment as the eigenmode operation of resonant gyroscopes [41, 42].

3.1.1. Theory of Eigenmode Operation

Coriolis vibratory gyroscopes are often modeled with a second-order system of differential equations, as shown below,

$$[M]\{\ddot{q}\}+[B]\{\dot{q}\}+[K]\{q\}=\{Q\} \tag{3.1}$$

where $[M]$, $[B]$, and $[K]$ are the mass, damping and stiffness matrices defining the gyroscopic system, $\{q\}$ is the generalized coordinate vector, and $\{Q\}$ is the forcing vector. In an ideal vibratory gyroscope, energy is coupled between the two resonant modes only due to an applied external rotation. However, in practice, because of misalignment of the vibration direction with respect to the location of the input and output electrodes, energy is transferred between the two modes even in the absence of an external rotation signal. This coupling effect is modeled in the equations of motion of the gyroscope by introducing off-diagonal terms in the stiffness and damping matrices to cross-couple force to displacement and velocity between the two modes. The mismatch between the resonant frequencies of the two vibration modes is also modeled by the introduction of a stiffness mismatch term as given below,

$$\begin{bmatrix} m & 0 \\ 0 & m \end{bmatrix}\begin{Bmatrix} \ddot{q}_1 \\ \ddot{q}_2 \end{Bmatrix}+\begin{bmatrix} b-\Delta b & b_{12}-2m\Omega \\ b_{12}+2m\Omega & b+\Delta b \end{bmatrix}\begin{Bmatrix} \dot{q}_1 \\ \dot{q}_2 \end{Bmatrix}+\begin{bmatrix} k-\Delta k & k_{12} \\ k_{12} & k+\Delta k \end{bmatrix}\begin{Bmatrix} q_1 \\ q_2 \end{Bmatrix}=\begin{Bmatrix} Q_1 \\ Q_2 \end{Bmatrix} \tag{3.2}$$

where q_1, q_2, Q_1, and Q_2 are the generalized coordinate and force components defined in the physical direction of gyroscope excitation and readout; m, b, and k are the mass, damping, and stiffness coefficients for both modes; Δb and Δk represent the damping and stiffness mismatches between the two modes; b_{12} and k_{12} represent the damping and stiffness cross-coupling between the two modes; and Ω is the magnitude of the angular velocity vector, which is perpendicular to the plane of general coordinates.

First, let us consider the case without mechanical damping where in the absence of an external rotation signal, the damping matrix reduces to zero. Considering zero forcing, we arrive at the homogeneous equation (3.3), which provides insight into the natural behavior of the system.

$$[M]\{\ddot{q}\}+[K]\{q\}=\{0\} \tag{3.3}$$

The solution to the above homogeneous equation is of the form $\{q\}=\mathrm{Re}\left(B\{\phi\}e^{j\omega t}\right)$. Substituting this form into equation (3.3), we arrive at the following eigenvalue problem.

$$\left([K]-\omega^2[M]\right)\{\phi\}=\{0\} \tag{3.4}$$

Solving equation (3.4) results in the eigenfrequencies and eigenmodes of the system.

$$\omega_1 = \sqrt{\frac{k - \sqrt{\Delta k^2 + {k_{12}}^2}}{m}}, \omega_2 = \sqrt{\frac{k + \sqrt{\Delta k^2 + {k_{12}}^2}}{m}} \tag{3.5}$$

$$\{\phi_1\} = \begin{Bmatrix} 1 \\ \dfrac{\Delta k - \sqrt{\Delta k^2 + {k_{12}}^2}}{k_{12}} \end{Bmatrix}, \{\phi_2\} = \begin{Bmatrix} 1 \\ \dfrac{\Delta k + \sqrt{\Delta k^2 + {k_{12}}^2}}{k_{12}} \end{Bmatrix} \tag{3.6}$$

Equations (3.5) and (3.6) give the natural frequencies and natural directions of the vibration for a vibratory gyroscope with stiffness mismatch and cross-coupling between the two modes. It is important to note that even in the absence of any stiffness mismatch, the two vibration modes will still have different resonance frequencies due to stiffness cross-coupling between the two modes. It is also informative to consider the eigenvector directions for the two extreme cases where only the stiffness mismatch is set to zero or where only the stiffness cross-coupling is set to zero. The former case results in eigenmodes that are in the direction of the generalized coordinates or, in other words, in the physical direction of transduction electrodes, whereas the latter case results in eigenmodes that are 45 degrees away from the direction of the transduction electrodes, which corresponds to equal direct and indirect coupling between the two modes. Figure 3.2 shows the simulated magnitude of the drive and sense modes of a gyroscope, with the gyroscopic modal parameters defined along the horizontal and vertical axes, for different cases of stiffness mismatch and cross-coupling as discussed above. The angle of transduction is swept around the device for each case and the magnitude of the drive and sense mode outputs are depicted.

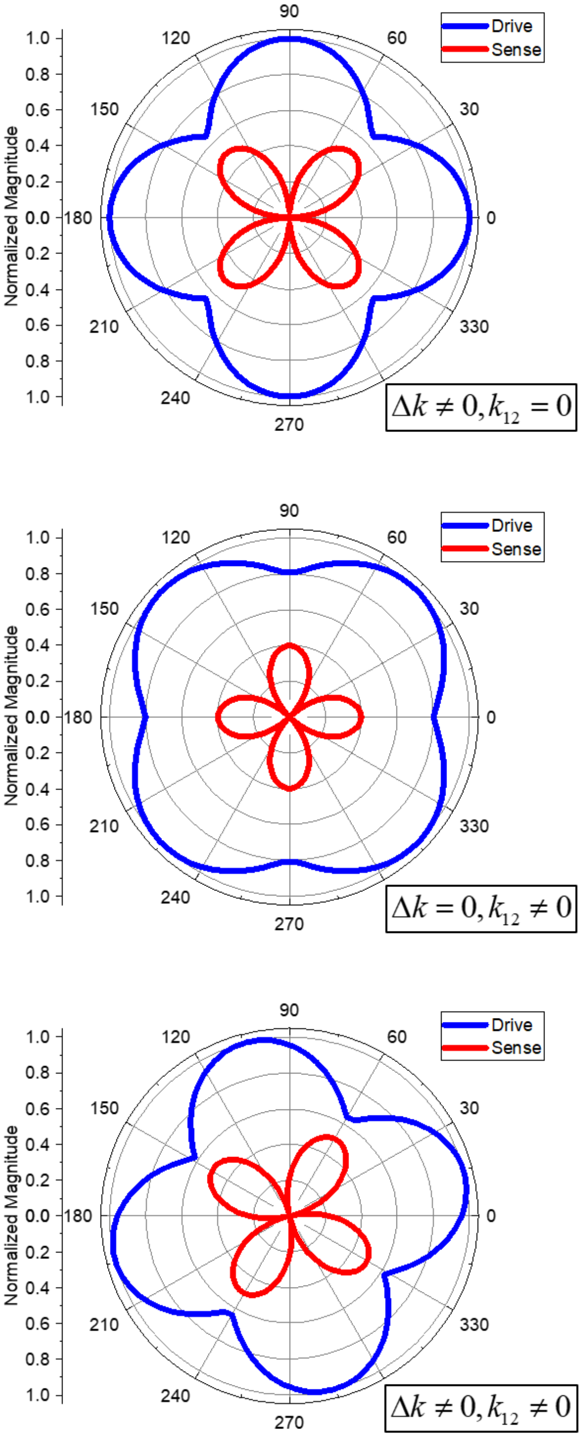

Figure 3.2: Simulated magnitude of the drive and sense modes of a gyroscope for different cases of modal coupling and frequency mismatch. The eigenmode direction is where the drive response is maximum, and the sense response approaches zero.

As we can see, the eigenmode direction, identified as the direction along which the drive mode response is maximum and the zero-rate output (ZRO) of the sense mode is minimum, changes from 0° to 45° depending on the level of mismatch and cross-coupling between the two modes and lies in between these two angles in general.

To take advantage of the orthogonality of the eigenmodes, the modal masses μ_1 and μ_2 can be defined as given below [43].

$$\mu_1 = \{\phi_1\}^T [M]\{\phi_1\}, \mu_2 = \{\phi_2\}^T [M]\{\phi_2\} \tag{3.7}$$

The eigenvectors can be normalized by the modal masses to define the normal modes $\{\Phi_1\}$ and $\{\Phi_2\}$, and the normal mode matrix $[\Phi]$ as follows.

$$\{\Phi_1\} = \frac{1}{\sqrt{\mu_1}}\{\phi_1\}, \{\Phi_2\} = \frac{1}{\sqrt{\mu_2}}\{\phi_2\} \tag{3.8}$$

$$[\Phi] = [\{\Phi_1\}\{\Phi_2\}] \tag{3.9}$$

The normal modes are orthogonal with respect to the mass and stiffness matrices, as shown in equations (3.10) and (3.11),

$$[\Phi]^T [M][\Phi] = [I] \tag{3.10}$$

$$[\Phi]^T [K][\Phi] = [\omega_{nat}{}^2] \tag{3.11}$$

where $[I]$ is the identity matrix and $[\omega_{nat}{}^2]$ is a diagonal matrix consisting of the square of the eigenfrequencies. Based on the normal mode matrix, the following linear transformation between the generalized coordinates $\{q\}$ and the modal coordinates $\{\eta\}$ can be considered.

$$\{q\} = [\Phi]\{\eta\} \tag{3.12}$$

Substituting for $\{q\}$ in the differential equations of motion of the gyroscope, we obtain

$$[M][\Phi]\{\ddot{\eta}\} + [K][\Phi]\{\eta\} = \{Q\}. \tag{3.13}$$

Left-multiplying (3.13) with the transpose of the normal mode matrix, $[\Phi]^T$, and applying the orthogonality properties in (3.10) and (3.11) results in the diagonalization of the mass and stiffness matrices. In other words, the modal cross-coupling is removed under normal modal transformation.

$$\{\ddot{\eta}\} + \left[\omega_{nat}{}^2\right]\{\eta\} = [\Phi]^T \{Q\} \tag{3.14}$$

3.1.2. Principles of Eigenmode Operation

The reason for the appearance of zero-rate error, or more specifically quadrature error, in the response of resonant gyroscopes is the existence of off-diagonal terms in the system of equations of motion that cause coupling of the two vibration modes. This misalignment of the mode shape with respect to the transduction direction is commonly corrected by aligning the direction of vibration to the transduction direction via application of electrostatic forces, as shown in Figure 3.3a.

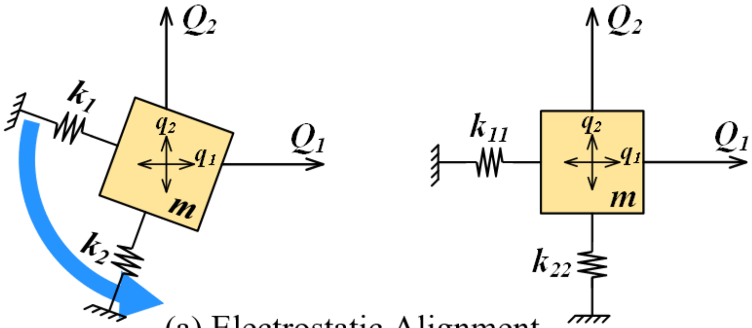

(a) Electrostatic Alignment

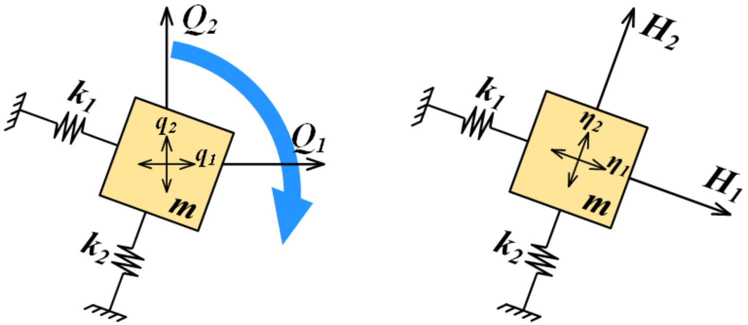

(b) Eigenmode Operation

Figure 3.3: Schematic representation of modal alignment techniques. (a) The electrostatic alignment technique corrects the misalignment in the stiffness direction to remove quadrature coupling. (b) Eigenmode operation adjusts the excitation and readout directions to the as-fabricated natural vibration direction.

Equation (3.14) represents a new set of modal coordinates, $\{\eta\}$, along which there is no cross-coupling between the two modes of the gyroscope. Therefore, it is alternatively possible to remove the zero-rate error by aligning the transduction direction to the eigenmode direction independent of the transduction mechanism. The method of operating the gyroscope in the direction of the natural vibration modes of the structure or the eigenmode operation is depicted in Figure 3.3b.

The transformation from $\{q\}$ to $\{\eta\}$ is via the transpose of the modal matrix, $[\Phi]^T$ which, in essence, represents a rotation transformation for the gyroscopic system. In other words, there exists a direction in the plane of the original generalized coordinates along which the two modes of the gyroscope are uncoupled. To be strictly accurate, it is worth noting that $\sqrt{m}[\Phi]^T$ is the pure rotation matrix, but the presence of a scaling factor is not crucial to our discussion. The desired forcing vector for uncoupled operation is $\{\mathrm{H}\} = [\Phi]^T \{Q\}$, and the desired readout vector is $\{\eta\} = [\Phi]^T \{q\}$. Therefore, both the excitation and readout directions must be transformed by the $[\Phi]^T$ matrix to ensure decoupling.

To implement the transformation, we can use pairs of electrodes that span the two-dimensional subspace of the plane normal to the axis of rotation for gyroscope excitation and readout. For instance, by applying the scaling coefficients of α and $(1-\alpha)$ to each pair, it is possible to sweep the effective direction of transduction between the two electrodes, in effect creating a set of virtual electrodes that are aligned to the direction of eigenmodes.

Theoretically, the scaling coefficient α is equal at the excitation and readout transducers of the gyroscope. However, to compensate for mismatch effects, the input and output scaling coefficients can be set slightly differently. Additionally, the scaling coefficients applied to the electrodes should be normalized depending on the angle between the electrodes to keep the total magnitude of excitation and readout constant as we sweep the direction of transduction. Assuming an angle of θ between the two members of each electrode pair, the scaling coefficients of α and $(1-\alpha)$ need to be normalized by $\sqrt{2\alpha(\alpha-1)(1-\cos\theta)+1}$ to keep the transduction magnitude constant.

3.1.3. The Effect of Damping on Eigenmode Operation

If the damping matrix is proportional to the mass and stiffness matrices, $[B]=\beta[M]+\gamma[K]$, the same transformation using the normal mode matrix results in the diagonalization of the damping matrix as well as the stiffness matrix [43], which means that the equations of motion will still be uncoupled, and eigenmode operation using the same scaling coefficients removes the zero-rate output, as derived below.

$$[\Phi]^T[M][\Phi]\{\ddot{\eta}\}+[\Phi]^T(\beta[M]+\gamma[K])[\Phi]\{\dot{\eta}\}+[\Phi]^T[K][\Phi]\{\eta\}=[\Phi]^T\{Q\} \tag{3.15}$$

$$\{\ddot{\eta}\}+\left(\beta+\gamma\left[{\omega_{nat}}^2\right]\right)\{\dot{\eta}\}+\left[{\omega_{nat}}^2\right]\{\eta\}=[\Phi]^T\{Q\} \tag{3.16}$$

Because of the axial symmetry of degenerate resonant gyroscopes, it is acceptable to assume that even if the damping matrix is not exactly proportional to the mass and stiffness matrices, it is almost proportional to those matrices. It should be noted that the coupling caused by cross-damping is always 90 degrees apart from that caused by the off-diagonal stiffness terms. Off-diagonal damping terms result in a residual coupled signal that is in phase with the output due to external rotation under mode-matched conditions. Therefore, compensation for this term is not possible without affecting the response of the gyroscope to the rate signal. Measurement results show that the total magnitude of the zero-rate output decreases as the effective direction of transduction approaches the eigenmode

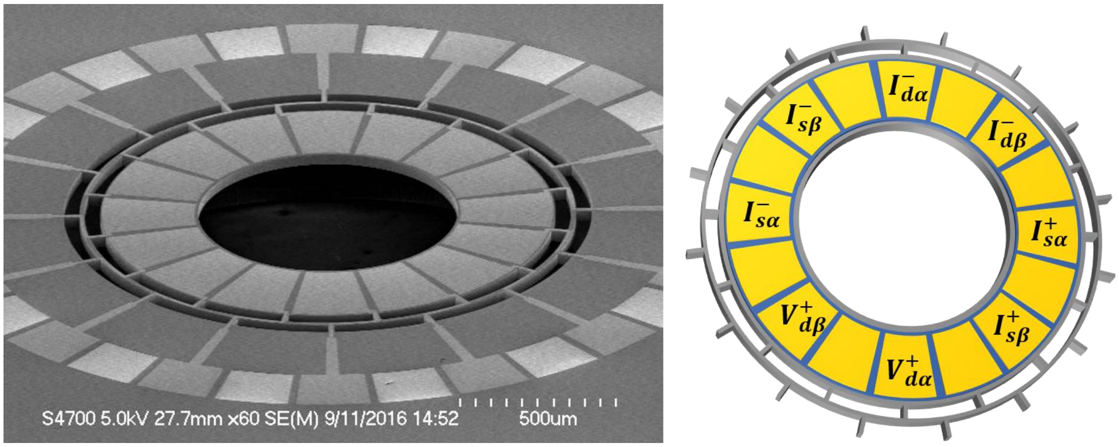

Figure 3.4: SEM image of the AlN-on-Si annular resonant gyroscope with 16 identical top electrodes. Pairs of adjacent electrodes are connected together, reducing the number of independently controlled electrodes to 8, suitable for eigenmode operation of the first in-plane flexural modes.

direction, which suggests that the damping matrix is either almost proportional to the mass and stiffness matrices or that the off-diagonal terms of the damping matrix are very small.

3.1.4. Eigenmode Operation of an AlN-on-Si Resonant Gyroscope

Figure 3.4 shows the SEM image of an AlN-on-Si annular resonant gyroscope whose modes are aligned based on eigenmode operation [44]. The device is comprised of a 1.3 μm thin film of AlN deposited in between 50 nm top and bottom molybdenum (Mo) electrode layers and stacked on top of a 35 μm thick (100) silicon structural layer. The annulus structure has an outer radius of 700 μm, an inner radius of 400 μm, and is anchored to the substrate through a network of 32 circularly symmetric T-supports to ensure structural symmetry of the drive and sense modes. The support structure is also used for routing the electrical signals to the metal electrodes attached to the structure.

To implement eigenmode operation pairs of adjacent electrodes are connected together and 45° apart electrode pairs are used for excitation and readout of the first in-plane flexural vibration modes as depicted in the schematic. The excitation electrodes of the gyroscope are scaled to apply the coefficients of α and $1-\alpha$ with proper normalization factors. The same scaling factors are used to scale the drive output signals and the differential sense output signals to generate the effective drive and sense currents from the pickoff electrodes.

Drive and sense mode response of the gyroscope for different levels of the weighting factor α are shown in Figure 3.5. For $\alpha = 0.8$, the direction of the virtual transduction electrode is closest to the eigenmode direction causing the sense-mode peak to disappear from the drive frequency response and the sense-mode response to be reduced significantly.

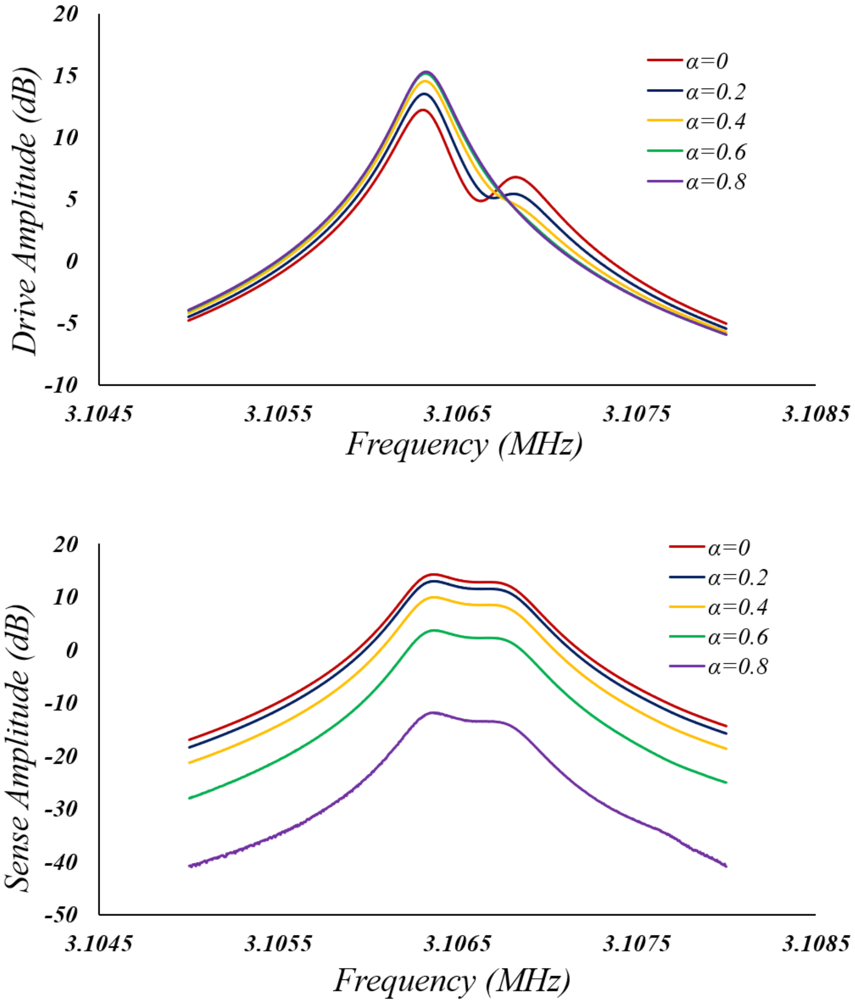

Figure 3.5: Drive and sense mode response of the gyroscope for different levels of the weighting factor α. For $\alpha = 0.8$, the resultant transduction direction is closest to the eigenmode direction; the sense-mode peak disappears from the drive response and the sense-mode amplitude is significantly reduced.

3.2. Resonance Frequency and Quality Factor Tuning of Piezoelectric Devices

Microelectromechanical resonators are usually characterized by their resonance frequency, quality factor, and insertion loss. Controlling these parameters are crucial in many applications as fabrication nonidealities and environmental or aging effects cause undesired temporary or permanent variations of these values [45]. High-precision resonant sensors [46, 47], crystal oscillators [48-50], mechanical filters and duplexers [51], and resonant actuators used in atomic force microscopy [52] are examples of devices that require resonance parameter control for their operation.

Contrary to capacitive resonators that use electrostatic spring softening, control of piezoelectric resonator parameters requires more elaborate implementation. Physical trimming of the resonator structure [53] is a widely used method to control the resonance frequency of piezoelectric devices, especially in the case of mechanical filters. However, trimming is done only once after fabrication and does not provide a means for real-time control of the resonator parameters. Although passive tuning based on changing the termination impedance of piezoelectric resonators [54, 55] has been used successfully to tune the resonance frequency, this technique is not very effective when applied to piezoelectric-on-substrate devices where substrate thickness is considerably larger than the piezoelectric layer thickness. Dynamic or active tuning of resonators [56-58] is a suitable method for controlling the resonance parameters of piezoelectric-on-substrate devices as described in this section.

Active tuning of mechanical resonators is based upon applying forces that are proportional to the displacement or velocity of the resonating body and interfering with the internal stiffness and damping forces of the resonator which results in modulating the effective stiffness and damping coefficients.

It is beneficial to use feedback theory to analyze the effect of active tuning on the response of resonators. Let us consider a second-order resonator system with m, k, and b representing the mass, stiffness and damping of the resonator undergoing a displacement x as force F is applied. Now, let us consider applying a feedback force from the output displacement to the input force with a feedback gain k_D which can be thought of as a dynamic stiffness coefficient as depicted in Figure 3.6. The transfer functions of the two systems along with their resonance frequencies are given in Equations (3.17) and (3.18).

$$H(s) = \frac{\frac{1}{k}}{\left(\frac{s}{\omega_o}\right)^2 + \frac{1}{Q}\frac{s}{\omega_o} + 1} \quad , \quad \omega_{90^\circ} = \omega_o \tag{3.17}$$

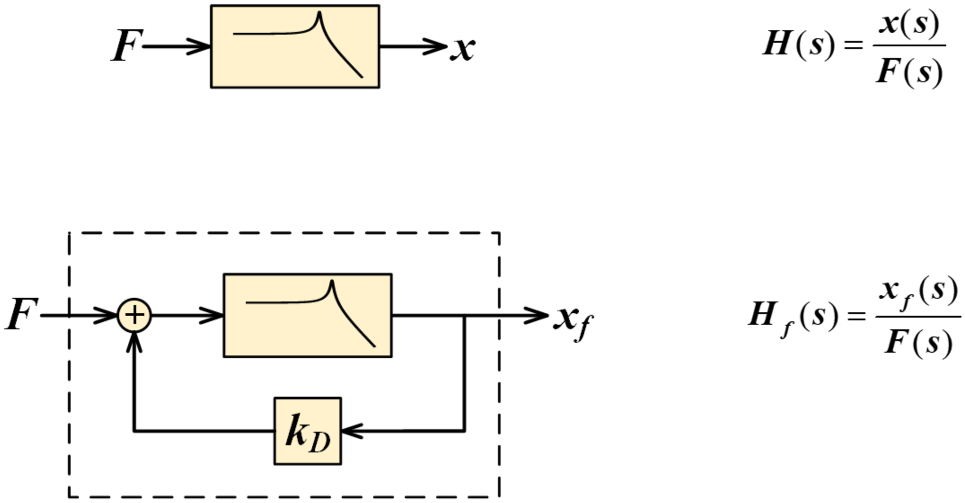

Figure 3.6: Schematic diagram of the second-order resonator with (top) and without (bottom) displacement feedback along with the corresponding force to displacement transfer functions

$$H_f(s)=\frac{\frac{1}{k}}{\left(\frac{s}{\omega_o}\right)^2+\frac{1}{Q}\frac{s}{\omega_o}+\left(1-\frac{k_D}{k}\right)} \quad , \quad \omega_{f,90^\circ}=\omega_o\sqrt{\left(1-\frac{k_D}{k}\right)} \tag{3.18}$$

As we can see the resonance frequency, defined as the frequency where the transfer function phase equals 90°, is modulated by the feedback gain. Considering that the gain can be set electronically, bidirectional frequency tuning is achieved using this technique.

Similarly we can apply the feedback force from the output velocity to the input force with a feedback gain b_D which can be thought of as a dynamic damping coefficient as depicted in Figure 3.7. The transfer functions of the two systems along with their resonance frequencies are given in Equations (3.19) and (3.20).

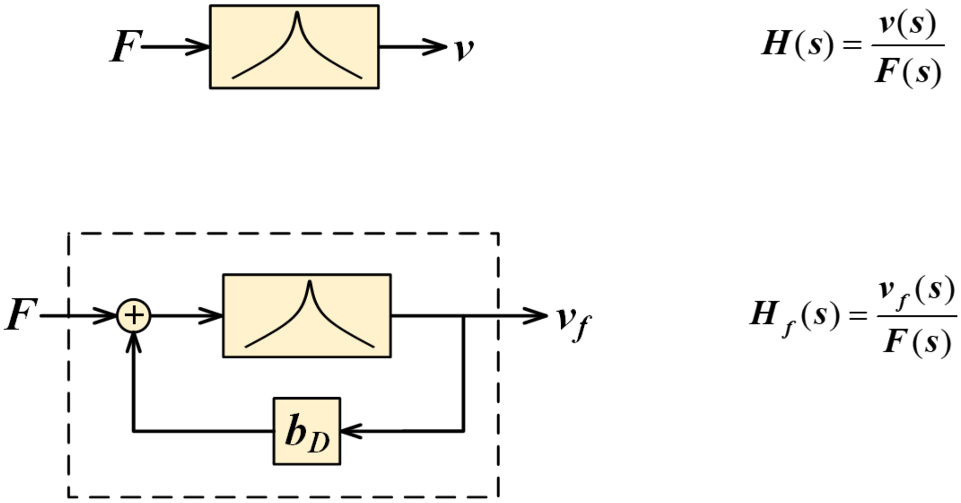

Figure 3.7: Schematic diagram of the second-order resonator with (top) and without (bottom) velocity feedback along with the corresponding force to velocity transfer functions

$$H(s)=\frac{\frac{s}{b\omega_o Q}}{\left(\frac{s}{\omega_o}\right)^2+\frac{1}{Q}\frac{s}{\omega_o}+1} \tag{3.19}$$

$$H_f(s)=\frac{\frac{s}{b\omega_o Q}}{\left(\frac{s}{\omega_o}\right)^2+\frac{1}{Q}\left(1-\frac{b_D}{b}\right)\frac{s}{\omega_o}+1}\ ,\ Q_f=\frac{Q}{1-\frac{b_D}{b}} \tag{3.20}$$

As we can see the quality factor is modulated by the feedback gain. Again, considering that the gain can be set electronically, bidirectional frequency tuning is achieved using this technique.

Active frequency and quality factor tuning are demonstrated by applying displacement and velocity feedback to an AlN-on-Si square resonator. The resonator structure, shown in Figure 3.8, is anchored to the substrate with a network of side-supporting tethers which serve as signal routing paths as well. The device can be transduced using eight top electrodes to support different vibration modes. However, to excite the second-order in-plane flexural vibration modes the corner electrodes are grounded and the four side electrodes are used for driving, sensing and controlling the parameters of the resonator as shown in Figure 3.9 along with the isometric and top views of the mode shape. The resonant frequency of the flexural mode is ~5.9 MHz with a *Q* of ~2900 and an insertion loss of ~40 dB. The device is mounted on a printed circuit board (PCB) with voltage amplifiers that provide the drive and tuning voltages to the resonator and transimpedance amplifiers (TIAs) that are used for sensing the output current signals. The PCB is then interfaced with a FlexRIO system from National Instruments which includes

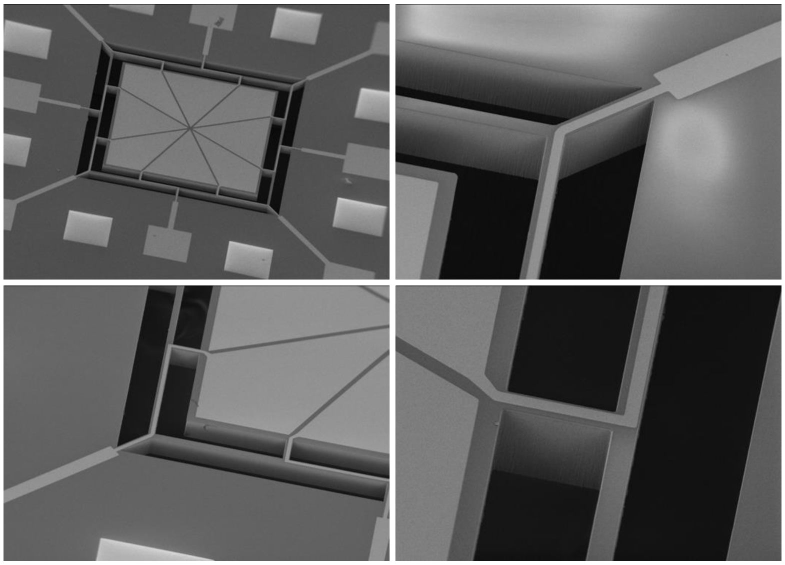

Figure 3.8: SEM images of the AlN-on-Si square resonator connected to the substrate using a network of T-supports

a field programmable gate array (FPGA) in communication with a real-time controller as shown in Figure 3.10. An adapter module converts the signals between the analog and

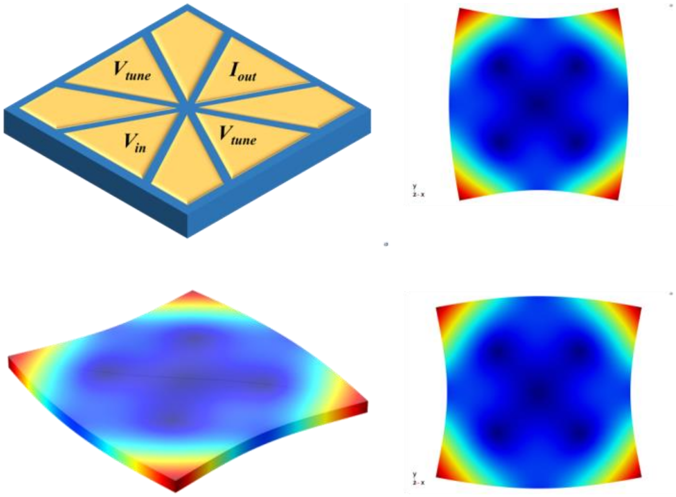

Figure 3.9: Schematic view of the piezoelectric square resonator and the isometric and top views of the second-order in-plane flexural vibration mode shape.

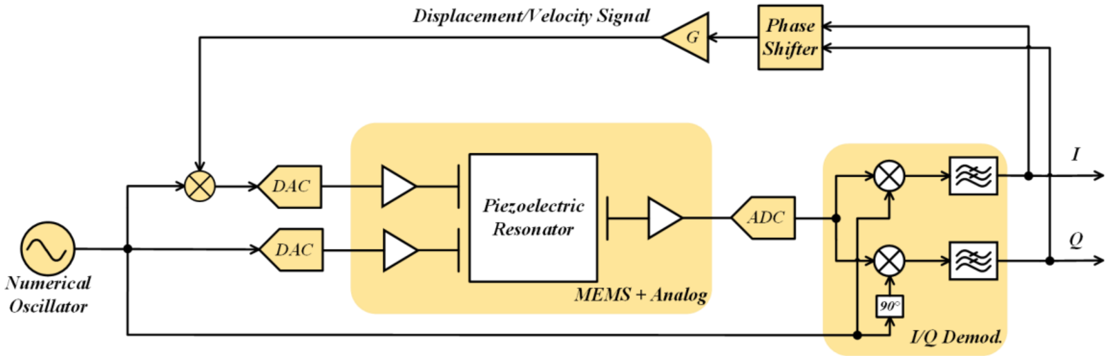
Displacement/Velocity Signal
G
Phase Shifter
DAC
DAC
Piezoelectric Resonator
ADC
MEMS + Analog
90°
I/Q Demod.
I
Q
Numerical Oscillator

Figure 3.10: Interface system architecture for active feedback tuning of resonance parameters.

digital domains on the PCB and the FPGA. The generation of the excitation and feedback signals, and in-phase and quadrature-phase demodulation are done in the digital domain. The feedback signal is constructed by phase shifting the demodulated output signals and applying them to the input after mixing with the excitation signal.

The frequency response of the AlN-on-Si resonators with displacement and velocity feedback applied is shown in Figure 3.11 and Figure 3.12. A bidirectional

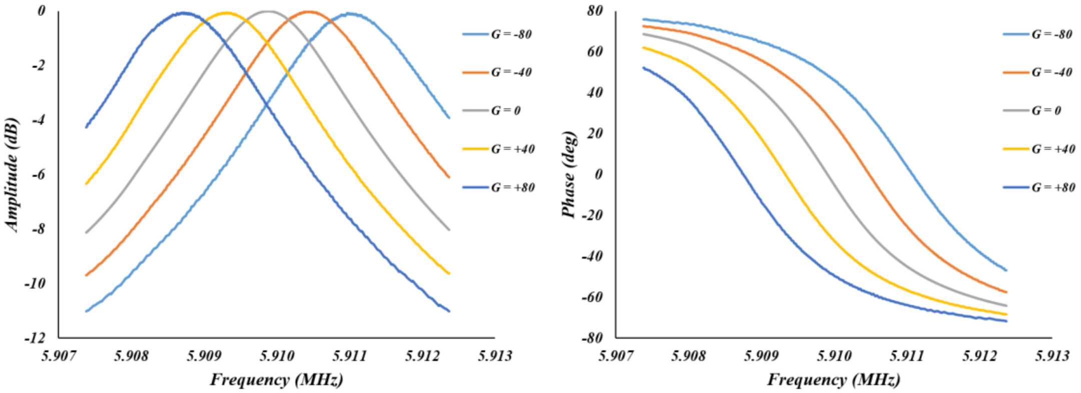

Figure 3.11: Frequency response of the piezoelectric resonator with active displacement feedback. The resonance frequency is tuned by ~400 p.p.m. in both directions.

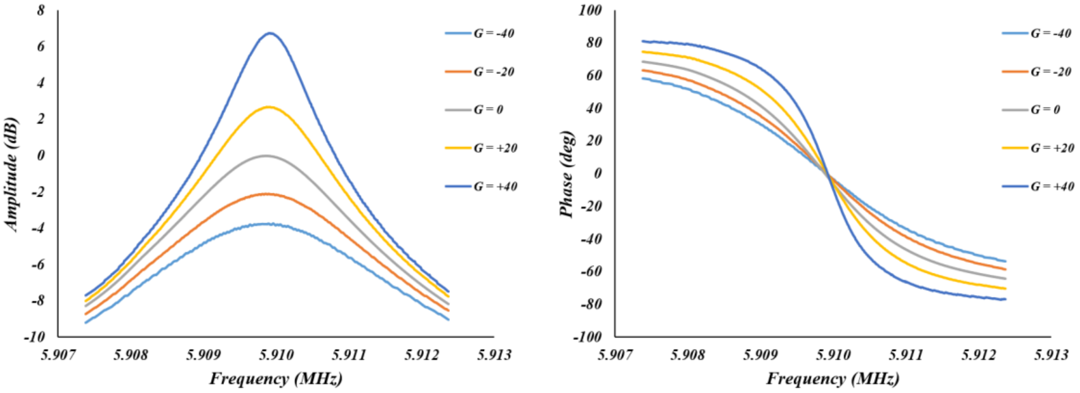

Figure 3.12: Frequency response of the piezoelectric resonator with active velocity feedback. Quality factor is tuned from 1800 to 6300 with the reference *Q* value of 2900.

frequency tuning range of ~800 p.p.m. is achieved with applying displacement feedback. Active Q tuning is also achieved by applying velocity feedback resulting in a tuned Q range of 1800 to 6300 for a reference Q value of 2900 without active tuning.

CHAPTER 4. A MODE-MATCHED ALN-ON-SILICON RESONANT ANNULUS GYROSCOPE

"I saw the angel in the marble and carved until I set him free." – Michelangelo

The main objective of this research is to develop the high-frequency resonant gyroscope technology based on the piezoelectric-on-substrate platform. There are many advantages with increasing the resonant frequency of the gyroscopes, most notably superior vibration and shock immunity. Moreover, the piezoelectric-on-substrate platform provides its own advantages in terms of efficient transduction, in-air operation as there is no need for narrow gaps, elimination of DC voltages, and excellent linearity and power handling. With all these benefits come the challenges of first designing a piezoelectric gyroscope, and second mode matching the gyroscope solely based on piezoelectric transduction, as examined in previous chapters. This chapter presents a high-frequency mode-matched AlN-on-Si gyroscope which provides competing performance compared with the state of the art and even surpasses in some metrics, namely the operation bandwidth and noise level.

4.1. Design of the AlN-on-Si Annular Gyroscope

The displacement and stress field patterns of the drive and sense vibration modes of the piezoelectric annulus gyroscope are shown in Figure 4.1. The major dimensions of the structure are initially adopted for best expected gyroscopic performance and spurious vibration modes rejection and then all the design parameters are fine-tuned throughout the design process.

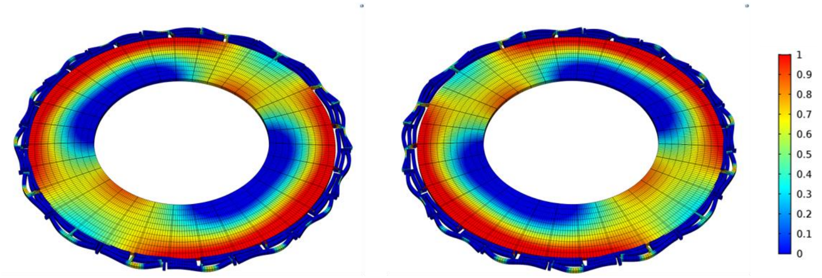

Drive Displacement Sense Displacement

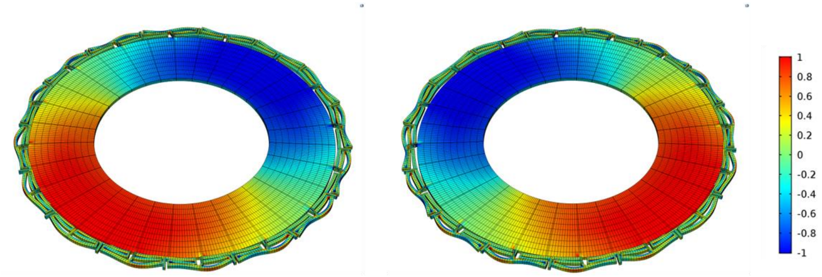

Drive Stress Sense Stress

Figure 4.1: Drive and sense vibration mode shapes of the annulus piezoelectric gyroscope showing the displacement field (top) and the stress pattern (bottom) of the in-plane flexural resonant mode. The stress field pattern is suitable for top-side piezoelectric transduction.

The performance of the piezoelectric annulus gyroscope is simulated using the COMSOL finite-element analysis tool. One important aspect of the design process is to control different effects of mechanical damping so that the behavior of quality factor of the fabricated device can be predicted. There are different damping mechanisms, such as anchor loss, thermoelastic damping, air damping, and piezoelectric losses, that contribute to the overall mechanical damping of the device. Although there has been a recent research interest [59-63], piezoelectric losses, among other factors, are the least well understood sources of damping. Therefore, it is crucial to ensure the contribution of anchor loss and thermoelastic damping are negligible by design. Considering that there is no need for implementation of narrow gaps in the fabrication process, air damping, although inevitably present, will not hinder the operation of the device.

The annular structure is anchored on the periphery using a network of symmetric double-T supports. Anchor loss is computed using perfectly matched layers, and the supporting structure is optimized so that the anchor quality factor (Q_{ANCHOR}) value obtained from simulations is larger than 2,000,000, ensuring structural decoupling from the substrate. Thermoelastic damping simulations also show a quality factor (Q_{TED}) larger than 200,000, which is much larger and so negligible compared with the target quality factor (Q_{TARGET}) of 5,000 to 10,000 for the gyroscope design.

Figure 4.2 shows the simulated output Coriolis current of the AlN-on-Si resonant gyroscope derived from frequency-domain simulations. For simulation of the scale factor and mechanical noise equivalent rotation rate (MNEΩ) of the device, a Q value of 6,300, which was obtained from measurement of the devices after fabrication, and a driving voltage of 90 mV, according to the testing conditions, were assumed. The simulated Coriolis output current yields a scale factor of 1.62 nA/°/s. The simulated motional resistance based on the drive mode output current is 1,082 Ω, and the maximum kinetic energy of the drive mode is computed to be 0.593 nJ. The small motional resistance value proves the strong electromechanical coupling of the thin-film piezoelectric layer for the transduction of the in-plane flexural vibration modes.

Equations (4.1) and (4.2) below are used to calculate the gyroscopic coupling coefficient, λ, and the MNEΩ for the gyroscope.

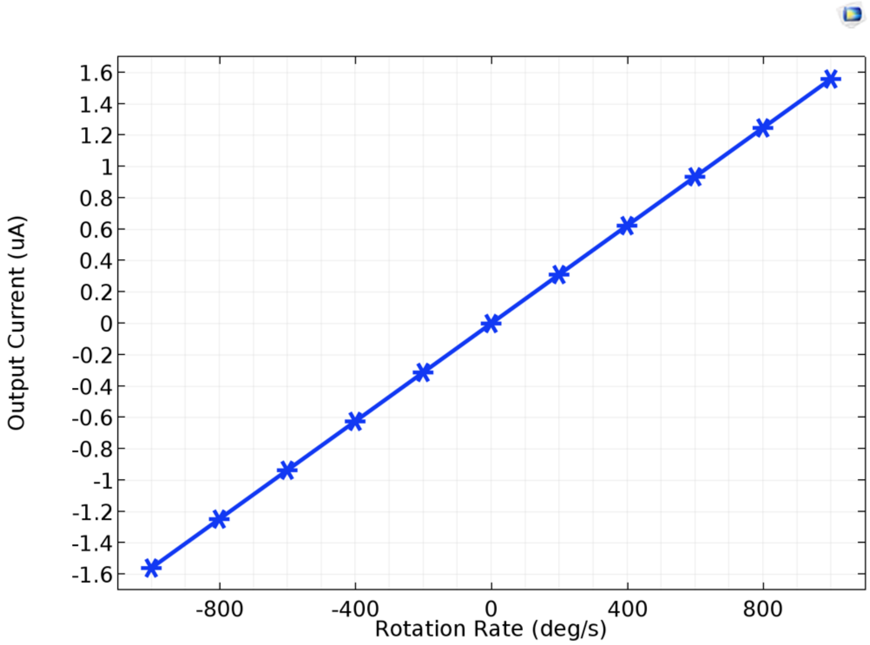

Figure 4.2: Simulated output Coriolis current of the AlN-on-Si annulus resonant gyroscope, showing a scale factor of 1.62 nA/°/s for an assumed *Q* of 6,300 and a driving voltage of 90 mV peak.

$$\lambda = \frac{1}{2Q}\frac{\omega_o}{\Omega}\frac{i_S}{i_D} \tag{4.1}$$

$$MNE\Omega = \frac{1}{\lambda}\sqrt{\frac{k_B T\omega_o}{2E_k Q}} \tag{4.2}$$

In the above equations, i_D and i_S are the drive- and sense-mode output currents, Ω is the external rotation rate, E_k is the maximum kinetic energy, k_B and T are the Boltzmann constant and ambient temperature, and ω_o and Q are the resonance frequency and quality factor of the resonant gyroscope. Substituting the values obtained from FEA results in a gyroscopic coupling coefficient of 0.876 and MNEΩ of 24.7 °/h/√Hz. A summary of the simulation parameters and results is provided in Table 4.1.

Table 4.1: COMSOL simulation results for the AlN-on-Si resonant annulus gyroscope

Parameter	Simulated Value
Resonance Frequency, f_o	3.1596 MHz
Q_{TARGET}	5,000 – 10,000
Q_{ANCHOR}	> 2,000,000
Q_{TED}	>200,000
Drive Voltage, V_d	90 mV
Motional Resistance, R_m	1,082 Ω
Maximum Kinetic Energy, E_k	0.593 nJ
Scale Factor	1.62 nA/°/s
Gyroscopic Coupling Factor, λ	0.876
MNEΩ	24.7 °/h/√Hz

4.2. Fabrication and Characterization of the AlN-on-Si Annular Gyroscope

An SEM image of the fabricated annulus piezoelectric gyroscope is shown in Figure 4.3a. The device structure is comprised of a 1.3 µm thin film of aluminum nitride (AlN) deposited between 50 nm top and bottom molybdenum (Mo) electrode layers and stacked on top of a 15 µm thick (100) silicon-on-insulator (SOI) device layer. The silicon handle layer is etched from the back side to release the structural device layer as described in section 2.3.

The annulus structure has an outer radius of 700 µm, an inner radius of 400 µm, a radial tether span of 0.8° and a tangential trench width of 15 µm. The radial trench span is 0.4°, and the tangential trench width etched into the silicon device layer is 5 µm. The device is anchored to the substrate through a network of circularly symmetric double-T supports to ensure structural symmetry of the drive and sense modes. The tether and trench widths are designed for maximum acoustic decoupling of the double-T structure. The support network is also used to route the electrical signals to the eight metal electrodes attached to the structure. Figure 4.3b and Figure 4.3c show close-up images of the supporting tethers with the routing of the top Mo layer between the device and a signal pad. The signal electrode pads on the substrate are separated by eight ground electrodes, which provide a common connection to the bottom Mo layer around the device. A close-up view of the piezoelectric stack on top of the silicon layer is also shown in Figure 4.3d.

The gyroscope is transduced using eight identical top electrodes. Pairs of electrodes that are spatially 45° apart are used for gyroscope excitation and readout compatible with eigenmode operation. One pair is used to excite the drive mode, a second pair is used to

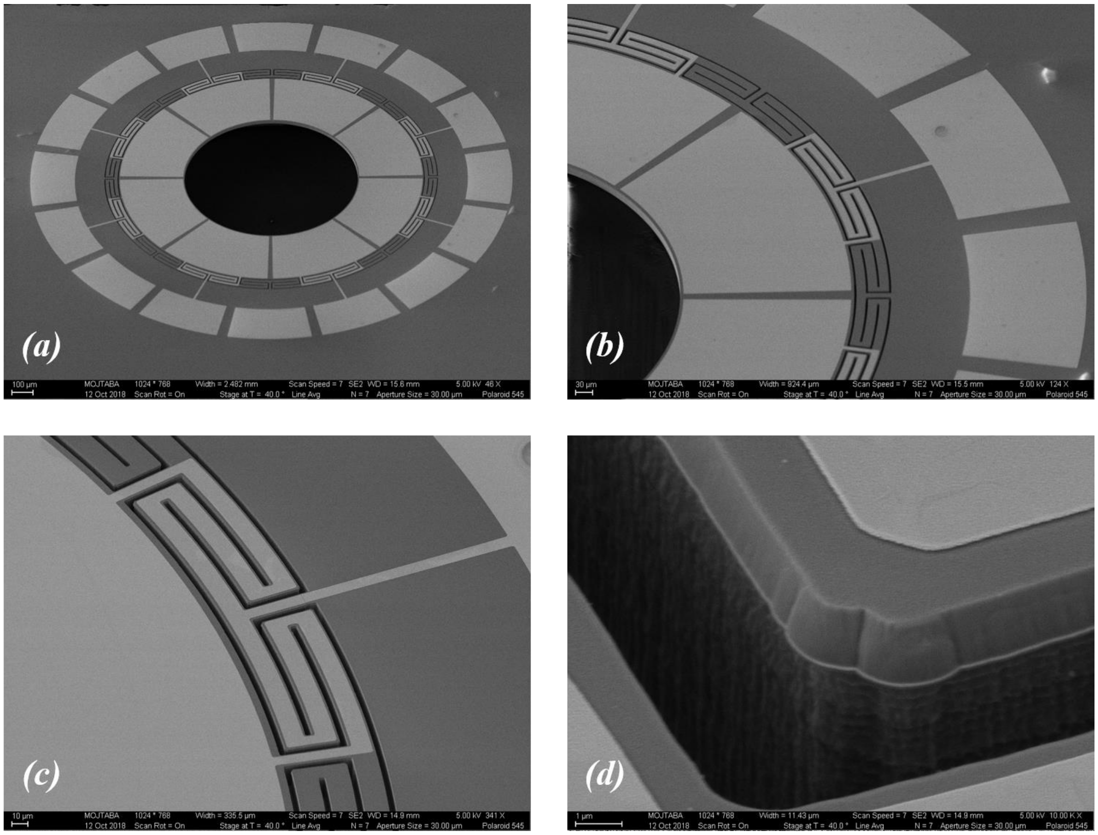

Figure 4.3: SEM images of annulus piezoelectric resonant gyroscopes fabricated using a simple 4-mask AlN-on-Si process. (a) 8 top electrodes used for eigenmode operation of the gyroscope. (b) The network of peripheral tethers is used to both support the structure and provide a routing path for the electrical connections.

pick off the drive signal, and the remaining two pairs of electrodes are used for differential readout of the sense mode signal.

Eigenmode operation circuitry for the piezoelectric annulus gyroscope was implemented on a printed circuit board, and the device was interfaced digitally with an FPGA module from National Instruments to realize the drive loop, the sense channel, and the dynamic frequency tuning scheme. The two excitation signals of the gyroscope are scaled using two voltage dividers followed by buffers to apply the coefficients of α and

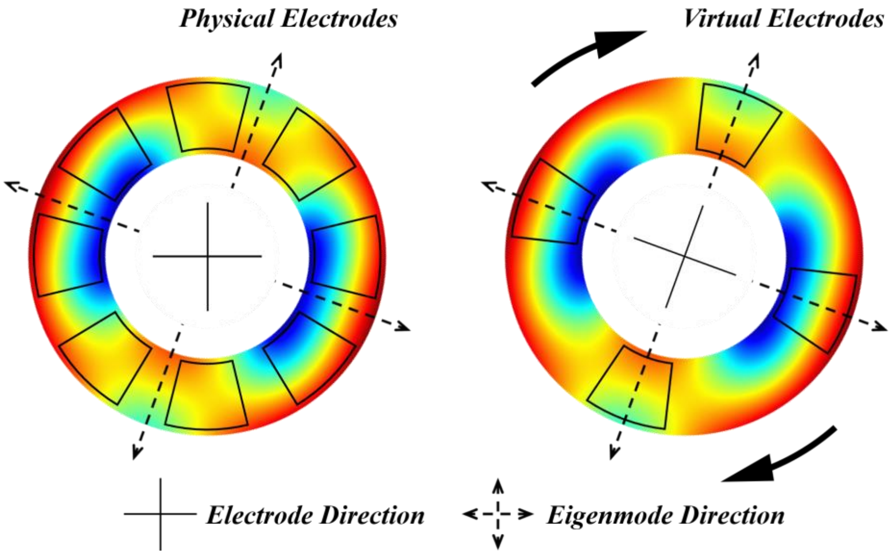

Figure 4.4: Schematic illustration of the eigenmode operation. The natural vibration modes are misaligned with respect to the electrodes as fabricated (left) and by applying scaling coefficients to electrode pairs the location of effective excitation and readout electrodes is virtually controlled and aligned with the eigenmodes (right).

$(1-\alpha)$ with the proper normalization factor to the drive electrodes. The same scaling coefficients are used to scale the drive output and the differential sense output signals to generate the effective drive and sense currents from the pickoff electrodes in essence creating virtual electrodes in the direction of the eigenmodes as shown in Figure 4.4. The effective drive current is integrated and scaled in a digital feedback loop to provide the displacement signal necessary for dynamic frequency tuning. The level of frequency tuning is adjusted by an external coefficient to control the amplitude of the displacement feedback. Perfect mode matching, where the sense mode response is minimized and the drive and sense frequencies are equal, is achieved by iterative adjustment of the factor α and matching the drive and sense frequencies by adjusting the level of displacement feedback.

The digital interface was implemented on a FlexRIO system from National Instruments (NI), which consists of a field-programmable gate array (FPGA) in communication with a real-time controller [64, 65]. An adapter module from NI provides analog-to-digital and digital-to-analog conversion capability.

A schematic of the interface system for the piezoelectric gyroscope along with the PCB and measurement setup is shown in Figure 4.5. The drive oscillator loop, the sense channel and the electromechanical feedback loop for the realization of frequency tuning are all implemented in the digital domain. The drive input signal is generated using a numerically controlled oscillator (NCO). The frequency of the NCO is controlled based on the output phase of the drive demodulated signal to track the resonance peak using a proportional-integral controller. The sense channel demodulators use the same NCO-generated signal for demodulation of the gyroscope output signal with a phase shift applied to account for the delay between the input and output signals to the gyroscope. The frequency tuning loop is implemented using the output drive signal. Since the output drive signal is proportional to the velocity of the resonator, this signal is integrated and applied back at the input with an amplification gain to control the displacement-dependent signal at the input of the gyroscope. Implementing the eigenmode operation circuitry in the digital domain results in a large flicker noise in the output signal of the gyroscope mainly due to the large uncorrelated noise injected in the system by using two different digital-to-analog converters. For that reason, eigenmode operation processing is performed in the analog domain. The drawback is the limited precision of implementation of the eigenmode coefficients, which directly affects the output bias of the gyroscope.

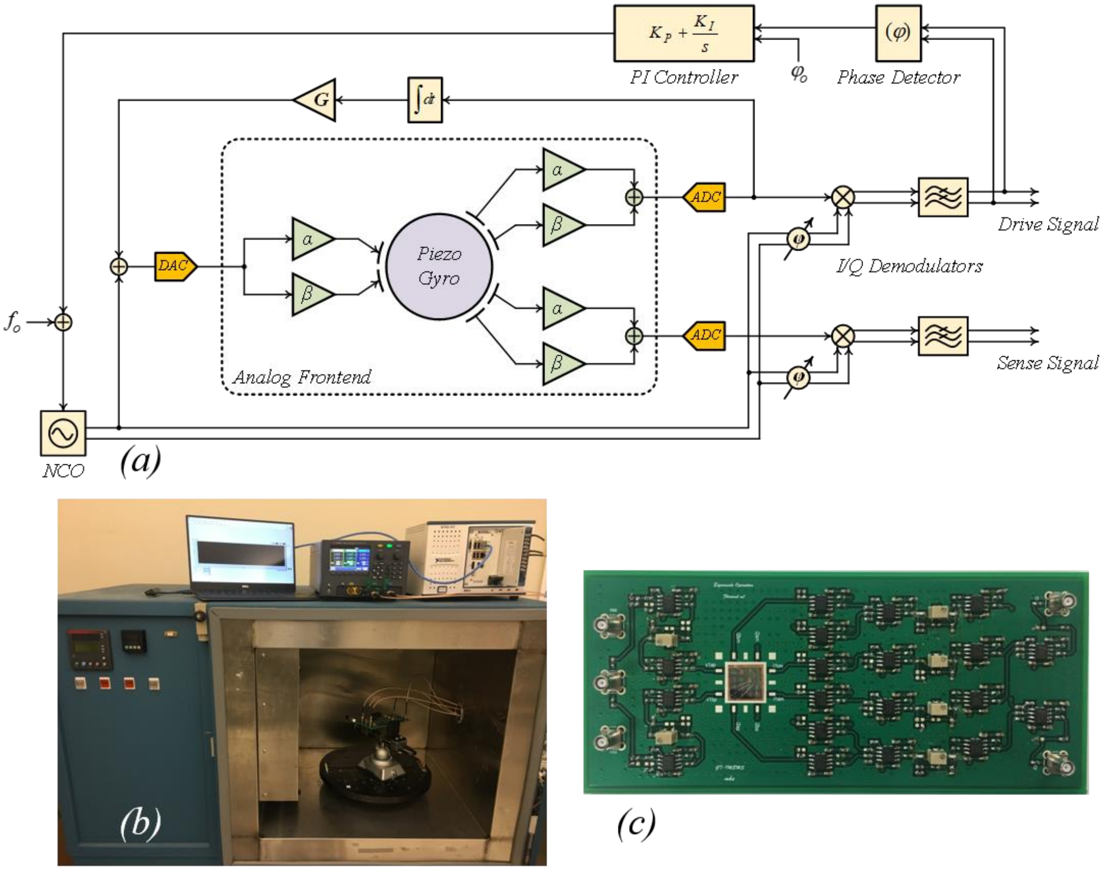
$K_P + \frac{K_I}{s}$
PI Controller
φ_o
(φ)
Phase Detector
G
$\int dt$
α
β
Piezo Gyro
DAC
ADC
Drive Signal
I/Q Demodulators
Sense Signal
Analog Frontend
f_o
NCO
(a)
(b)
(c)

Figure 4.5: (a) Interface system architecture of the piezoelectric gyroscope. The drive loop, sense channel, and dynamic displacement feedback are implemented in the FPGA in the digital domain. The piezoelectric gyroscope is actuated and sensed in the analog domain based on eigenmode operation. (b) Measurement setup, including a FlexRIO system from National Instruments in communication with the analog frontend mounted on the rate table and controlled by the PC. (c) Printed circuit board showing the device actuated by applying the eigenmode input pair voltage and sensed by processing the output current according to eigenmode operation. Potentiometers at the input and output are used for realization of the eigenmode operation coefficients.

The normalized drive and sense frequency responses of the AlN-on-Si resonant gyroscope as fabricated, with eigenmode operation only, and with eigenmode operation and dynamic frequency tuning applied simultaneously are shown in Figure 4.6. The amplitudes are normalized with respect to the drive amplitude at resonance, which was measured to be ~ -23 dB, translating to a motional resistance of ~1300 Ω.

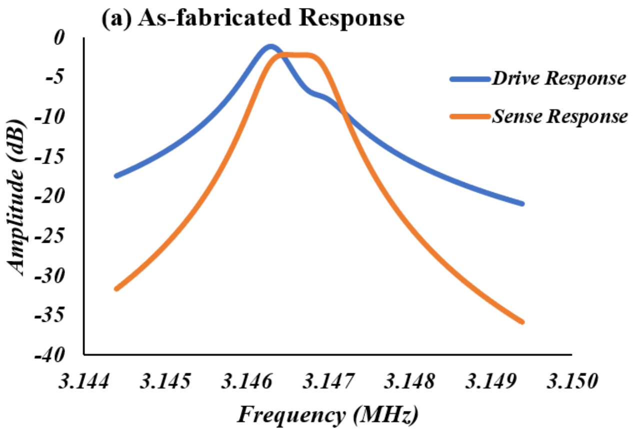
(a) As-fabricated Response

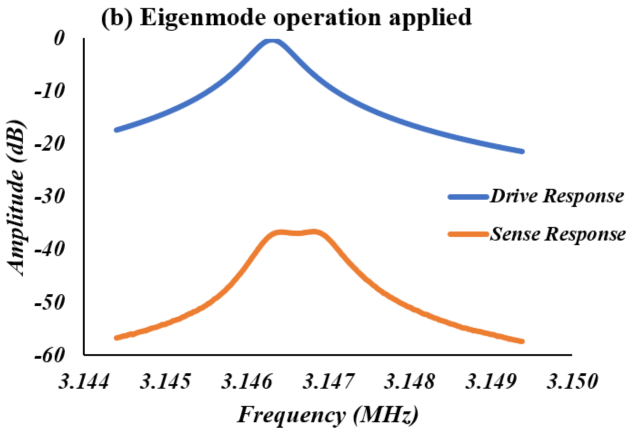
(b) Eigenmode operation applied

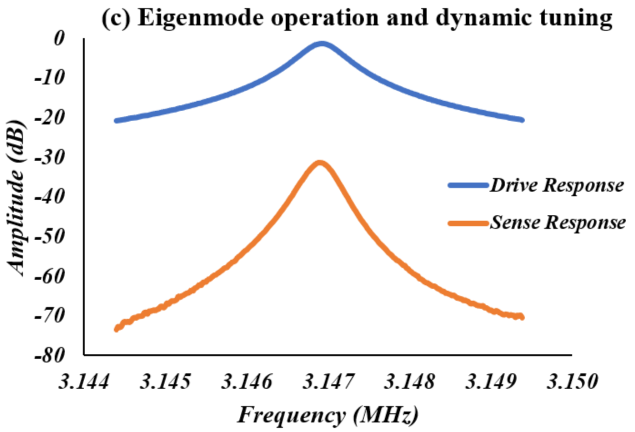
(c) Eigenmode operation and dynamic tuning

Figure 4.6: The normalized drive and sense frequency responses of the AlN-on-Si resonant gyroscope as fabricated (a), with eigenmode operation only (b) and with eigenmode operation and dynamic frequency tuning applied (c). The zero-rate error is reduced by ~35 dB with the application of eigenmode operation. The device shows a *Q* of ~6,300 while operating in air, corresponding to a mode-matched mechanical bandwidth of 500 Hz.

The zero-rate error is suppressed the most when the direction of the virtual transduction electrode is closest to the eigenmode direction, causing the sense-mode peak to disappear from the drive frequency response and the sense-mode response to be reduced significantly. The zero-rate error is reduced by ~35 dB with the application of eigenmode operation. The device shows a *Q* of ~6,300 while operating in air, corresponding to a large mode-matched mechanical bandwidth of ~500 Hz.

The measured output current of the piezoelectric gyroscope as a function of the applied external rotation rate is plotted in Figure 4.7a. The experimental scale factor is measured to be 1.57 nA/°/s for a 90 mV-peak input drive voltage. The time-domain output waveform of the gyroscope is plotted in Figure 4.7b over a period of 70 seconds. The input mechanical rotation rate to the device is 20, 40, 60, 80, 40, and 20 °/s, applied at a frequency of 1 Hz for the first four signals and 2 Hz for the last two. The Allan deviation plot of the piezoelectric gyroscope showing a measured angle random walk of 0.86 °/√h is given in Figure 4.7c. The measured thermal noise value is very close to the simulated mechanical noise equivalent rotation, MNEΩ, of 24.7 °/h/√Hz considering the effect of the interface noise. The bias instability of the gyroscope is ~125 °/h, which is limited by the precision of modal alignment and excess noise from the discrete electronics. The precision of modal alignment is limited by the resolution of the eigenmode coefficient adjustment. The analog potentiometers that are used at the input and output ports of the gyroscope to adjust the coefficients of eigenmode operation impose a significant limitation on the resolution of the eigenmode coefficient and hence limit the level of decoupling between the drive and sense modes, which directly affects the bias instability of the device.

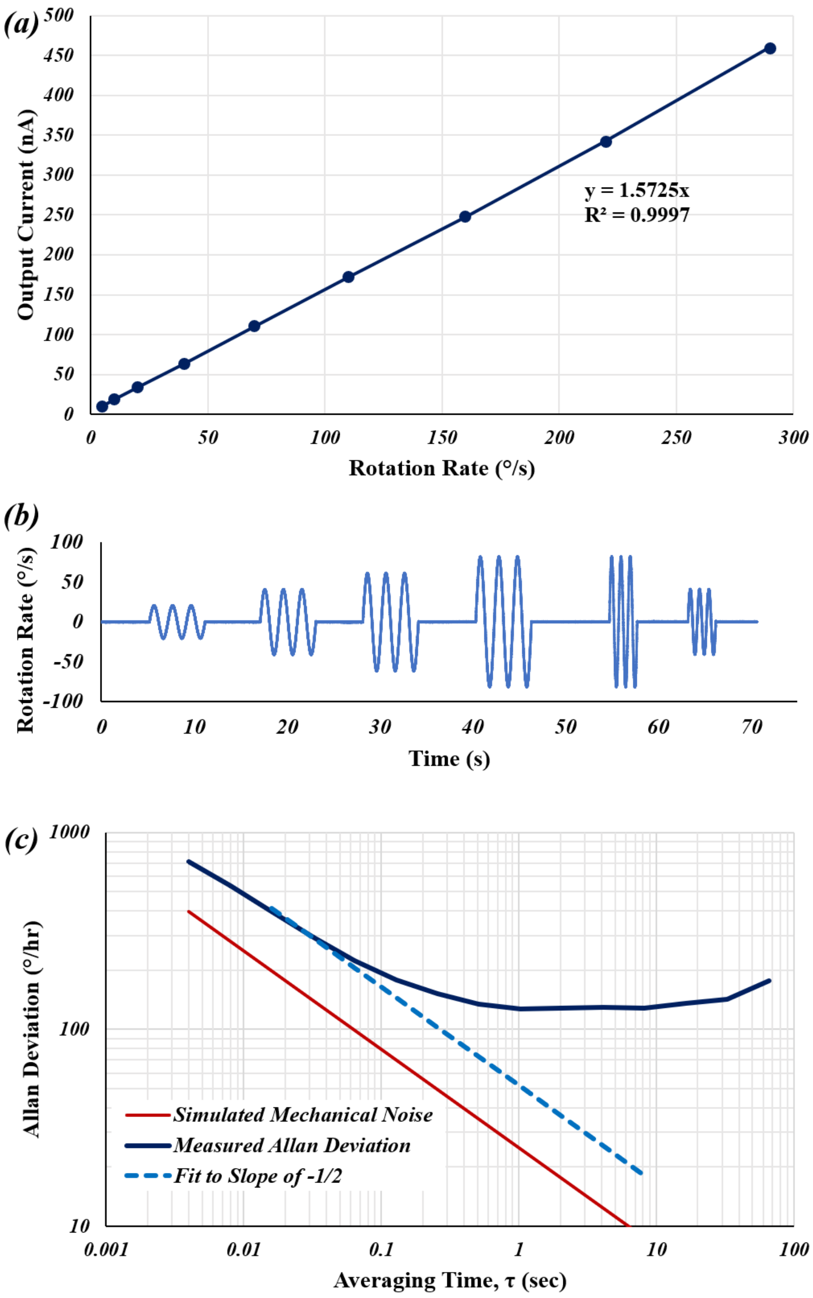

Figure 4.7: (a) The measured output current of the piezoelectric gyroscope vs. the applied external rotation rate. The experimental scale factor is 1.57 nA/°/s for an input 90 mV peak drive voltage. (b) The time-domain output waveform for different rotation rates at two frequencies of 1 Hz and 2 Hz and different rotation amplitudes. (c) Allan deviation plot of the piezoelectric gyroscope showing a measured angle random walk of 0.86 °/√h, which is close to the simulated MNEΩ of 24.7 °/h/√Hz considering the effect of interface noise. The bias instability of the gyroscopes is ~125 °/h, which is limited by the precision and excess noise of the interface circuitry.

The other limiting factor in achieving a lower bias instability is the phase noise of the drive signal, which is generated by the numerically controlled oscillator and digital-to-analog converters [66]. The phase noise appears as a signal-dependent flicker component at the output of the gyroscope and hence limits the minimum achievable bias instability regardless of the level of the excitation signal.

The temperature behavior of the drive and sense resonance modes of the piezoelectric gyroscope is characterized from -40°C to +100°C, as shown in Figure 4.8. The maximum frequency split between the two modes is 107 ppm with a maximum frequency split variation of 6 ppm over the temperature range. The linear temperature coefficient of frequency is ~ -12 ppm/°C. The insertion losses of the drive and sense modes remain almost constant over the temperature range, with a maximum difference of 0.9% between the two modes and a maximum variation of 0.6% over the temperature range. Considering mechanical decoupling from the substrate and similar piezoelectric losses, the quality factors of the two modes remain almost constant over the temperature range with a maximum difference of 3.2% between the two modes and a maximum variation of 2.2% from -40°C to +100°C.

The wideband frequency response of the gyroscope drive mode is shown in Figure 4.9. All the spurious modes are suppressed, by design, compared with the gyroscope resonance peak by at least 40 dB to minimize interference and lock-in complications.

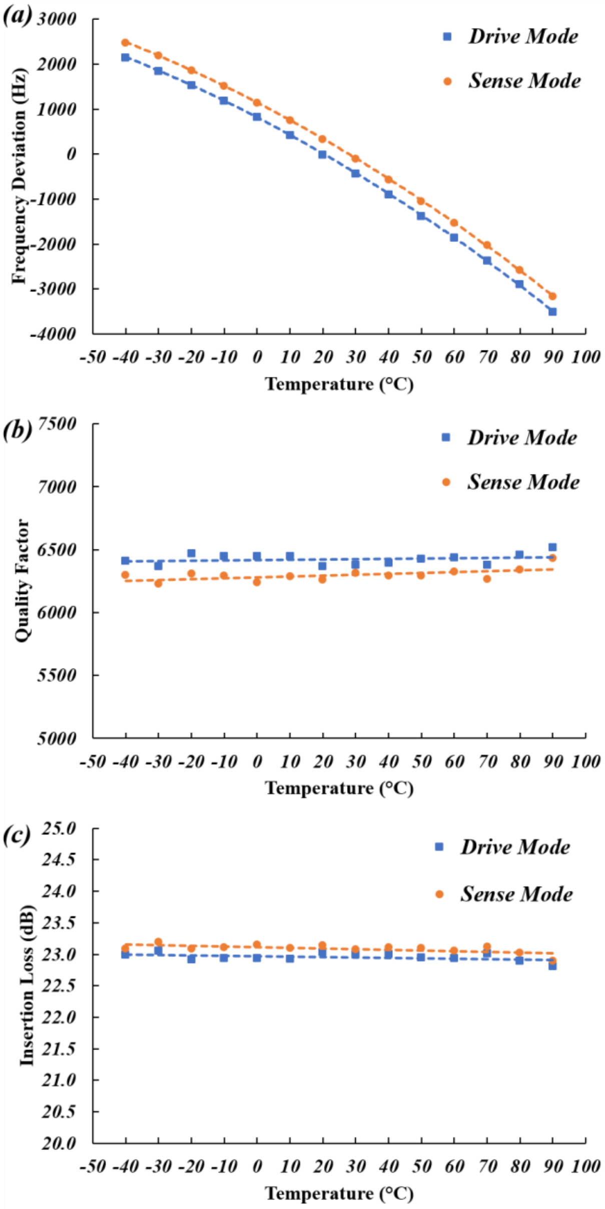

Figure 4.8: Temperature characterization plots for the AlN-on-Si resonator gyroscope. (a) Temperature dependence of drive and sense resonance frequency deviations from the drive resonance frequency at 20°C showing a maximum frequency split of 107 ppm between the two modes with a maximum frequency split variation of 6 ppm over the temperature range. The linear temperature coefficient of frequency is ~ -12 ppm/°C. (b) Drive and sense mode insertion loss vs. temperature. The insertion loss of both modes remains almost constant over the temperature range with a maximum difference of 0.9% between the two modes and maximum variation of 0.6%. (c) Drive and sense mode *Q* vs. temperature. Considering mechanical decoupling from the substrate, the quality factor remains almost constant over the temperature range with a maximum difference of 3.2% between the two modes and a maximum variation of 2.2%.

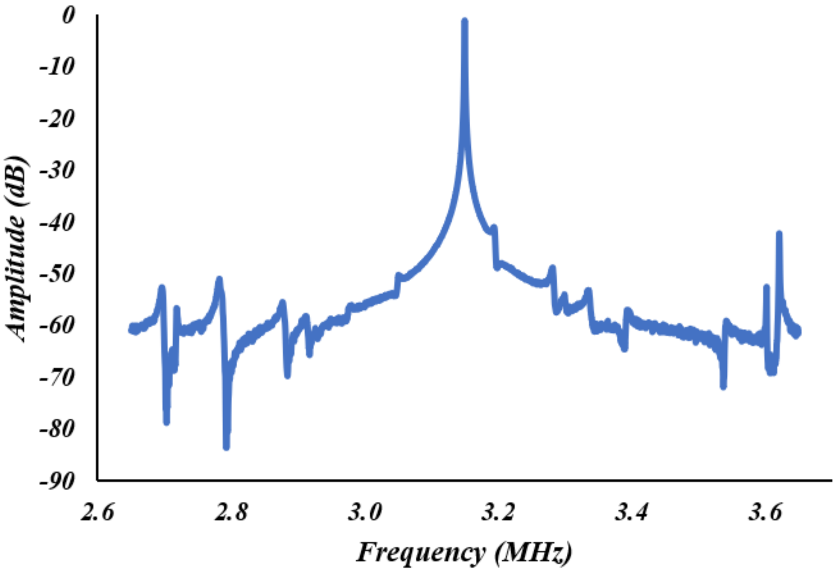

Figure 4.9: Wideband frequency response of the piezoelectric gyroscope drive mode showing the spurious modes suppressed by at least 40 dB around the resonance peak.

4.3. Improvement of the Bias Instability

The main factor affecting the bias instability (BI) of the gyroscope is the coupling between the drive and sense mode signals. The larger the coupling level is, the larger becomes the unwanted signal in the sense channel causing higher BI. In eigenmode operation, by changing the signal coefficients at the input and output ports, the effective direction of transduction is adjusted to be aligned to the natural directions of vibration along which we get the maximum decoupling between the two modes and lowest bias level and bias instability. Allan deviation plots are shown in Figure 4.10 for an AlN-on-Si resonant gyroscope with and without eigenmode operation. The application of eigenmode operation resulted in significant reduction of bias instability from 1700°/h to 270°/h for the same drive excitation voltage of 50mV-peak. The higher value of angle random walk

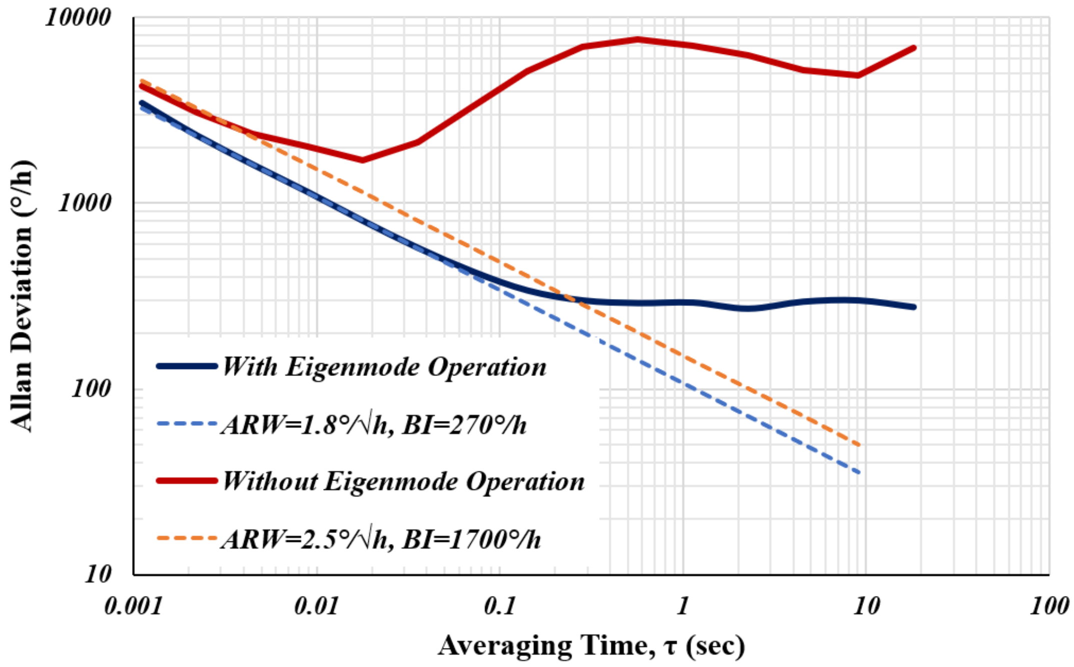

Figure 4.10: Allan deviation plots with and without eigenmode operation. The bias instability is reduced from 1700 deg/h to ~270 deg/h by adjusting the eigenmode coefficients and hence the transduction direction. The residual bias is due to slight misalignment from the natural vibration directions caused by the limited resolution of eigenmode coefficients adjustment.

(ARW) for the case where eigenmode operation is not applied is attributed to the larger frequency mismatch caused by the quadrature signal. The maximum decoupling achievable depends on the precision of eigenmode coefficient adjustment. In this experiment, the eigenmode coefficients were adjusted using analog potentiometers with limited precision which translated to a lower bound of 270 °/h for the bias instability.

The underlying limiting factor in achieving a lower bias instability, however, is the phase noise of the drive signal which is generated by the NCO and DACs in the interface setup. The phase noise of the excitation signal appears as a flicker component in the bias output after demodulation and more importantly, the level of this flicker component is proportional to the level of the drive signal. This means that improving the scale factor by driving the gyroscope harder, does not translate into an improvement in the bias instability level as the flicker noise at the output increases proportionally. We have shown this effect by measuring the Allan deviation at two different drive voltage levels. As we can see in Figure 4.11, increasing the drive amplitude from 20mV-peak to 50mV-peak results in a proportional reduction in the ARW as the thermal noise remains constant. However, the BI remains almost constant at around 300 °/h limited by the drive signal-proportional flicker component.

In conclusion, the BI level can be reduced by implementing a more accurate mechanism for adjustment of the eigenmode coefficients to reduce the effect of all of the error sources in the output and in particular the reduction of phase noise in the drive signal will result in lower bias instability as the flicker noise in the output is the dominant source of error in the current interface system.

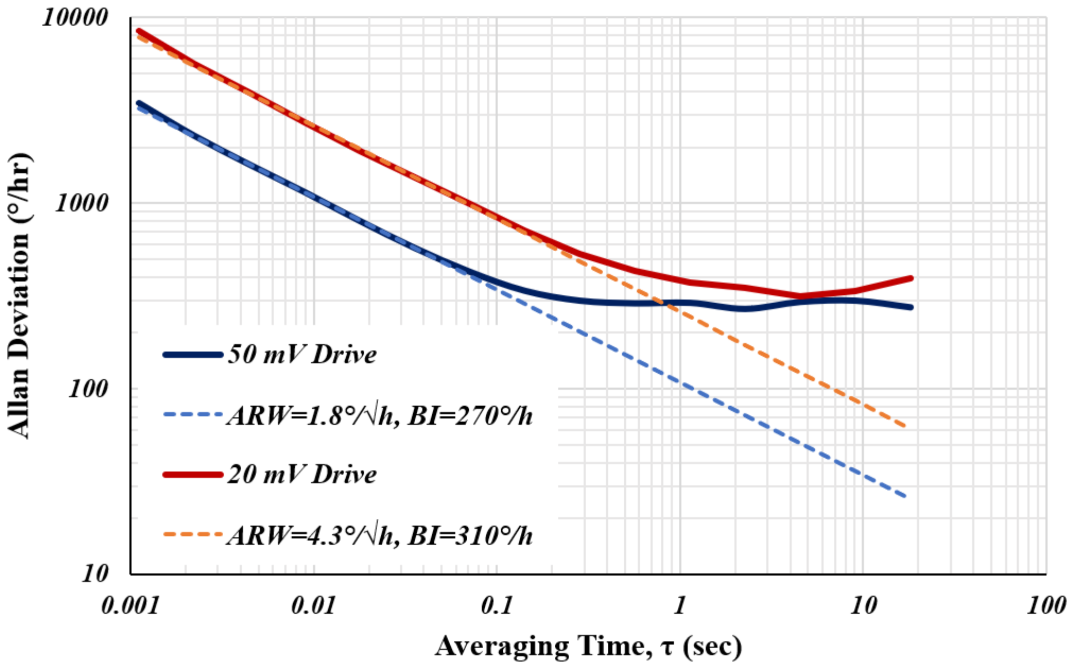

Figure 4.11: Allan deviation plots at two different drive voltage levels. Increasing the excitation voltage from 20mV to 50mV results in the reduction of thermal noise in the output bias as expected. However, this reduction does not translate to lower bias instability as it is limited by the phase noise of the NCO and DACs (flicker noise after demodulation) which is proportional to the excitation signal. In other words, larger excitation results in larger scale factor and hence lower ARW as the thermal noise remains constant but it does not result in lower bias instability as the flicker noise is signal dependent.

CHAPTER 5. CONCLUSIONS AND FUTURE DIRECTIONS

“I never think of the future; it comes soon enough.” – Albert Einstein

This work presented the theory for design and method of mode matching of piezoelectric Coriolis vibratory gyroscopes, along with the implementation of a mode-matched thin-film AlN-on-Si resonant gyroscope with performance characteristics exceeding the state of the art. The sputter-deposited thin-film piezoelectric material offers significant advantages in terms of the manufacturability of MEMS gyroscopes compared with the current dominant technology based on bulk piezoelectric materials. The utilization of the degenerate pair of in-plane flexural vibration modes of an annular structure is the key feature that enables efficient thin-film piezoelectric transduction, resulting in low noise, a low motional resistance, and a high scale factor suitable for low-power applications. To provide mode matching capability, it was showed analytically that modal alignment of resonant gyroscopes can be achieved by applying a rotation transformation to the actuation and sensing directions regardless of the transduction mechanism. This eigenmode operation technique to mode match a piezoelectric gyroscope obviates the need for narrow capacitive gaps and DC polarization voltages that are otherwise required with conventional mode matching techniques. It is worth noting that the application of eigenmode operation is not limited to piezoelectric devices and can be extended to modal alignment of resonant gyroscopes regardless of their transduction mechanism or axis of operation. In particular, since electrostatic quadrature cancellation in pitch and roll gyroscopes requires the implementation of physical electrodes that span the subspaces of both in-plane and out-of-plane vibration modes to compensate for modal cross coupling

[67, 68], eigenmode operation is a good candidate for modal alignment of these devices without the need for the implementation of complex fabrication processes.

The following sections provide some insight into further developing the piezoelectric gyroscope technology towards establishing a comprehensive rotation sensing solution.

5.1. Center-Supported Design for the Piezoelectric Gyroscope

One major mode of failure of MEMS devices is associated with the stress induced in the structure due to packaging of the device. Mismatches in the coefficients of thermal expansion could lead to compressive or tensile stresses and even bending of the MEMS structure which could affect both the mechanical characteristics of the device as well as the electromechanical transduction. Therefore, it is very favorable to have the anchor points of the device isolated from the peripheral substrate so to achieve stress isolation. Contrary to capacitive devices with lateral transduction gaps that are directly affected by package substrate the piezoelectric gyroscope with flexural vibration mode can be anchored in the center and be supported with the handle layer.

Figure 5.1 shows such design for an AlN-on-Si annular gyroscope with the supporting structure connected to the inner radius of the device and anchored to the handle layer. Finite-element analysis showed no degradation in performance for center-supported devices compared with side-supported gyroscopes. In addition to stress isolation, the smaller area of the device is also favorable. Although the fabrication process of these devices is the same as the side-supported devices, the HF release time is considerably

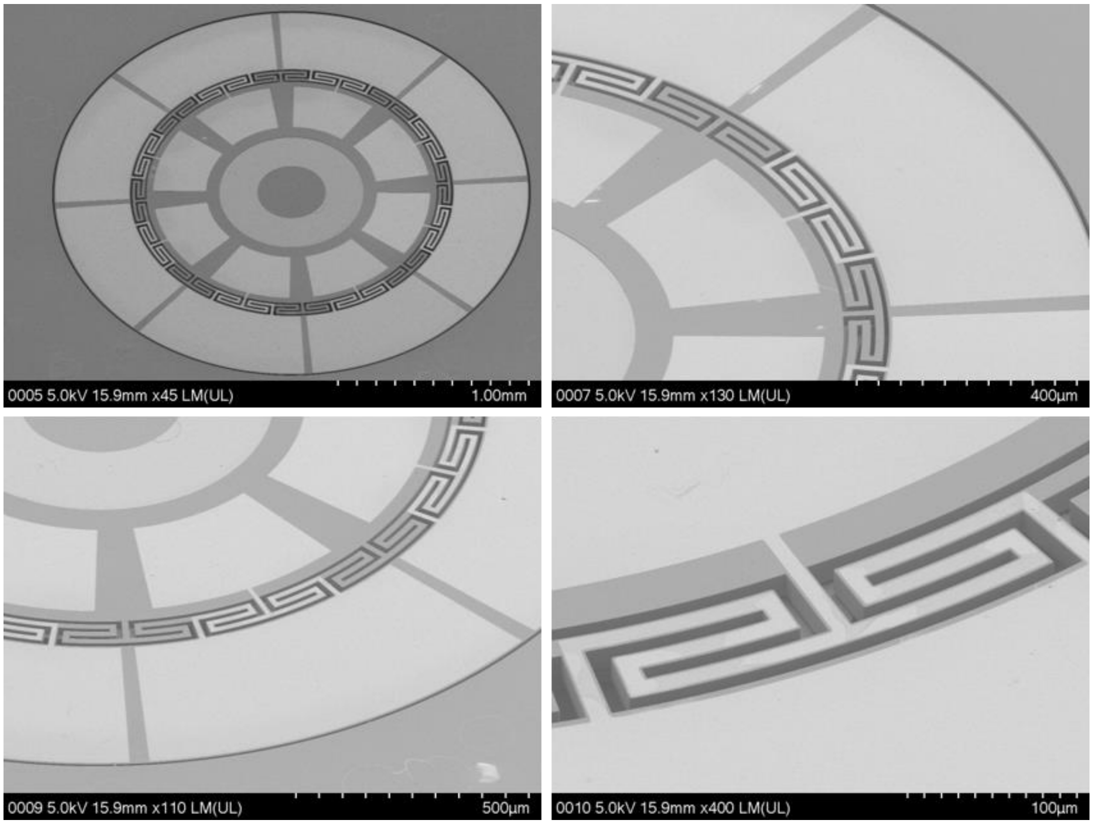
0005 5.0kV 15.9mm x45 LM(UL)
1.00mm
0007 5.0kV 15.9mm x130 LM(UL)
400μm
0009 5.0kV 15.9mm x110 LM(UL)
500μm
0010 5.0kV 15.9mm x400 LM(UL)
100μm

Figure 5.1: A center-supported AlN-on-Si resonant gyroscope. The annular structure is supported using a network of double-T tethers which serve as signal routing paths as well and anchored in the center to the handle layer. The device is separated from the peripheral substrate for package stress isolation.

longer and demands vigilance as the backside cannot be etched entirely and lateral etching of the buried oxide layer is required.

5.2. Pitch and Roll and Triaxial Piezoelectric Gyroscopes

The piezoelectric-on-substrate rotation sensing platform is not complete without the ability to sense rotation along the in-plane rotation axes. Many applications, such as gaming and image stabilization rely on sensing the pitch and roll rotation. Moreover, the stringent constraints on the allocated surface area and thickness of these chips call for designs that integrates all three yaw, pitch, and roll devices in a single structure.

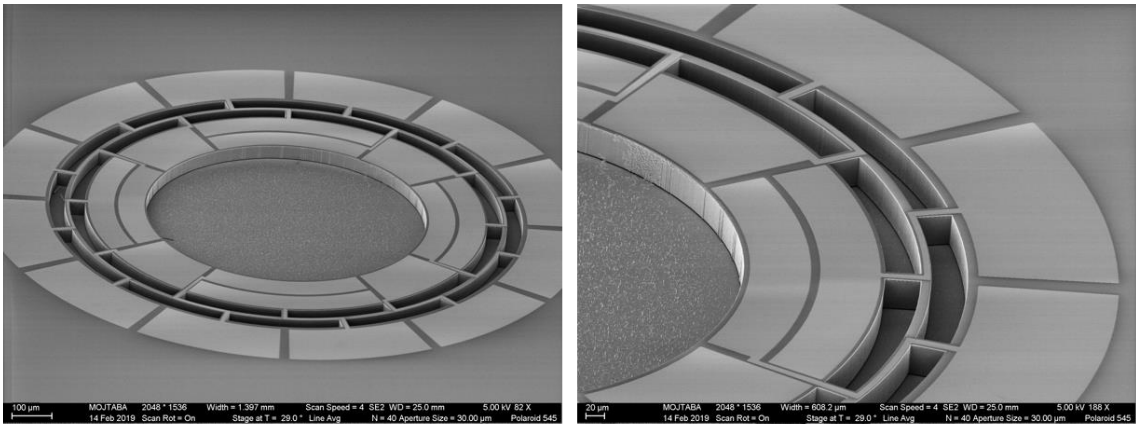

Figure 5.2: A preliminary design for a pitch and roll AlN-on-Si resonant gyroscope with a second-order elliptical drive vibration mode and third-order out-of-plane bending sense modes.

Figure 5.2 shows a preliminary design for a pitch and roll gyroscope based on the second-order elliptical drive vibration mode and third-order out-of-plane bending sense modes. Since the resonance frequency of the out-of-plane modes depend directly on the thickness of the structure, the frequency split between the drive and sense modes could be in the order of tens of kilo hertz which is problematic for mode-matched devices. Precise control of the thickness of the device layer is required to ensure a smaller initial frequency split. The weak piezoelectric transduction efficiency of the elliptical mode could also hinder achieving a large signal-to-noise ratio. Therefore, modifying the design to adopt a vibration mode with stronger electromechanical transduction efficiency would be desirable.

Finally, a representative design for a three-axis piezoelectric gyroscope is shown in Figure 5.3. The yaw gyroscope is supported at the center with the pitch and roll annular device around it and anchored to the peripheral substrate.

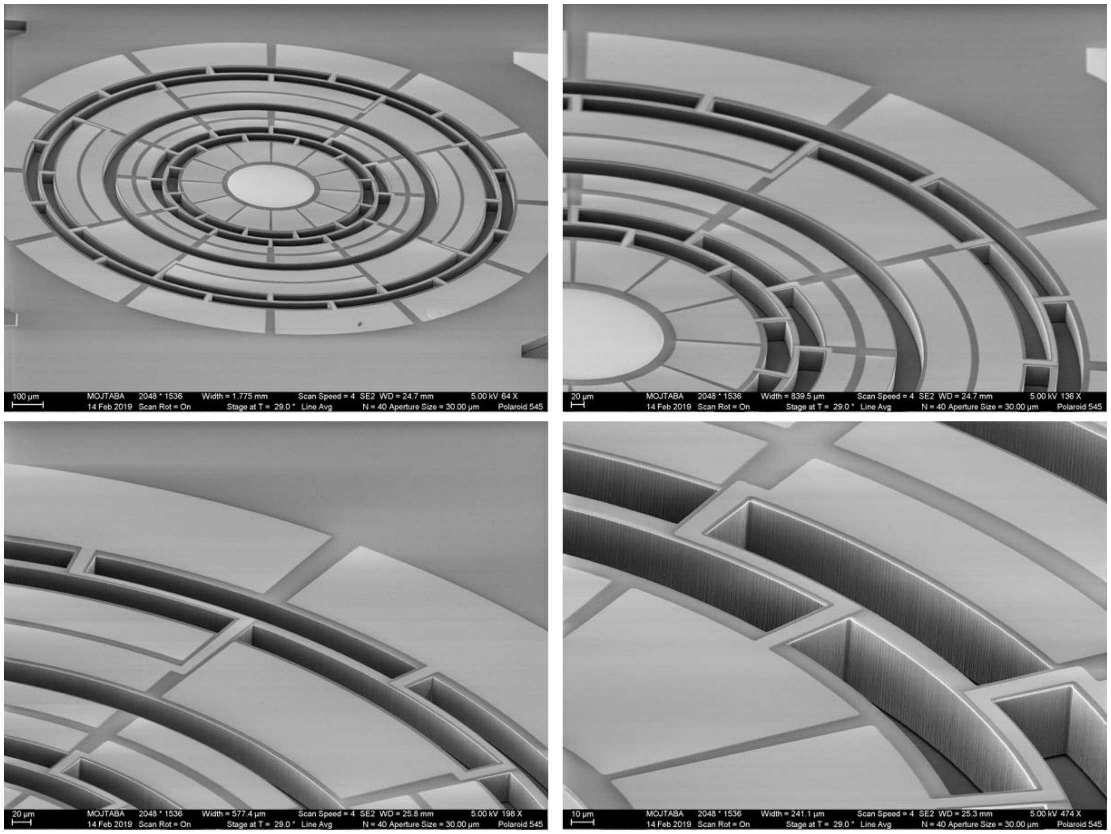
100 µm
MOJTABA 2048 * 1536 Width = 1.775 mm Scan Speed = 4 SE2 WD = 24.7 mm 5.00 kV 64 X
14 Feb 2019 Scan Rot = On Stage at T = 29.0 ° Line Avg N = 40 Aperture Size = 30.00 µm Polaroid 545
20 µm
MOJTABA 2048 * 1536 Width = 839.5 µm Scan Speed = 4 SE2 WD = 24.7 mm 5.00 kV 136 X
14 Feb 2019 Scan Rot = On Stage at T = 29.0 ° Line Avg N = 40 Aperture Size = 30.00 µm Polaroid 545
20 µm
MOJTABA 2048 * 1536 Width = 577.4 µm Scan Speed = 4 SE2 WD = 25.8 mm 5.00 kV 198 X
14 Feb 2019 Scan Rot = On Stage at T = 29.0 ° Line Avg N = 40 Aperture Size = 30.00 µm Polaroid 545
10 µm
MOJTABA 2048 * 1536 Width = 241.1 µm Scan Speed = 4 SE2 WD = 25.3 mm 5.00 kV 474 X
14 Feb 2019 Scan Rot = On Stage at T = 29.0 ° Line Avg N = 40 Aperture Size = 30.00 µm Polaroid 545

Figure 5.3: A representative design for a triaxial AlN-on-Si gyroscope with the annular pitch and roll device supported to the peripheral substrate and the yaw device placed in the middle and anchored to the handle layer in the center of the structure.

REFERENCES

[1] G. H. Bryan, "On the Beats in the vibrations of a revolving cylinder or bell," in *Proceedings of the Cambridge Philosophical Society*, 1890, vol. 7, no. 24, pp. 101-111.

[2] L. Joseph and N. Elwood, "Rate and attitude indicating instrument," United States Patent 2,309,853, 1943.

[3] J. M. O'connor and D. M. Shupe, "Vibrating beam rotation sensor," United States Patent 4,381,672, 1983.

[4] J. J. Bernstein and M. S. Weinberg, "Comb drive micromechanical tuning fork gyro," United States Patent 5,349,855, 1994.

[5] M. R. Layton, "Rotation rate sensor with optical sensing device," United States Patent 5,796,002, 1998.

[6] J. A. Geen, S. J. Sherman, J. F. Chang, and S. R. Lewis, "Single-chip surface micromachined integrated gyroscope with 50 deg/h Allan deviation," *Ieee J Solid-St Circ*, vol. 37, no. 12, pp. 1860-1866, 2002.

[7] J. A. Geen, "Very low cost gyroscopes," in *Proceedings of the 2005 IEEE Sensors Conference*, 2005, pp. 537-540.

[8] S. G. Saraswathy, J. Geen, and J. Chang, "High performance gyro with fast startup time, high range, wide bandwidth, low noise and excellent vibration immunity," in *Proceedings of the 2012 IEEE/ION Position, Location and Navigation Symposium (PLANS)*, 2012, pp. 20-23.

[9] L. Prandi *et al.*, "A low-power 3-axis digital-output MEMS gyroscope with single drive and multiplexed angular rate readout," in *Proceedings of the 2011 IEEE International Solid-State Circuits Conference*, 2011, pp. 104-106.

[10] B. Vigna, "Tri-axial MEMS gyroscopes and Six Degree-Of-Freedom Motion Sensors," in *Proceedings of the 2011 International Electron Devices Meeting (IEDM)*, 2011, pp. 29.1.1-29.1.3.

[11] J. Seeger, M. Lim, and S. Nasiri, "Development of high-performance, high-volume consumer MEMS gyroscopes," in *Proceedings of the 2010 Solid-State Sensors, Actuators, and Microsystems Workshop*, 2010, pp. 61-64.

[12] G. K. Balachandran, V. P. Petkov, T. Mayer, and T. Balslink, "A 3-Axis Gyroscope for Electronic Stability Control With Continuous Self-Test," *Ieee J Solid-St Circ*, vol. 51, no. 1, pp. 177-186, 2016.

[13] M. F. Zaman, A. Sharma, Z. Hao, and F. Ayazi, "A Mode-Matched Silicon-Yaw Tuning-Fork Gyroscope With Subdegree-Per-Hour Allan Deviation Bias Instability," *Journal of Microelectromechanical Systems,* vol. 17, no. 6, pp. 1526-1536, 2008.

[14] A. A. Trusov *et al.*, "Flat is not dead: Current and future performance of Si-MEMS Quad Mass Gyro (QMG) system," in *Proceedings of the 2014 IEEE/ION Position, Location and Navigation Symposium (PLANS)*, 2014, pp. 252-258.

[15] A. A. Trusov *et al.*, "mHRG: Miniature CVG with beyond navigation grade performance and real time self-calibration," in *Proceedings of 2016 IEEE International Symposium on Inertial Sensors and Systems*, 2016, pp. 29-32.

[16] J. Y. Cho, J. Woo, J. Yan, R. L. Peterson, and K. Najafi, "Fused-Silica Micro Birdbath Resonator Gyroscope," *Journal of Microelectromechanical Systems,* vol. 23, no. 1, pp. 66-77, 2014.

[17] P. Shao, V. Tavassoli, C. L. Mayberry, and F. Ayazi, "A 3D-HARPSS Polysilicon Microhemispherical Shell Resonating Gyroscope: Design, Fabrication, and Characterization," *IEEE Sensors Journal,* vol. 15, no. 9, pp. 4974-4985, 2015.

[18] P. Shao, C. L. Mayberry, X. Gao, V. Tavassoli, and F. Ayazi, "A Polysilicon Microhemispherical Resonating Gyroscope," *Journal of Microelectromechanical Systems*, vol. 23, no. 4, pp. 762-764, 2014.

[19] F. Ayazi and K. Najafi, "A HARPSS polysilicon vibrating ring gyroscope," *Journal of Microelectromechanical Systems,* vol. 10, no. 2, pp. 169-179, 2001.

[20] T. Su, S. H. Nitzan, P. Taheri-Tehrani, M. H. Kline, B. E. Boser, and D. A. Horsley, "Silicon MEMS Disk Resonator Gyroscope With an Integrated CMOS Analog Front-End," *IEEE Sensors Journal,* vol. 14, no. 10, pp. 3426-3432, 2014.

[21] D. E. Serrano *et al.*, "Substrate-decoupled, bulk-acoustic wave gyroscopes: Design and evaluation of next-generation environmentally robust devices," *Microsystems & Nanoengineering,* vol. 2, no. 1, p. 16015, 2016/04/25 2016.

[22] R. Antonello and R. Oboe, "MEMS gyroscopes for consumer and industrial applications," I. Minin, Ed.: IntechOpen, 2011.

[23] "IEEE Standard for Inertial Sensor Terminology," *IEEE Std 528-2019,* pp. 1-35, 2019.

[24] D. W. Allan, "Statistics of atomic frequency standards," *Proceedings of the IEEE,* vol. 54, no. 2, pp. 221-230, 1966.

[25] "IEEE Standard Specification Format Guide and Test Procedure for Single-Axis Interferometric Fiber Optic Gyros," *IEEE Std 952-1997,* pp. 1-84, 1998.

[26] N. Yazdi, F. Ayazi, and K. Najafi, "Micromachined inertial sensors," *Proceedings of the IEEE,* vol. 86, no. 8, pp. 1640-1659, 1998.

[27] R. Ruby, "A decade of FBAR success and what is needed for another successful decade," in *Proceedings of the 2011 Symposium on Piezoelectricity, Acoustic Waves and Device Applications (SPAWDA)*, 2011, pp. 365-369.

[28] R. Aigner, "SAW and BAW technologies for RF filter applications: A review of the relative strengths and weaknesses," in *Proceedings of the 2008 IEEE Ultrasonics Symposium (IUS),* 2008, pp. 582-589.

[29] "IEEE Standard on Piezoelectricity," *ANSI/IEEE Std 176-1987,* pp. 1-74, 1988.

[30] A. Erturk and D. J. Inman, "Appendix A: Piezoelectric Constitutive Equations," in *Piezoelectric Energy Harvesting*: John Wiley & Sons, Ltd, 2011, pp. 343-348.

[31] H. Johari and F. Ayazi, "Capacitive Bulk Acoustic Wave Silicon Disk Gyroscopes," in *Proceedings of the 2006 International Electron Devices Meeting (IEDM),* 2006, pp. 1-4.

[32] F. Ayazi, "Multi-DOF inertial MEMS: From gaming to dead reckoning," in *Proceedings of the 2011 16th International Conference on Solid-State Sensors, Actuators and Microsystems (TRANSDUCERS),* 2011, pp. 2805-2808.

[33] Y. Jeong, D. E. Serrano, V. Keesara, W. K. Sung, and F. Ayazi, "Wafer-level vacuum-packaged triaxial accelerometer with nano airgaps," in *Proceedings of the 2013 26th IEEE International Conference on Micro Electro Mechanical Systems (MEMS),* 2013, pp. 33-36.

[34] R. Tabrizian, M. Hodjat-Shamami, and F. Ayazi, "High-Frequency AlN-on-Silicon Resonant Square Gyroscopes," *Journal of Microelectromechanical Systems,* vol. 22, no. 5, pp. 1007-1009, 2013.

[35] F. Ayazi, R. Tabrizian, M. Hodjat-Shamami, and A. Norouzpour-Shirazi, "Resonant Gyroscopes and Methods of Making and Using the Same," United States Patent 9,917,571 Patent Appl. 14/739,721, 2018.

[36] M. Hodjat-Shamami, A. Norouzpour-Shirazi, R. Tabrizian, and F. Ayazi, "A dynamically mode-matched piezoelectrically transduced high-frequency flexural disk gyroscope," in *Proceedings of the 2015 28th IEEE International Conference on Micro Electro Mechanical Systems (MEMS),* 2015, pp. 789-792.

[37] D. M. Schwartz, D. Kim, P. Stupar, J. DeNatale, and R. T. M’Closkey, "Modal Parameter Tuning of an Axisymmetric Resonator via Mass Perturbation," *Journal of Microelectromechanical Systems*, vol. 24, no. 3, pp. 545-555, 2015.

[38] B. Hamelin, V. Tavassoli, and F. Ayazi, "Localized Eutectic Trimming of Polysilicon Microhemispherical Resonating Gyroscopes," *IEEE Sensors Journal*, vol. 14, no. 10, pp. 3498-3505, 2014.

[39] B. Hamelin, A. Daruwalla, and F. Ayazi, "Stiffness trimming of high Q MEMS resonators by excimer laser annealing of germanium thin film on silicon," in *Proceedings of the 2016 29th IEEE International Conference on Micro Electro Mechanical Systems (MEMS)*, 2016, pp. 1026-1029.

[40] B. J. Gallacher, J. Hedley, J. S. Burdess, A. J. Harris, A. Rickard, and D. O. King, "Electrostatic correction of structural imperfections present in a microring gyroscope," *Journal of Microelectromechanical Systems*, vol. 14, no. 2, pp. 221-234, 2005.

[41] M. Hodjat-Shamami and F. Ayazi, "Systems and Methods for Operation of Vibratory Gyroscopes," United States Patent 10,466,068 Patent Appl. 62449472, 2019.

[42] M. Hodjat-Shamami and F. Ayazi, "Eigenmode operation of piezoelectric resonant gyroscopes," *Microsystems & Nanoengineering*, vol. 6, no. 1, p. 108, 2020/11/30 2020.

[43] J. H. Ginsberg, *Mechanical and Structural Vibrations: Theory and Applications*. John Wiley & Sons, Inc., 2001, p. 704.

[44] M. Hodjat-Shamami, A. Norouzpour-Shirazi, and F. Ayazi, "Eigenmode operation as a quadrature error cancellation technique for piezoelectric resonant gyroscopes," in *Proceedings of the 2017 30th IEEE International Conference on Micro Electro Mechanical Systems (MEMS)*, 2017, pp. 1107-1110.

[45] F. Ayazi, R. Tabrizian, and L. Sorenson, "Compensation, tuning, and trimming of MEMS resonators," in *2012 IEEE International Frequency Control Symposium Proceedings*, 2012, pp. 1-7.

[46] A. Daruwalla, H. Wen, C. Liu, H. Jeong, and F. Ayazi, "A piezo-capacitive BAW accelerometer with extended dynamic range using a gap-changing moving electrode," in *Proceedings of the 2018 IEEE/ION Position, Location and Navigation Symposium (PLANS)*, 2018, pp. 283-287.

[47] H. Wen *et al.*, "A high-performance single-chip timing and inertial measurement unit with robust mode-matched gyroscopes," in *Proceedings of the 2018 31st IEEE International Conference on Micro Electro Mechanical Systems (MEMS)*, 2018, pp. 105-108.

[48] C. S. Lam, "A review of the recent development of MEMS and crystal oscillators and their impacts on the frequency control products industry," in *2008 IEEE Ultrasonics Symposium*, 2008, pp. 694-704.

[49] J. C. Salvia, R. Melamud, S. A. Chandorkar, S. F. Lord, and T. W. Kenny, "Real-Time Temperature Compensation of MEMS Oscillators Using an Integrated Micro-Oven and a Phase-Locked Loop," *Journal of Microelectromechanical Systems,* vol. 19, no. 1, pp. 192-201, 2010.

[50] C. Liu, R. Tabrizian, and F. Ayazi, "A ±0.3 ppm Oven-Controlled MEMS Oscillator Using Structural Resistance-Based Temperature Sensing," *IEEE Transactions on Ultrasonics, Ferroelectrics, and Frequency Control,* vol. 65, no. 8, pp. 1492-1499, 2018.

[51] R. Ruby, P. Bradley, D. Clark, D. Feld, T. Jamneala, and W. Kun, "Acoustic FBAR for filters, duplexers and front end modules," in *2004 IEEE MTT-S International Microwave Symposium Digest (IEEE Cat. No.04CH37535)*, 2004, vol. 2, pp. 931-934 Vol.2.

[52] T. Sulchek *et al.*, "High-speed tapping mode imaging with active Q control for atomic force microscopy," *Applied Physics Letters,* vol. 76, no. 11, pp. 1473-1475, 2000.

[53] M. D. Henry, J. Nguyen, T. R. Young, T. Bauer, and R. H. Olsson, "Frequency Trimming of Aluminum Nitride Microresonators Using Rapid Thermal Annealing," *Journal of Microelectromechanical Systems,* vol. 23, no. 3, pp. 620-627, 2014.

[54] B. Kim, R. H. Olsson, and K. E. Wojciechowski, "Capacitive frequency tuning of ALN micromechanical resonators," in *Proceedings of the 2011 16th International Conference on Solid-State Sensors, Actuators and Microsystems (TRANSDUCERS)*, 2011, pp. 502-505.

[55] M. Shahmohammadi, D. Dikbas, B. P. Harrington, and R. Abdolvand, "Passive tuning in lateral-mode thin-film piezoelectric oscillators," in *Proceedings of the 2011 Joint Conference of the IEEE International Frequency Control and the European Frequency and Time Forum (FCS)*, 2011, pp. 1-5.

[56] P. W. Loveday and C. A. Rogers, "Modification of piezoelectric vibratory gyroscope resonator parameters by feedback control," *IEEE Transactions on Ultrasonics, Ferroelectrics, and Frequency Control,* vol. 45, no. 5, pp. 1211-1215, 1998.

[57] N. A. Hall *et al.*, "Micromachined Accelerometers With Optical Interferometric Read-Out and Integrated Electrostatic Actuation," *Journal of Microelectromechanical Systems,* vol. 17, no. 1, pp. 37-44, 2008.

[58] A. Norouzpour-Shirazi, M. Hodjat-Shamami, R. Tabrizian, and F. Ayazi, "Dynamic tuning of MEMS resonators via electromechanical feedback," *IEEE Transactions on Ultrasonics, Ferroelectrics, and Frequency Control,* vol. 62, no. 1, pp. 129-137, 2015.

[59] R. Tabrizian and M. Rais-Zadeh, "The effect of charge redistribution on limiting the kt2.Q product of piezoelectrically transduced resonators," in *Proceedings of the 2015 18th International Conference on Solid-State Sensors, Actuators and Microsystems (TRANSDUCERS),* 2015, pp. 981-984.

[60] A. Peczalski, Z. Wu, R. Tabrizian, and M. Rais-Zadeh, "Investigation Into the Quality Factor of Piezoelectric-on-Silica Micromachined Resonators," *Journal of Microelectromechanical Systems,* vol. 24, no. 6, pp. 1695-1702, 2015.

[61] J. Segovia-Fernandez and G. Piazza, "Damping in 1 GHz laterally-vibrating composite piezoelectric resonators," in *Proceedings of the 2015 28th IEEE International Conference on Micro Electro Mechanical Systems (MEMS)*, 2015, pp. 1000-1003.

[62] J. Segovia-Fernandez and G. Piazza, "Thermoelastic Damping in the Electrodes Determines *Q* of AlN Contour Mode Resonators," *Journal of Microelectromechanical Systems,* vol. 26, no. 3, pp. 550-558, 2017.

[63] A. Qamar, S. Sherrit, X. Zheng, J. Lee, P. X. Feng, and M. Rais-Zadeh, "Study of Energy Loss Mechanisms in AlN-Based Piezoelectric Length Extensional-Mode Resonators," *Journal of Microelectromechanical Systems,* vol. 28, no. 4, pp. 619-627, 2019.

[64] S. Wisher, "An FPGA-Based Architecture For the In-Run Self-Calibration of MEMS Gyroscopes," Master of Science, School of Electrical and Computer Engineering, Georgia Institute of Technology, 2017.

[65] C. Li *et al.*, "An FPGA-Based Interface System for High Frequency Bulk-Acoustic-Wave (BAW) Micro-Gyroscopes with In-Run Automatic Mode-Matching," *IEEE Transactions on Instrumentation and Measurement,* vol. 69, no. 4, pp. 1783-1793, 2019.

[66] C. E. Calosso, A. C. C. Olaya, and E. Rubiola, "Phase-Noise and Amplitude-Noise Measurement of DACs and DDSs," *IEEE Transactions on Ultrasonics, Ferroelectrics, and Frequency Control*, vol. 67, no. 2, pp. 431-439, 2019.

[67] H. Wen, A. Daruwalla, and F. Ayazi, "Resonant pitch and roll silicon gyroscopes with sub-micron-gap slanted electrodes: Breaking the barrier toward high-performance monolithic inertial measurement units," *Microsystems &Amp; Nanoengineering*, Article vol. 3, p. 16092, 04/24/online 2017.

[68] H. Wen, A. Daruwalla, and F. Ayazi, "A 0.5MHz mode-matched pitch or roll annulus gyroscope with nano-gap slanted electrodes for quadrature cancellation," in *Proceedings of the 2017 19th International Conference on Solid-State Sensors, Actuators and Microsystems (TRANSDUCERS)*, 2017, pp. 536-539.